



DECONVOLUTION FROM WAVEFRONT SENSING  
USING OPTIMAL WAVEFRONT ESTIMATORS

THESIS  
Scott R. Maethner  
Captain, USAF

AFIT/GSO/ENP/96D-01

DEPARTMENT OF THE AIR FORCE  
AIR UNIVERSITY  
**AIR FORCE INSTITUTE OF TECHNOLOGY**

Wright-Patterson Air Force Base, Ohio

DTIC QUALITY INSPECTED

19970521 022

AFIT/GSO/ENP/96D-01

DECONVOLUTION FROM WAVEFRONT SENSING  
USING OPTIMAL WAVEFRONT ESTIMATORS

THESIS  
Scott R. Maethner  
Captain, USAF

AFIT/GSO/ENP/96D-01

Approved for public release; distribution unlimited

The views expressed in this thesis are those of the author and do not reflect the official policy or position of the Department of Defense or the U. S. Government.

AFIT/GSO/ENP/96D-01

DECONVOLUTION FROM WAVEFRONT SENSING USING  
OPTIMAL WAVEFRONT ESTIMATORS

THESIS

Presented to the Faculty of the School of Engineering  
of the Air Force Institute of Technology  
Air University  
In Partial Fulfillment of the  
Requirements for the Degree of  
Master of Science

Scott R. Maethner, B.A.  
Captain, USAF

December, 1996

Approved for public release; distribution unlimited

## *Acknowledgements*

I would like to thank the Phillips Laboratory and the folks at the Air Force Maui Optical Station (PL/OL-YY) for sponsoring this research. I'd also like to express appreciation to my thesis advisor, Maj Mike Roggemann, for the opportunity to conduct this research, for his sound direction, and for the patience he demonstrated for someone new to this field. I also owe a lot to Dr. Byron Welsh for his guidance and many helpful suggestions. Thanks to Dr. Chris Hall for the thorough review and to Maj Price Smith for the review and the Spacecast 1996 project. I'd also like to thank 1Lt Greg Wood for sharing ideas on this topic and for the *Dante's Inferno* optics study sessions. A sincere thank you goes out to Cindy Hyde for passing down the corporate knowledge of the resident imaging codes. I also appreciate the suggestions I received from Capt David Lee. I'd like to thank Capt Wayne Zorn for helping me keep my center on the golf course and Lt Brian Robinson for pushing me at the gym. Finally, I'd like to thank my GSO-96D classmates for making my assignment at AFIT fun and memorable. I sincerely hope our paths will cross again.

Scott R. Maethner

## *Table of Contents*

|   | Page |
|---|------|
| Acknowledgements . . . . .                                | ii   |
| List of Figures . . . . .                                 | viii |
| List of Tables . . . . .                                  | xi   |
| Abstract . . . . .  | xii  |
| I. Introduction . . . . .                                 | 1    |
| 1.1 The Problem: Imaging Through Atmospheric Turbulence . | 1    |
| 1.2 Mitigation Methods . . . . .                          | 2    |
| 1.3 Deconvolution from Wavefront Sensing . . . . .        | 6    |
| 1.4 Problem Statement . . . . .                           | 6    |
| 1.5 Current Knowledge . . . . .                           | 7    |
| 1.6 Scope . . . . .                                       | 8    |
| 1.7 Approach . . . . .                                    | 8    |
| 1.8 Research Objectives . . . . .                         | 8    |
| 1.9 Key Results . . . . .                                 | 9    |
| 1.10 Thesis Organization . . . . .                        | 10   |
| II. Theory . . . . .                                      | 11   |
| 2.1 Introduction . . . . .                                | 11   |
| 2.2 Imaging System Theory . . . . .                       | 11   |
| 2.3 Atmospheric Turbulence Theory . . . . .               | 13   |
| 2.3.1 Signal . . . . .                                    | 15   |
| 2.3.2 Measurement Noise . . . . .                         | 15   |

|  | Page |
|--|------|
| 2.3.3 Signal to Noise Ratio . . . . .                                      | 16   |
| 2.4 Deconvolution from Wavefront Sensing Theory . . . . .                  | 17   |
| 2.4.1 Wavefront Sensor . . . . .   | 18   |
| 2.4.2 Phase Estimation for DWFS . . . . .                                  | 22   |
| 2.4.3 Post-Processing Deconvolution Procedure . . . . .                    | 27   |
| 2.5 Simulating DWFS . . . . .  | 28   |
| 2.6 Performance Metrics . . . . .  | 29   |
| 2.6.1 Average Pupil-Averaged Mean Square Residual Phase<br>Error . . . . . | 31   |
| 2.6.2 Average System Transfer Function . . . . .                           | 32   |
| 2.6.3 Signal-to-Noise Ratio . . . . .                                      | 33   |
| 2.6.4 OTF Correlation . . . . .  | 34   |
| 2.6.5 Image Quality Assessment . . . . .                                   | 35   |
| 2.7 Summary . . . . .  | 37   |
| III. Methodology . . . . .   | 38   |
| 3.1 Introduction . . . . .   | 38   |
| 3.2 Simulations . . . . .  | 38   |
| 3.3 Imaging System . . . . .   | 39   |
| 3.4 Simulation Parameters . . . . .  | 41   |
| 3.4.1 Light Levels . . . . .   | 42   |
| 3.4.2 Atmospheric Coherence Diameter . . . . .                             | 44   |
| 3.4.3 Pre-Processing Tilt Correction . . . . .                             | 45   |
| 3.4.4 Wavefront Estimation Technique . . . . .                             | 47   |
| 3.5 Number of Zernike Polynomials . . . . .                                | 47   |
| 3.6 Simulation Matrices . . . . .  | 49   |
| 3.6.1 Point Source Simulations . . . . .                                   | 49   |
| 3.6.2 Extended Object Simulations . . . . .                                | 50   |
| 3.7 Summary . . . . .  | 51   |

|  | Page |
|--|------|
| IV. Results and Analysis . . . . .   | 52   |
| 4.1 Introduction . . . . .   | 52   |
| 4.2 Optimal Number of Zernike Polynomials . . . . .                        | 52   |
| 4.3 Point Source Simulation Results . . . . .                              | 54   |
| 4.3.1 Average Pupil-Averaged Mean Square Residual Phase<br>Error . . . . . | 55   |
| 4.3.2 Average System Transfer Function . . . . .                           | 55   |
| 4.3.3 SNR of System Transfer Function . . . . .                            | 57   |
| 4.3.4 OTF Correlation . . . . .  | 60   |
| 4.4 Extended Object Simulation Results . . . . .                           | 63   |
| 4.4.1 DWFS Demonstration Results . . . . .                                 | 66   |
| 4.4.2 Comparison of LS-Z and MV-Z Object Estimates . . . . .               | 66   |
| 4.5 Implementation . . . . .   | 74   |
| 4.5.1 USAF Optical Sites . . . . .   | 75   |
| 4.6 Summary . . . . .  | 78   |
| V. Conclusions . . . . .   | 80   |
| 5.1 Introduction . . . . .   | 80   |
| 5.2 Summary of Research Advancements . . . . .                             | 80   |
| 5.3 Summary of Results Obtained . . . . .                                  | 81   |
| 5.4 Conclusions Drawn from Research . . . . .                              | 81   |
| 5.5 Recommendations for Future Research . . . . .                          | 82   |
| 5.6 Summary . . . . .  | 82   |
| Appendix A. Programs and Simulation Parameters . . . . .                   | 84   |
| A.1 Computer Programs . . . . .  | 84   |
| A.2 Simulation Input Parameters . . . . .                                  | 84   |



|   | Page |
|---|------|
| Appendix B. Average Pupil-Averaged Mean Square Residual Phase Error Results . . . . . | 86   |
| B.1 Introduction . . . . .  | 86   |
| B.1.1 Effect of Light Level, $m_v$ . . . . .  | 86   |
| B.1.2 Effect of Atmospheric Coherence Diameter, $r_0$ . .                             | 86   |
| B.1.3 Effect of Tilt Removal . . . . .  | 86   |
| B.2 Summary . . . . .   | 86   |
| Appendix C. Average System Transfer Function Results . . . . .                        | 89   |
| C.1 Introduction . . . . .  | 89   |
| C.1.1 Effect of Light Level, $m_v$ . . . . .  | 89   |
| C.1.2 Effect of Atmospheric Coherence Diameter, $r_0$ . .                             | 89   |
| C.1.3 Effect of Tilt Removal . . . . .  | 89   |
| C.2 Summary . . . . .   | 89   |
| Appendix D. System Transfer Function SNR Results . . . . .                            | 98   |
| D.1 Introduction . . . . .  | 98   |
| D.1.1 Effect of Light Level, $m_v$ . . . . .  | 98   |
| D.1.2 Effect of Atmospheric Coherence Diameter, $r_0$ . .                             | 98   |
| D.1.3 Effect of Tilt Removal . . . . .  | 98   |
| D.2 Summary . . . . .   | 98   |
| Appendix E. OTF Correlation Results . . . . .   | 107  |
| E.1 Introduction . . . . .  | 107  |
| E.1.1 Effect of Light Level, $m_v$ . . . . .  | 107  |
| E.1.2 Effect of Atmospheric Coherence Diameter, $r_0$ . .                             | 107  |
| E.1.3 Effect of Tilt Removal . . . . .  | 107  |
| E.2 Summary . . . . .   | 107  |
| Bibliography . . . . .  | 116  |

|                | Page |
|----------------|------|
| Vita . . . . . | 119  |

## *List of Figures*

| Figure  | Page |
|---|------|
| 1. Imaging Simulations . . . . .  | 4    |
| 2. Coordinate System . . . . .  | 12   |
| 3. Aberrated Wavefront . . . . .  | 15   |
| 4. Deconvolution from Wavefront Sensing Block Diagram. . . . .                                | 18   |
| 5. Hartmann Wavefront Sensor . . . . .  | 20   |
| 6. Simulating Deconvolution from Wavefront Sensing. . . . .                                   | 30   |
| 7. Generic Satellite Used for Extended Object Simulations . . . . .                           | 40   |
| 8. Telescope Pupil Geometry . . . . .   | 41   |
| 9. AMOS $m_v$ Historical Data . . . . .   | 44   |
| 10. Variation in $r_0$ . . . . .  | 45   |
| 11. AMOS $r_0$ Historical Data . . . . .  | 46   |
| 12. Wavefront With and Without Tilt Aberration Removed . . . . .                              | 48   |
| 13. Determining the Optimal Number of Zernike Polynomials. . . . .                            | 54   |
| 14. Original, Estimated, and Residual Wavefront Phase . . . . .                               | 56   |
| 15. Average System Transfer Function for $m_v = 4$ , $r_0 = 10$ cm (tilt corrected) . . . . . | 57   |
| 16. Average System Transfer Function for MV-Z Technique . . . . .                             | 58   |
| 17. Average System Transfer Function for MV-Z Technique (tilt corrected) . . . . .            | 59   |
| 18. System Transfer Function SNR for $m_v = 4$ , $r_0 = 10$ cm (tilt corrected) . . . . .     | 60   |
| 19. System Transfer Function SNR for MV-Z Technique . . . . .                                 | 61   |
| 20. System Transfer Function SNR for MV-Z Technique (tilt corrected) . . . . .                | 62   |
| 21. OTF Correlation for $m_v = 4$ , $r_0 = 10$ cm (tilt corrected) . . . . .                  | 63   |
| 22. OTF Correlation for MV-Z Technique . . . . .  | 64   |
| 23. OTF Correlation for MV-Z Technique (tilt corrected) . . . . .                             | 65   |
| 24. LEO Imaging, Range = 500 km, $m_v = 5.37$ , $r_0 = 9.79$ cm . . . . .                     | 67   |

| Figure  | Page |
|---|------|
| 25. GEO Imaging, Range = 35780 km, $m_v = 14$ , $r_0 = 9.79$ cm . . . . .   | 68   |
| 26. LS-Z and MV-Z DWFS Object Estimates; $m_v = 0$ , $r_0 = 10$ cm . . .    | 70   |
| 27. LS-Z and MV-Z DWFS Object Estimates; $m_v = 4$ , $r_0 = 10$ cm . . .    | 71   |
| 28. LS-Z and MV-Z DWFS Object Estimates; $m_v = 8$ , $r_0 = 10$ cm . . .    | 72   |
| 29. LS-Z and MV-Z DWFS Object Estimates; $m_v = 12$ , $r_0 = 10$ cm . . .   | 73   |
| 30. USAF Optical Space Surveillance Sites. . . . .                          | 76   |
| 31. Average System Transfer Function for $m_v = 0$ . . . . .                | 90   |
| 32. Average System Transfer Function for $m_v = 4$ . . . . .                | 91   |
| 33. Average System Transfer Function for $m_v = 8$ . . . . .                | 92   |
| 34. Average System Transfer Function for $m_v = 12$ . . . . .               | 93   |
| 35. Average System Transfer Function for $m_v = 0$ (tilt corrected) . . . . | 94   |
| 36. Average System Transfer Function for $m_v = 4$ (tilt corrected) . . . . | 95   |
| 37. Average System Transfer Function for $m_v = 8$ (tilt corrected) . . . . | 96   |
| 38. Average System Transfer Function for $m_v = 12$ (tilt corrected) . . .  | 97   |
| 39. SNR of System Transfer Function for $m_v = 0$ . . . . .                 | 99   |
| 40. SNR of System Transfer Function for $m_v = 4$ . . . . .                 | 100  |
| 41. SNR of System Transfer Function for $m_v = 8$ . . . . .                 | 101  |
| 42. SNR of System Transfer Function for $m_v = 12$ . . . . .                | 102  |
| 43. SNR of System Transfer Function for $m_v = 0$ (tilt corrected) . . . .  | 103  |
| 44. SNR of System Transfer Function for $m_v = 4$ (tilt corrected) . . . .  | 104  |
| 45. SNR of System Transfer Function for $m_v = 8$ (tilt corrected) . . . .  | 105  |
| 46. SNR of System Transfer Function for $m_v = 12$ (tilt corrected) . . . . | 106  |
| 47. OTF Correlation for $m_v = 0$ . . . . .                                 | 108  |
| 48. OTF Correlation for $m_v = 4$ . . . . .                                 | 109  |
| 49. OTF Correlation for $m_v = 8$ . . . . .                                 | 110  |
| 50. OTF Correlation for $m_v = 12$ . . . . .                                | 111  |
| 51. OTF Correlation for $m_v = 0$ (tilt corrected) . . . . .                | 112  |

| Figure |   | Page |
|--------|---|------|
| 52.    | OTF Correlation for $m_v = 4$ (tilt corrected) . . . . .  | 113  |
| 53.    | OTF Correlation for $m_v = 8$ (tilt corrected) . . . . .  | 114  |
| 54.    | OTF Correlation for $m_v = 12$ (tilt corrected) . . . . . | 115  |

## *List of Tables*

| Table  | Page |
|--|------|
| 1. Imaging System Used for Simulations . . . . .                                       | 42   |
| 2. Values Used for Light Level Calculations . . . . .                                  | 43   |
| 3. Average Photoevents per Frame for Visual Magnitudes . . . . .                       | 43   |
| 4. Point Source Simulation Input Parameters . . . . .                                  | 50   |
| 5. DWFS Demonstration Simulation Input Parameters . . . . .                            | 50   |
| 6. Extended Object Simulation Input Parameters . . . . .                               | 51   |
| 7. Optimal Number of Zernike Polynomials . . . . .                                     | 53   |
| 8. Object Estimate Correlation Coefficient . . . . .                                   | 74   |
| 9. On-object Resolution . . . . .  | 74   |
| 10. USAF Electro-Optical Telescopes . . . . .  | 77   |
| 11. Simulation Programs . . . . .  | 85   |
| 12. Simulation Input Parameters . . . . .  | 85   |
| 13. Average Pupil-Averaged Mean Square Residual Phase Error . . . . .                  | 87   |
| 14. Average Pupil-Averaged Mean Square Residual Phase Error (tilt corrected) . . . . . | 88   |

### *Abstract*

A cost effective method to improve the space surveillance mission performance of United States Air Force (USAF) ground-based telescopes is investigated and improved. A minimum variance wavefront estimation technique is used to improve Deconvolution from Wavefront Sensing (DWFS), a method to mitigate the effects of atmospheric turbulence on imaging systems that does not require expensive adaptive optics. Both least-squares and minimum variance wavefront phase estimation techniques are investigated, using both Gaussian and Zernike polynomial elementary functions. Imaging simulations and established performance metrics are used to evaluate these wavefront estimation techniques for a one-meter optical telescope. Performance metrics include the average pupil-averaged mean square phase error of the residual wavefront, the average system transfer function, the signal-to-noise ratio (SNR) of the system transfer function, and the optical transfer function correlation. Results show that the minimum variance estimation technique that employs Zernike polynomial elementary functions offers improvements over all other estimation techniques in each of the performance metrics. Extended object simulations are also conducted which demonstrate the improvements in image quality and resolution that result from the modifications to the DWFS method. Implementation of the DWFS method into USAF space surveillance telescopes is investigated.

# DECONVOLUTION FROM WAVEFRONT SENSING USING OPTIMAL WAVEFRONT ESTIMATORS

## *I. Introduction*

### *1.1 The Problem: Imaging Through Atmospheric Turbulence*

Gathering information about space objects from the ground is an essential element of the United States Air Force (USAF) space surveillance mission. There are several factors, however, that make ground-based remote sensing of space objects difficult. First, the objects are hundreds of kilometers to tens of thousands of kilometers away from the imaging system. For passive imaging, the only light detected is that which is reflected off the objects by the sun or that which is radiated from the objects themselves. This results in dim objects with low signals. Second, the received signal is highly dependent on variations in object shape, orientation, material properties, and solar angles. Third, the Earth-orbiting objects must be tracked, and the laws of orbital mechanics and the location of the observing site often limit the opportunities for observation (3). Fourth, the best observing times for a particular telescope are limited to dawn and dusk when the object is illuminated by the sun and the telescope is in the darkness. Fifth, telescopes can only operate effectively under a dark and clear sky. Finally, turbulent motion in the upper atmosphere imposes a fundamental limit on the resolution of the image. This thesis investigates a method to mitigate the effects of atmospheric turbulence.

The quality, and therefore usefulness, of an image obtained with a ground-based optical telescope depends on the quantity and properties of the reflected light that eventually reaches the telescope from the object. The best image occurs when the amount of light received is maximized and when unwanted signals and interfer-



ence are minimized. Unwanted signals arise from detector noise, photon shot noise, and light pollution. Interference can occur when the signal interacts with dust particles, pollutants, clouds, humidity, and atmospheric turbulence. Observing sites can mitigate against some of these undesirables by using low-noise detectors and by building large telescopes on the tops of mountains and under dark and clear skies. Atmospheric turbulence, however, presents a more difficult problem and is addressed in this thesis. A telescope's light-gathering power is proportional to the square of its aperture diameter. However, in terms of the ability to resolve objects, today's biggest telescopes are reduced to the effectiveness of telescopes with apertures on the order of tens of centimeters due to the aberrations imposed by the atmosphere (29).

### *1.2 Mitigation Methods*

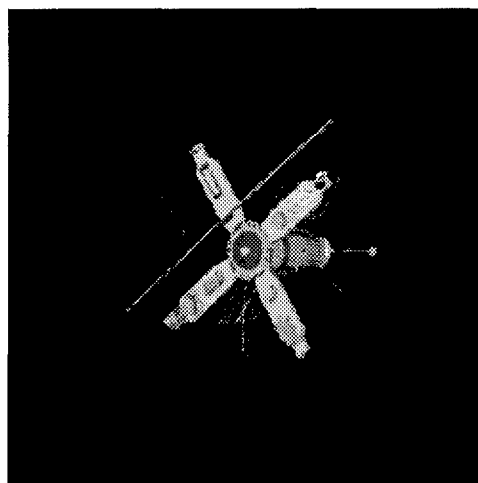
One way to overcome the problem that atmospheric turbulence presents to ground-based imaging of space objects is to operate the telescope in space. However, space-based telescopes are expensive, limited by the size of the launch vehicle (17), few in number, and present a new set of object acquisition difficulties because of orbital mechanics. Ground-based telescopes are not limited by size or power like space-based telescopes but they must deal with the adverse effects of atmospheric turbulence. There are several techniques currently available for ground-based telescopes to overcome the adverse effects of the atmosphere. These techniques can be placed in three broad categories. First, pre-detection or adaptive optics (AO) techniques incorporate the use of mechanical means to compensate for the effects of turbulence before the image is detected. Second, purely post-processing techniques are used to deconvolve the combined atmosphere-telescope system aberrations from the image after the image is detected. And third, hybrid techniques combine elements of both adaptive optics and post processing (29).

The upper bound to image quality is known as the diffraction-limited image. The diffraction limit is a function of the imaging wavelength and the size of the

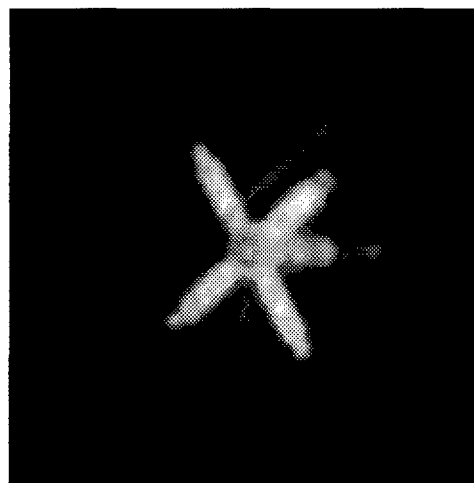
telescope, and is due to the telescope system alone. The atmosphere imposes a further limit that is more severe than the diffraction limit (29). Of course, the ideal turbulence mitigation technique could, at best, only achieve diffraction-limited performance. Additionally, it has been shown that the aberrations resulting from atmospheric turbulence never improve the performance of optical imaging systems beyond the diffraction limited case (11). There are several fundamental limitations that keep turbulence mitigation techniques from reaching ideal diffraction-limited performance. These include the finite light levels arriving at the sensor, differences between object aberrations and sampled aberrations, finite spatial sampling of the wavefront, and for AO systems, finite temporal response and finite number of degrees of freedom of the deformable mirror and actuator system (29).

Figure 1 demonstrates the performance degrading effects of atmospheric turbulence and the significant improvement that is possible with the turbulence mitigation method developed in this thesis. Frame (a) is a computer graphics rendering of a generic satellite which is the object to be imaged. Frame (b) is the diffraction-limited image for a one-meter telescope operating at visible wavelengths. Frame (c) shows the image for the telescope without correcting for the aberrations imposed by atmospheric turbulence. Frame (d) is the corrected image using the technique developed in this thesis.

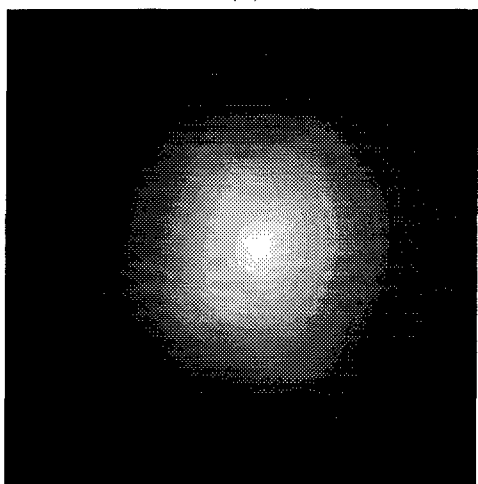
What causes the degradation of these images? A distant object produces a spherical wavefront and at long distances from the source this wavefront becomes effectively planar. Meanwhile, temperature fluctuations in the Earth's atmosphere cause the index of refraction of the air to change randomly in both space and time. When the planar wavefront passes through the atmospheric turbulence, it becomes distorted. The distortions arise because the propagation velocities of different portions of the wavefront are altered due to turbulence-induced variations in the index of refraction. This results in random phase aberrations which appear at the telescope pupil, severely degrading image resolution.



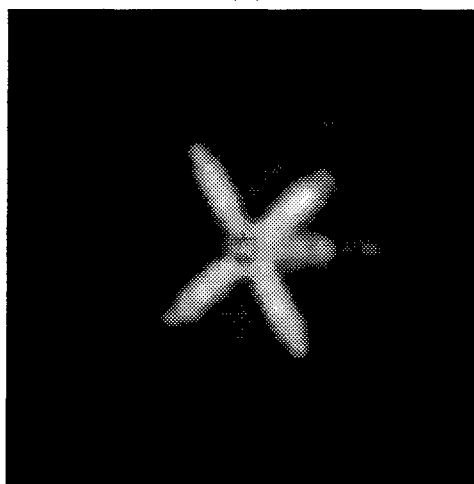
(a)



(b)



(c)



(d)

Figure 1. Imaging Simulations: Effects of Atmospheric Turbulence on Imaging. (a) Computer Rendering of a Generic Satellite, (b) Diffraction Limited Image, (c) Uncorrected Image, (d) Corrected Image.

Resolution is intimately tied to image quality and the amount of information one can gather from an object. Seyrafi defines four basic levels of information for remote sensing. These can be considered levels of usefulness for the data. *Detection* involves the ability to determine that something is there. *Orientation* involves the ability to determine the view or pose of the object. *Recognition* involves the ability to determine the type or class of object. For the case of space objects this could be active or inactive satellites, spent rocket stages, or debris. *Identification* involves the ability to discriminate between objects within a particular class (32). A progression from one usefulness category to the next requires improvements in resolution. Improvements in resolution can increase the ability to detect objects, determine their orientation, recognize their type, and perform identification. All of these are important elements of the USAF space surveillance mission.

The USAF operates several optical telescopes as part of a larger network of ground-based sensors designed to detect, track, identify and maintain orbital element sets for all man-made objects in space. Collectively, these sensors function to monitor, assess and inform (20). High resolution images of the objects are used to monitor the space object population and special events, make assessments of missions and threats for a user base, and provide information on routine space operations such as new launch processing, insertion maneuvers, and satellite decay and de-orbit. Space surveillance network sensors also provide data for collision hazard assessments and satellite breakup analysis (16). Atmospheric turbulence severely limits the ability of the USAF to obtain quality images of space objects from ground-based optical telescopes. Also, recent mission area plan deficiencies for USAF space surveillance that could be addressed with the implementation of atmospheric turbulence mitigation techniques include limited space intelligence support, incomplete space object catalog, and high operations and maintenance costs (19).

### *1.3 Deconvolution from Wavefront Sensing*

Deconvolution from Wavefront Sensing (DWFS) is the atmospheric turbulence mitigation technique that is the subject of this thesis. DWFS is a hybrid technique (29) that can be used to mitigate the effects of atmospheric turbulence on imaging systems without using the expensive components of adaptive optics (AO). In DWFS, information from wavefront sensor (WFS) measurements of a series of spatially and temporally random incoming aberrated wavefronts is stored along with each wavefront's corresponding image. Various techniques are then employed that use the WFS measurements to estimate the form or shape of the incoming wavefronts. With a phase estimate, estimates of the instantaneous optical transfer function (OTF) of the telescope-atmosphere system are made. This estimated OTF can then be used in a deconvolution procedure to estimate the object intensity distribution (29). DWFS has been shown to improve image resolution (15, 24, 29). One disadvantage of the DWFS method compared to adaptive optics methods is that real-time imaging is not possible with DWFS because of the post-processing requirement. Also, the resolution of object estimates obtained using DWFS are inherently worse than AO object estimates. Real-time AO systems can be more effective in removing distortions. This is because the averaging used by DWFS acts to smooth out the image. However, DWFS is less mechanically demanding and much cheaper than AO and less computationally demanding than post-processing techniques such as speckle interferometry (24, 29). Also, DWFS can be used in concert with adaptive optics systems (24).

### *1.4 Problem Statement*

This thesis investigates improving the hybrid atmospheric turbulence mitigation technique known as deconvolution from wavefront sensing by incorporating a minimum variance wavefront estimation technique that employs two-dimensional Gaussian and Zernike polynomial elementary functions. This minimum variance

technique uses the known statistics of turbulence and measurement noise to develop an optimal wavefront estimate.

### 1.5 Current Knowledge

Past work in the areas of DWFS and wavefront reconstruction has laid the foundation for this thesis. The basic concept of deconvolution from wavefront sensing as a technique to mitigate turbulence effects was first introduced in 1987 by Fried who called it *post-detection wavefront compensation* (7). In 1990, Primot coined the name DWFS and was the first to produce experimental verification. Primot used a least-squares reconstruction technique that incorporated the use of Zernike polynomial influence functions (24). Least-squares estimation does not account for turbulence and measurement noise statistics. Wallner introduced an optimal (minimum variance) control law for adaptive optics in 1983 that accounted for the known statistics of the measured wavefront when estimating the wavefront phase (34). In 1989, Welsh and Gardner investigated the mean square phase error performance of the least-squares and minimum variance wavefront reconstruction techniques for adaptive optics systems (36). In 1992, Roggemann investigated the least-squares and minimum variance reconstruction techniques for an adaptive optics system and showed that the minimum variance technique with Gaussian influence functions was superior to the least-squares technique with Gaussian influence functions in terms of signal-to-noise and optical transfer function performance (26). In 1994, Roggemann, Welsh, and Devey reported an unnoticed bias in the DWFS least-squares estimation technique which caused nonrandom errors in the object estimate (31). This thesis is the first to incorporate minimum variance phase estimation techniques into the DWFS method.

## *1.6 Scope*

In this thesis, DWFS performance is improved by incorporating minimum variance wavefront estimation techniques. These techniques are compared with two other existing least-squares wavefront estimation techniques. A variety of metrics including average pupil-averaged mean square residual phase error, average system transfer function, image and system transfer function signal-to-noise ratio, and average OTF correlation are used to quantify performance. Imaging simulations are also used to demonstrate and quantify the improvements in image quality that DWFS offers. Also, implementation of the DWFS method into existing USAF telescopes is explored.

## *1.7 Approach*

Computer programs are used to simulate the imaging process. A series of simulations is conducted for point source objects and extended objects to quantify the sensitivity of the optical performance of the various wavefront estimation techniques to variations in telescope operational conditions (including light levels and atmospheric turbulence levels). Established performance metrics are used to quantify the performance of each technique.

## *1.8 Research Objectives*

The following research objectives were to be accomplished in this thesis:

1. Implement minimum variance wavefront estimation techniques for the deconvolution from wavefront sensing (DWFS) method that makes use of two-dimensional Gaussian and Zernike polynomial elementary functions.
2. Compare these wavefront estimation techniques with existing least-squares DWFS wavefront estimation techniques and quantify the performance of each technique.

3. Test the performance of a typical imaging system using each DWFS wavefront estimation technique for a variety of light and turbulence levels.
4. Demonstrate and quantify the improvements in telescope performance that the modified DWFS method can bring for typical imaging scenarios.
5. Investigate the implementation of DWFS into USAF ground-based optical telescopes.

### *1.9 Key Results*

- The deconvolution from wavefront sensing atmospheric turbulence mitigation method was modified by incorporating minimum variance wavefront estimation techniques that employed two-dimensional Gaussian and Zernike polynomial elementary functions.
- The minimum variance technique that used Zernike polynomial elementary functions was shown to provide lower residual error and superior OTF, signal-to-noise ratio, and image quality over previous wavefront estimation techniques.
- Simulations were conducted that demonstrated and quantified the improvement in telescope performance that the DWFS techniques can bring to space object imaging.
- A preliminary analysis showed that implementing DWFS into existing USAF ground-based telescopes would serve to reduce USAF space surveillance deficiencies in a cost effective manner by increasing the number of surveillance assets capable of providing intelligence support and improving the space object catalog.



### *1.10 Thesis Organization*

The remainder of this thesis is organized as follows: Chapter II discusses the theory that is used in this research in the areas of imaging, atmospheric turbulence, and deconvolution from wavefront sensing. Chapter III describes the basic methodology employed in the research. Chapter IV presents and analyzes the results obtained in this research, and finally Chapter V summarizes the entire thesis and presents conclusions.

## II. Theory

### 2.1 Introduction

This chapter presents a background for the theory used in this thesis. These theoretical foundations can be categorized into three areas: imaging system theory, atmospheric turbulence theory, and the theory relating to the method of Deconvolution from Wavefront Sensing (DWFS). Underpinning each of these areas are the mathematical tools and disciplines of Fourier analysis, statistical optics, and linear shift invariant systems. Additionally, the theory behind each of the metrics used to evaluate imaging system performance is presented.

### 2.2 Imaging System Theory

The act of remotely imaging a distant object involves measuring the light intensity distribution from the object at the location of the imaging system. Because of things that are happening between the object and the imaging focal plane, these two distributions will be very different. It is the *stuff* in the middle that acts to make the image distributions different (worse) from the original object distribution. This *stuff* includes the physical imaging system itself and the aberrating media between the object and the imaging system. Collectively the *stuff* can be considered a system through which the light wave propagates and the resulting image is formed. Fortunately, from a modeling point of view, optical imaging systems obey a conventional linear shift invariant system framework whereby the optical system acts to linearly map the light intensity distributions from the object to the light intensity distributions of the image (11). For the problem of a ground-based telescope imaging objects in space through the atmosphere, the system is a combination of the telescope apparatus and the atmosphere.

This thesis is concerned with the adverse effects that atmospheric turbulence has on the quality of images. The coordinate system that will be used for the con-

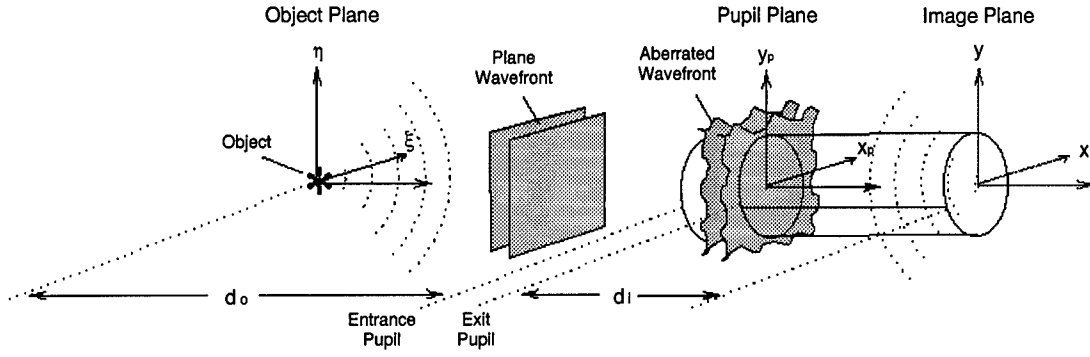


Figure 2. Coordinate System.

cepts and equations in this thesis is defined in Figure 2. Characteristics of the light intensity distributions can be described at different planes as the light propagates from the object to the image. The object plane has the coordinates  $(\xi, \eta)$ , the pupil plane is denoted with the coordinates  $(x_p, y_p)$  and the image plane is denoted with the coordinates  $(x, y)$ . The distance from the object plane to the entrance pupil is  $d_o$  and the distance from the exit pupil to the image plane is  $d_i$ .

The linear shift invariant (LSI) model for noiseless incoherent imaging presents a relationship between the image intensity distribution, the object intensity distribution, and the system point spread function. Let  $i(\vec{x})$  be a short exposure, noise-free image intensity distribution of an imaging system. The vector  $\vec{x}$  represents a point on the image in the  $(x, y)$  plane. The image intensity distribution is given by the convolution of the object intensity distribution,  $o(\vec{x})$ , and the point spread function,  $h(\vec{x})$  (11).

$$i(\vec{x}) = o(\vec{x}) * h(\vec{x}) \quad (1)$$

Here, the asterisk,  $*$ , represents the two-dimensional convolution. Using the definition of convolution (11), this expression takes the form

$$i(x, y) = \iint_{-\infty}^{\infty} o(\xi, \eta) h(x - \xi, y - \eta) d\xi d\eta \quad (2)$$

Fortunately, Fourier analysis methods can greatly simplify the mathematics. The Fourier transform  $G(\vec{f})$  of a function  $g(\vec{x})$  is defined as (8)

$$G(\vec{f}) = \int g(\vec{x}) \exp\{-j2\pi\vec{f} \cdot \vec{x}\} d\vec{x}. \quad (3)$$

Fourier analysis tools allow one to work in terms of spatial frequency or what is referred to as the *frequency domain*. Here,  $\vec{f}$  is a two dimensional spatial frequency coordinate which in the image plane contains the  $x$  and  $y$  directed frequency components  $(f_x, f_y)$ . In the frequency domain, the complicated two-dimensional convolution integral (Equation 2) is replaced by a simpler relationship involving only multiplication. Taking the Fourier transform of each side of Equation 1, one gets

$$I(\vec{f}) = O(\vec{f}) H(\vec{f}). \quad (4)$$

Here,  $I$ ,  $O$ , and  $H$  are the Fourier transforms of  $i$ ,  $o$ , and  $h$ , respectively.  $I(\vec{f})$  is the image spectrum,  $O(\vec{f})$  is the object spectrum, and  $H(\vec{f})$  is the optical transfer function (OTF). The OTF is a two-dimensional function of spatial frequency that represents the effects of the system in the spatial frequency domain and acts as a low pass filter which attenuates the high spatial frequency components of a signal. Usually it is easier to perform convolutions in the spatial frequency domain using the Fast Fourier Transform (FFT) (11).

### 2.3 Atmospheric Turbulence Theory

As discussed in Chapter I, atmospheric turbulence imposes a fundamental limit on the resolution of ground-based imaging systems. This section describes why this happens. Turbulent motion in the upper atmosphere resulting from differential heating of features on the Earth's surface causes an inhomogeneous temperature distribution in the atmosphere. This, in turn, causes the air to move and makes the index of refraction of the air a random quantity that varies in both space and time.

For visible wavelengths, spatial variations have been observed to occur at angular separations of 5 to 10  $\mu\text{rad}$  as viewed from the ground (29). For a given spatial sample, time-scale variations occur on the order of several 10s of to a few hundred times per second (29). For an imaging wavelength equal to 0.5  $\mu\text{m}$  the differential variation of the index of refraction,  $n$ , is

$$dn = \frac{-77.6P}{T^2} \times 10^{-6} dT, \quad (5)$$

where  $P$  is the pressure in millibars,  $T$  is the temperature in degrees Kelvin,  $dT$  is the incremental change in temperature, and  $dn$  is the incremental change in the index of refraction (29). Light propagating a distance  $z_i$  through free space ( $n = 1$ ) is retarded by the factor  $2\pi z_i/\lambda$ , where  $\lambda$  is the imaging wavelength. When the index of refraction is not uniform, the light is retarded by  $2\pi n z_i/\lambda$ . Prior to interaction with the atmosphere the wavefront is a plane wave with constant phase. The turbulence-induced aberrations manifest themselves as spatial changes in the phase of the incoming wavefront. When the wavefront passes through a spatially random atmosphere of thickness  $z_b - z_a$ , its phase is spatially affected according to (29)

$$\Delta\psi(\vec{x}) = \frac{2\pi}{\lambda} \int_{z_a}^{z_b} n(\vec{x}, z) dz. \quad (6)$$

As was previously mentioned, the effect of the atmosphere is equivalent to an aberration in the pupil plane,  $(x_p, y_p)$ , of the telescope. Atmospheric turbulence causes the optical transfer function to be a random process. As a result, the average OTF is narrow and the point spread function of the imaging system is broad and smooth (29). Variations in amplitude (known as scintillation) are ignored because the “near field” assumption is made where refraction due to propagation through turbulence is ignored. This implies that only phase perturbations exist and that they do not evolve into both phase and amplitude perturbations (29).

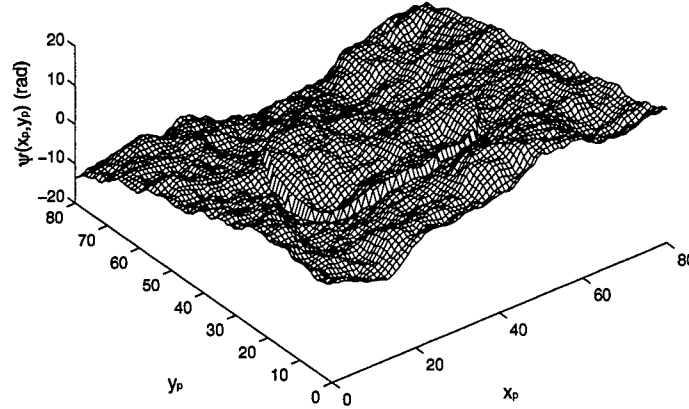


Figure 3. Aberrated Wavefront.

**2.3.1 Signal.** The purpose of remote sensing is to gather information about an object from the electromagnetic radiation that is scattered off or self-emitted from the object. This electromagnetic radiation, or *signal*, propagates from the distant object as a spherical wavefront. At large separations between the object and the imaging system, this spherical wavefront is effectively planar by the time it reaches the receiving aperture. A *wavefront* is a spatial representation of the phase of a propagating wave and is an important concept for this study. A planar wavefront is a surface of constant phase and an aberrated wavefront is a surface of spatially-varying phase. If there were no interference from the atmosphere, these wavefronts would continue to be planar. Instead, atmospheric turbulence causes aberrations in the wavefronts. Phase screens are individual time slices of the spatially-varying wavefronts that enter the imaging system aperture. A typical rendering of an aberrated wavefront is shown in Figure 3. This particular example shows the spatial variation in phase angle (measured in radians) for the wavefront in the pupil plane  $(x_p, y_p)$ .

**2.3.2 Measurement Noise.** Equation 4 shows the relationship between the image and object spectrums for a LSI imaging system that is noiseless. However, in

the real world, no image is free of noise. In general, noise is any unwanted signal and affects the confidence in a measurement (29). Types of noise include shot noise and detector read noise. Shot noise arises due to the inherent randomness of the optical detection process for sources of finite brightness. It occurs because of the random arrival times and locations of photons on a detector. Because shot noise obeys Poisson statistics, the mean and variance of the random variable are the same. It will be shown later that wavefront sensor errors arise from shot noise and the finite sampling of the WFS over the pupil aperture (36). Detector read noise is an additive noise that arises from specific detector configurations (35). The noise model used in this thesis is described in Section 2.4.1.1.

*2.3.3 Signal to Noise Ratio.* The signal-to-noise ratio (SNR) is a measure of the proportional amounts of signal and noise contained in a particular message. In general, the SNR of any random quantity can be defined as the mean or expected value of that random quantity divided by the random quantity's standard deviation (37). The variance of a random quantity,  $Q(\vec{f})$ , is given by

$$\text{var}\{Q(\vec{f})\} = \langle |Q(\vec{f})|^2 \rangle - |\langle Q(\vec{f}) \rangle|^2, \quad (7)$$

where,  $|\cdot|$  denotes absolute value and  $\langle \cdot \rangle$  denotes expected value (10). Thus, the SNR of the random quantity,  $Q(\vec{f})$ , is given by (29)

$$\text{SNR}_{Q(\vec{f})}(\vec{f}) = \frac{|\langle Q(\vec{f}) \rangle|}{\sqrt{\text{var}\{Q(\vec{f})\}}}. \quad (8)$$

With this definition, the SNR can be seen as a measure of the uncertainty of a quantity with respect to its expected value. The existence of randomness in a measurement will decrease the SNR. A large value of the SNR implies the quantity is not expected to deviate too much from its mean value. If there were no noise one would have an infinite SNR and, for the application of imaging, a perfect image. For

low values of SNR below certain threshold values, it becomes difficult to distinguish the signal from the noise. A total of  $I$  uncorrelated measurements will increase the SNR by a factor of  $\sqrt{I}$  (27).

For the problem of imaging through atmospheric turbulence, the OTF,  $H(\vec{f})$ , and image,  $I(\vec{f})$ , are random quantities. Thus, one can speak of the SNR of these quantities. Also, after deconvolution, one can look at the SNR of the estimated object spectrum,  $\tilde{O}(\vec{f})$ . Equations for the SNR of the various quantities used in this thesis are defined in Section 2.6.3.

## 2.4 Deconvolution from Wavefront Sensing Theory

Deconvolution from Wavefront Sensing (DWFS) is a hybrid technique that is used to mitigate the effects of the atmosphere on imaging. DWFS has been shown to improve images by providing sharper pictures and higher resolutions (15, 24, 29). As was previously discussed in Chapter I, hybrid imaging techniques combine some aspect of adaptive optics and post-processing techniques. The AO elements required by DWFS are a wavefront sensor and a reference beacon. Figure 4 provides an overview of the DWFS process. Light from a distant object is aberrated by the atmosphere/telescope system. Within the telescope, a high speed shutter is used to capture many short exposure images of the object. A beam splitter is then used so that simultaneous measurements can be made by a wavefront sensor and an imaging camera. For each short exposure the wavefront sensor measures the aberrations of the incoming wavefront,  $\psi(\vec{x}_p)$ , of a reference beacon (either natural or artificial), and the imaging camera records the corresponding image of the object (29). These measurements are stored for later processing. During the processing, a computer uses the wavefront sensor measurements to come up with an estimate of the phase,  $\tilde{\psi}(\vec{x}_p)$ . This phase estimate is combined with the telescope pupil function to create an estimate of the generalized pupil function. The generalized pupil function is used to generate an estimate of the OTF,  $\tilde{H}(\vec{f})$ . A deconvolution procedure is then used to



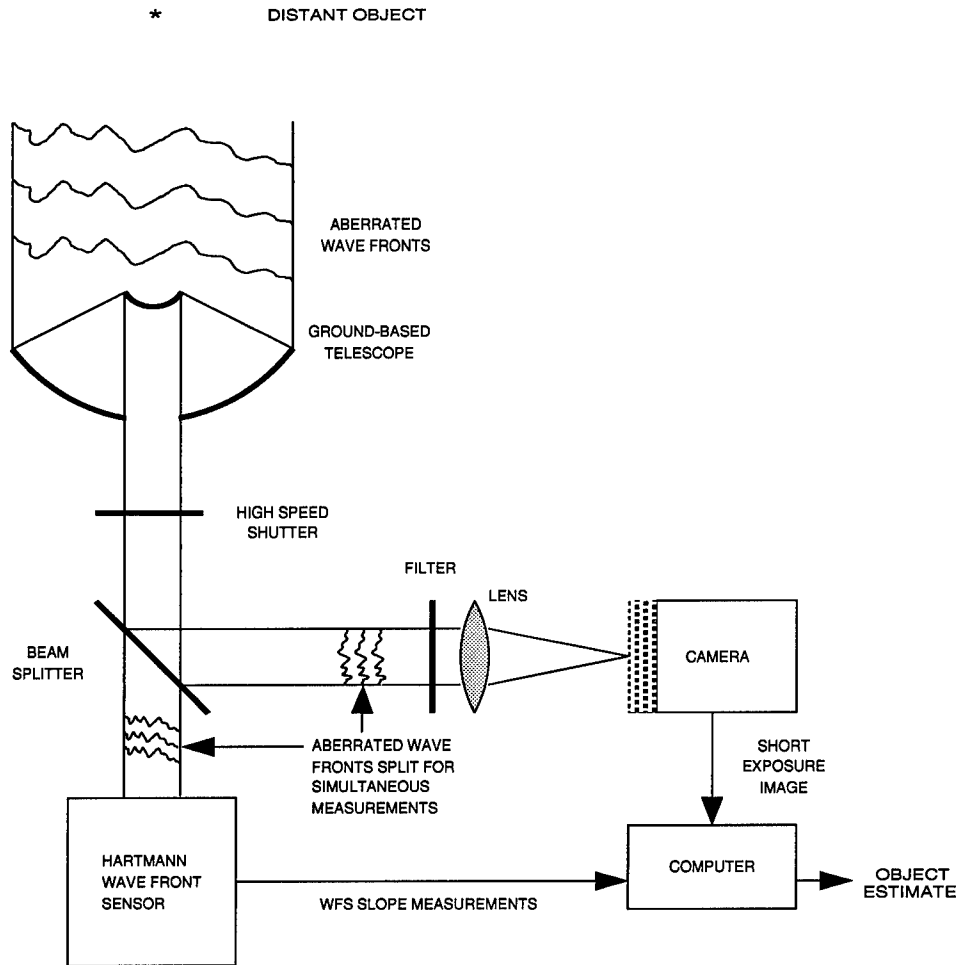


Figure 4. Deconvolution from Wavefront Sensing (DWFS) Block Diagram (29).

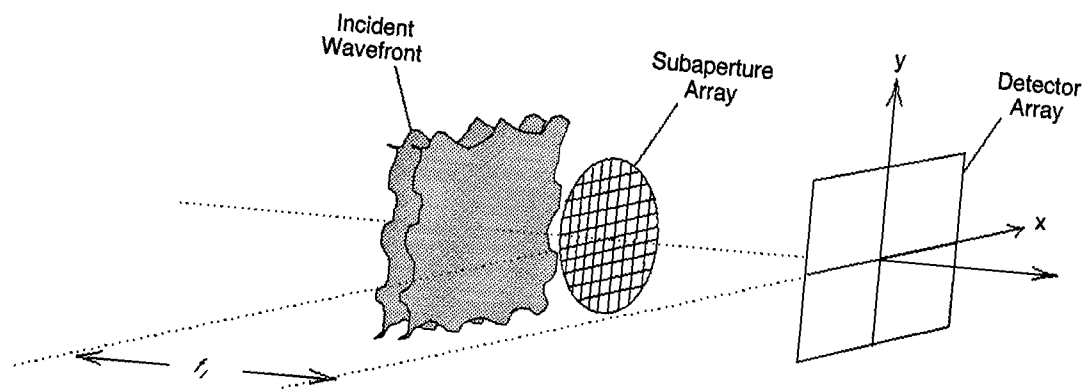
get an estimate of the object spectrum,  $\tilde{O}(\vec{f})$ , and the inverse FFT is used to get an estimate of the object intensity distribution,  $\tilde{o}(\vec{x})$ . Note that the SNR is improved by using hundreds of realizations. In the sections that follow, the theory behind the wavefront sensor, phase estimation techniques, and deconvolution procedure is discussed.

**2.4.1 Wavefront Sensor.** A wavefront sensor (WFS) is a piece of equipment that is used to measure the phase distortions of the incoming wavefronts. The signals that are measured by the wavefront sensor come from a reference beacon, traditionally a nearby star. One problem often faced is finding a bright enough star in

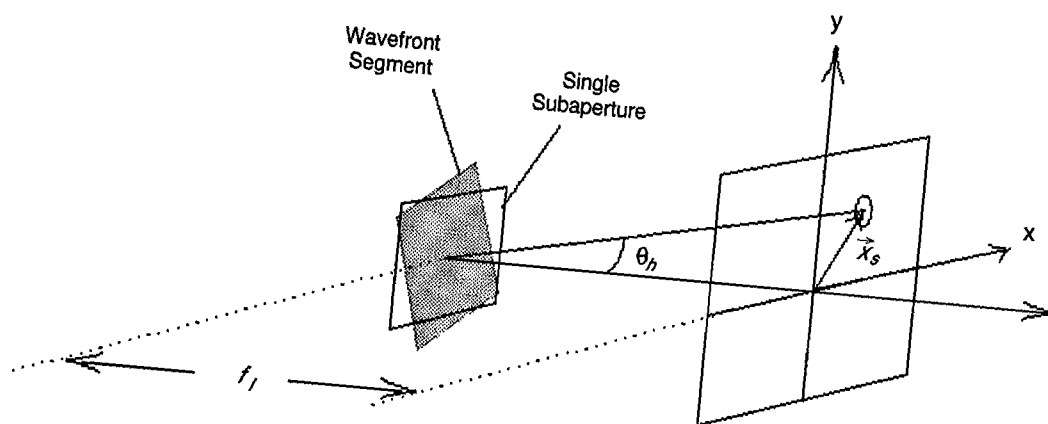
the region of the sky close to the object of interest to sample the regional turbulence effects adequately. The existence of spatial differences in the atmospheric turbulence over a particular sampled region is known as *anisoplanatism*. Artificial beacons that use lasers have been recently developed to overcome this limitation. Laser light is scattered off the atmosphere directly above the telescope pupil. The scattered light is used by the WFS to measure the turbulence-induced aberrations in the wavefront. The WFS measures the wavefront phase by measuring the slope or tilt in small sections of the wavefront. For this study a Hartmann WFS is used because it has been shown to perform better than other wavefront sensors for imperfect seeing conditions and for extended beacons (35). These correspond to realistic telescope operational conditions. Diagrams depicting the Hartmann WFS are shown in Figure 5. This figure shows how the Hartmann WFS spatially separates the incoming aberrated wavefront. Each of the segments on the telescope pupil is called a subaperture. Each subaperture samples the average tilt of the wavefront in its particular region. As shown in frame (b) of Figure 5, across a given subaperture, the wavefront will have an average tilt which is effectively a plane wave incident on the subaperture. The image produced on each detector will be the diffraction pattern offset in a manner directly related to the tilt of the wavefront section. The vector  $\vec{x}_s$  corresponding to the centroid of each spot can then be determined and recorded. From here, the wavefront slope can be obtained for the entire sampled wavefront. The tilt at each subaperture is determined by finding the offset of the spot on the detector focal plane. The wavefront tilt,  $\theta_h$ , is related to the location of the spot by the following relationship (35)

$$\theta_h = \tan^{-1} \left( \frac{|\vec{x}_s|}{f_l} \right). \quad (9)$$

Here,  $f_l$  is the focal length of the subaperture lens, and  $\vec{x}_s$  is the spot location which is determined by detecting the location on the subaperture detector with the highest intensity.



(a)



(b)

Figure 5. Hartmann Wavefront Sensor (a) Entire Wavefront (b) Single Subaperture.

*2.4.1.1 WFS Model.* In the real world the noise-corrupted slope sensor data would be in the output of the WFS. However, for this study a model is required to simulate the noisy readout from a wavefront sensor. Fundamental performance limits of a WFS include the finite sampling of the WFS over the pupil area, shot noise, and detector read noise (35, 36). This model takes the original phase  $\psi(\vec{x}_p)$  as input and adds noise. The WFS slope of the  $i$ th realization for the  $n$ th subaperture is given by (29)

$$s_i(n) = - \int \nabla^q W_n(\vec{x}_p) \psi_i(\vec{x}_p) d\vec{x}_p + \vec{s}_{noise}(n), \quad (10)$$

where the integral term represents the noise-free slope measurement of the  $i$ th realization for the  $n$ th subaperture and the last term is a random vector that describes system noise.  $\nabla^q$  is the  $q$  component of the spatial gradient operator and  $q$  indicates either the  $x$  or  $y$  direction.  $W_n(\vec{x}_p)$  is the  $n$ th subaperture weighting function (29). The WFS noise,  $\vec{s}_{noise}(n)$ , for each subaperture is modeled by considering its variance,  $\sigma_{noise}^2$ . The variance of the system noise variable combines the variance of the shot noise,  $\sigma_{shot}^2$ , and the variance of the detector read noise,  $\sigma_{read}^2$  (29)

$$\sigma_{noise}^2 = \sigma_{shot}^2 + \sigma_{read}^2. \quad (11)$$

Recall that a reference beacon is used with a WFS to estimate the phase of the incoming wavefront. For a Hartmann WFS using an ideal quad-cell detector, the standard deviation of the location error due to shot noise in radians per meter is given as (29, 35)

$$\sigma_{shot} = \frac{\sqrt{2} \pi}{\sqrt{\bar{K}_{WFS} \int_{-1}^1 I_b(f_{x_p}, 0) H(f_{x_p}, 0) df_{x_p}}}, \quad (12)$$

where  $H(f_{x_p}, f_{y_p})$  is the tilt-removed OTF for a particular subaperture,  $\bar{K}_{WFS}$  is the average number of photoevents per frame for a subaperture and  $I_b(f_{x_p}, 0)$  is the

beacon spectrum which is given by

$$I_b(\vec{f}) = \exp \left[ -\pi^2 |\vec{f}|^2 \left( \frac{\sigma_b/z_b}{\lambda/r_0} \right)^2 \left( \frac{d}{r_0} \right)^2 \right], \quad (13)$$

for a Gaussian beacon and  $\sigma_b$  is the root mean square size of the beacon at  $z_b$ , the altitude of the beacon,  $\lambda$  is the imaging wavelength,  $r_0$  is the atmospheric coherence diameter and  $d$  is the square subaperture dimension. And finally, the standard deviation of the read noise is expressed as

$$\sigma_{read} = \frac{\sqrt{2} \pi}{d \sqrt{\bar{K}_{WFS}^2 / 4 \sigma_e^2}}. \quad (14)$$

Here,  $\sigma_e^2$  is the variance of the electronic noise for each pixel in the quad cell detector array and has the units of photoelectrons squared (29).

*2.4.2 Phase Estimation for DWFS.* An integral part of DWFS, and for that matter any atmospheric turbulence mitigation technique, is the estimate of the incoming wavefront that is made from the WFS measurements. For non-AO systems such as DWFS this process is referred to as wavefront *phase estimation*<sup>1</sup>.

In DWFS, information required to compute the phase estimate is provided by the wavefront sensor. The slope of the  $n$ th subaperture is given by Equation 10. Recall that for each subaperture the wavefront sensor measures the slope of the tilt in the  $x$  and  $y$  directions in the image plane. Thus, the slope for the  $n$ th subaperture is represented by a two-dimensional vector with one value for the  $x$  direction and the other value for  $y$  direction. As described in References (26, 29, 30), the estimate of the incident phase,  $\tilde{\psi}(\vec{x}_p)$ , can be written as a linear combination of elementary

---

<sup>1</sup>Note that phase estimation is also used when modeling the processes undertaken by AO systems. In this context it is referred to as *phase reconstruction* and the elementary functions are called *influence functions* (26, 29). In AO systems the reconstruction matrix (or control matrix) is used to determine the actuator control signals for the command actuators. The actuators move to form the mirror surface to the appropriate shape.

functions  $e_j(\vec{x}_p)$

$$\tilde{\psi}(\vec{x}_p) = \sum_{j=1}^J c_j e_j(\vec{x}_p), \quad (15)$$

where  $c_j$  is the weight associated with each of the  $J$  elementary functions. The weights,  $c_j$ , are given by

$$c_j = \sum_{n=1}^{2N} M_{jn} s_n. \quad (16)$$

Here,  $M_{jn}$  is the reconstruction matrix,  $s_n$  is the slope sensor measurement for the  $n$ th subaperture, and  $N$  is the number of subapertures. This thesis looks at two methods to compute  $M_{jn}$  (least-squares and minimum variance) and two choices for the elementary functions,  $e_j(\vec{x}_p)$ , (Gaussian and Zernike polynomials). Collectively, the four techniques will be abbreviated in the following manner: Least-squares with Gaussian elementary functions (LS-G), least-squares with Zernike polynomial elementary functions (LS-Z), minimum variance with Gaussian elementary functions (MV-G), and minimum variance with Zernike polynomial elementary functions (MV-Z). It is the computation of  $M_{jn}$  that distinguishes the least-squares and minimum variance estimation techniques that are described in the next sections.

*2.4.2.1 Least-Squares Estimation.* The least-squares (LS) wave-front phase estimation technique has been used in both AO and DWFS methods (15, 24, 29, 34). The least-squares technique does not consider statistics of atmospheric turbulence or WFS noise (26). It assumes that the WFS measurements are noiseless (29). Because it does not consider prior knowledge of statistics, it is the simplest and most commonly employed phase-estimation/reconstruction technique. The LS technique minimizes the mean square sum of values of the error,  $\Delta$ , between the WFS slope measurements and the slopes from a phase estimate constructed from a linear combination of elementary functions (26). This error is given by

$$\Delta = \vec{s} - H\vec{c}, \quad (17)$$

where  $\vec{s}$  is a column vector of WFS slope measurements and  $\vec{c}$  is a column vector of elementary function weights.  $H$  is a Jacobian matrix with elements

$$h_{nj} = \frac{\partial s_n}{\partial c_j}. \quad (18)$$

The optimal value for  $\vec{c}$  is determined by setting the derivative of  $\Delta^T \Delta$  with respect to  $c_j$  equal to zero and solving for  $c_j$ :

$$\vec{c}^{opt} = (H^T H)^{-1} H^T \vec{s} \quad (19)$$

According to the convention of Equation 16, the resulting reconstruction matrix for the LS estimation technique is given by (26)

$$M_{jn}^{LS} = (H^T H)^{-1} H^T. \quad (20)$$

One of the reasons the LS wavefront estimation approach has been employed for AO systems is that it minimizes the slope measurements by choosing actuator commands in real time without making use of the statistics of the atmospheric turbulence. Knowledge of turbulence statistics and measurement noise statistics is the fundamental difference between the least-squares technique and the minimum variance technique described below.

*2.4.2.2 Minimum Variance Estimation.* The minimum variance (MV) wavefront phase estimation technique minimizes the pupil-averaged mean square residual phase error (26) by optimally choosing the elements of the reconstruction matrix,  $M_{jn}$ . Thus, this method does not assume perfect knowledge of the incident wavefront,  $\psi(\vec{x}_p)$ , but instead it estimates a wavefront based on a noisy set of WFS measurements. Optimization occurs because the MV technique takes into account statistical noise information about the incident wavefront phase and the WFS measurements. The pupil-averaged mean square residual phase error is

used as a performance metric for this thesis and is defined later in this Chapter in Section 2.6.1. It has already been shown that the minimum variance technique outperforms the least-squares technique for AO simulations when Gaussian elementary functions are used (26, 34). This thesis looks at the implementation of the MV technique into the DWFS method.

The minimum variance technique optimally accounts for the case when the WFS measurements have non-zero correlations. It also does the same for correlations between the WFS measurements and the original aberrated wavefront phase. These correlations are neglected in the LS technique (29).

The minimum variance reconstruction matrix has been shown to be

$$M_{jn}^{MV} = R_{jk}^{-1} A_{kn} S_{nm}^{-1}, \quad (21)$$

where  $S_{nm}$  is a  $n \times n$  matrix consisting of slope sensor measurement correlations (26). This is derived from Equation 10 and is given by (26)

$$S_{nm} = -\frac{1}{2} \iint \nabla^q W_n(\vec{x}') \nabla^r W_m(\vec{x}'') D(\vec{x}', \vec{x}'') d^2 \vec{x}' d^2 \vec{x}'' + \langle \sigma_n \sigma_m \rangle. \quad (22)$$

Here,  $D(\vec{x}', \vec{x}'')$  is the structure function of the incident phase and  $\langle \sigma_n \sigma_m \rangle$  is the correlation of the wavefront sensor noise (26).  $R_{jk}$  is a  $j \times j$  matrix with elements

$$R_{jk} = \int W(\vec{x}) e_j(\vec{x}) e_k(\vec{x}) d^2 \vec{x}, \quad (23)$$

where  $e_j(\vec{x})$  and  $e_k(\vec{x})$  are elementary functions. Note that  $R_{jk}$  only requires knowledge of the elementary functions.  $A_{kn}$  is a  $j \times n$  matrix whose elements are given by

$$A_{kn} = - \iint W(\vec{x}_1) \nabla^q W_n(\vec{x}_2) e_k(\vec{x}_1) \langle \psi(\vec{x}_1) \psi(\vec{x}_2) \rangle d^2 \vec{x}_1 d^2 \vec{x}_2. \quad (24)$$

Note that for the tilt-removed cases  $\phi(\vec{x}_p)$  should be substituted for  $\psi(\vec{x}_p)$  in the expression for the  $A_{kn}$  matrix as discussed in Section 3.4.3.



Notice that knowledge of the incident wavefront phase statistics and the WFS noise statistics are required for the computation of matrices  $A_{kn}$  and  $S_{nm}$ . This required statistical knowledge could be considered a drawback to the minimum variance technique as it may be hard to obtain in practice. But, with good statistical knowledge of wavefront phase and WFS noise it was shown to be superior to the LS method for AO systems (26, 29).

*2.4.2.3 Elementary functions.* In addition to looking at the two different wavefront estimation techniques of least-squares and minimum variance, this thesis considers the choice of the elementary function utilized by each method. Recall that the phase estimate,  $\tilde{\psi}(\vec{x}_p)$ , is expressed as a weighted sum of elementary functions as shown in Equation 15.

Systems involving AO have primarily used two-dimensional *Gaussian* elementary functions to determine the actuator control signals in order to move the mirror surface. The Gaussian elementary functions have  $e^{-1}$  widths equal to the distance to the nearest actuator (26). The elementary functions are applied at each actuator location. When Gaussian elementary functions are used, the summation in Equation 15 is conducted over the number of actuators in the AO configuration. Gaussian functions have been used in AO and DWFS simulations (26, 38).

*Zernike polynomials* have also been used as elementary functions. Previously they have been used along with the LS phase estimation technique for AO and DWFS (24, 28). Zernike polynomials have been frequently used to represent aberrations in optical systems. For example, the familiar aberrations of piston, tilt, defocus, astigmatism, and coma each have their own unique Zernike polynomials. A property that makes Zernike polynomials attractive for this study is that they are orthonormal on a circle of unit radius, an appropriate choice for circular telescope apertures. Zernike polynomials are expressed in polar coordinates as a function of a radius,  $r$  and an angle,  $\theta$ . The transformation equations from Cartesian coordinates

$\vec{x} = (x, y)$  to polar coordinates  $(r, \theta)$  are given by

$$\begin{aligned} x &= r \cos \theta, \\ y &= r \sin \theta, \\ r &= \sqrt{x^2 + y^2}, \\ \theta &= \tan^{-1} \frac{y}{x}. \end{aligned} \quad (25)$$

Under the Noll ordering scheme (22), the Zernike polynomials,  $Z_i(r, \theta)$ , are defined as

$$\left. \begin{aligned} Z_{i=even}(r, \theta) &= \sqrt{n+1} R_n^m(r) \sqrt{2} \cos(m\theta) \\ Z_{i=odd}(r, \theta) &= \sqrt{n+1} R_n^m(r) \sqrt{2} \sin(m\theta) \end{aligned} \right\} \quad m \neq 0, \quad (26)$$

and

$$Z_i(r, \theta) = R_n^0(r), \quad m = 0, \quad (27)$$

where the radial functions  $R_n^m(r)$  are defined by (29)

$$R_n^m(r) = \sum_{s=0}^{\frac{(n-m)}{2}} \frac{(-1)^s (n-s)!}{s! \left[ \frac{n+m}{2} - s \right]! \left[ \frac{(n-m)}{2} - s \right]!} r^{n-2s}. \quad (28)$$

The orthonormal property of the Zernike polynomials means that (2)

$$\int W(\vec{x}_p) Z_i(\vec{x}_p) Z_j(\vec{x}_p) d\vec{x}_p = \delta_{ij}, \quad (29)$$

where  $\delta_{ij}$  is the Kronecker delta function given by

$$\delta_{ij} = \begin{cases} 1 & i=j \\ 0 & i \neq j. \end{cases} \quad (30)$$

**2.4.3 Post-Processing Deconvolution Procedure.** Deconvolution is a procedure that is used to effectively remove the imaging system (atmosphere and telescope)

from the image spectrum to get an estimate of the object spectrum,  $\tilde{O}(\vec{f})$ . With the measured image spectrum,  $I(\vec{f})$ , and the corresponding estimated OTF,  $\tilde{H}(\vec{f})$ , a deconvolution procedure can be used to determine the estimated object spectrum,  $\tilde{O}(\vec{f})$ . The estimated object spectrum is a random process due to turbulence effects and measurement noise.

One rather straightforward method for deconvolution can be developed from Equation 4. This is known as an inverse filter. The object spectrum for the inverse filter is given by

$$\tilde{O}(\vec{f}) = \frac{I(\vec{f})}{\tilde{H}(\vec{f})}. \quad (31)$$

The deconvolution approach used in this work was originally presented by Primot (24) who considered the statistical routines involved with estimating the OTF for a variety of aberrated wavefronts. Primot's approach was later modified to remove an unnoticed bias by changing measurement and post-processing procedures. This modified deconvolution procedure is given as

$$\tilde{O}(\vec{f}) = \frac{O(\vec{f}) \langle H_i(\vec{f}) \tilde{H}_i^*(\vec{f}) \rangle}{\langle H_k^{ref}(\vec{f}) [\tilde{H}_k^{ref}(\vec{f})]^* \rangle}, \quad (32)$$

where the asterisk,  $*$ , represents the complex conjugate,  $\tilde{H}_i(\vec{f})$  is the OTF estimate for the  $i$ th phase screen realization,  $O(\vec{f})$  is the object spectrum,  $H_k^{ref}(\vec{f})$  is the normalized Fourier transform of the  $k$ th reference star image, and  $\tilde{H}_k^{ref}(\vec{f})$  is computed from the  $k$ th WFS measurement of the light from the reference star (31, 29). The estimate of the object intensity distribution,  $\tilde{o}(x, y)$ , is obtained by taking the inverse Fourier transform of Equation 32.

## 2.5 Simulating DWFS

The process of simulating DWFS is depicted in Figure 6 and is fully described in Reference (29). A DWFS simulation begins by reading in the problem parameters.

A typical set of input parameters is shown in Table 12 in Appendix A. With this information the telescope pupil model is established, the object is created and scaled for the viewing geometry, and the object spectrum,  $O(\vec{f})$  is calculated. Next, the first of  $I$  specified phase screens is generated using the input parameters. A large number of iterations is used to establish statistical significance for the quantities of interest. This provides good estimates of the mean and variance of these quantities. Each generated phase screen is used as input to the wavefront sensor model. The WFS model generates noise-free slope measurements and then corrupts them by adding shot noise and detector read noise as described in Section 2.4.1.1. Next, one of several techniques can be used to obtain an estimate of the wavefront phase,  $\tilde{\psi}(\vec{x}_p)$ , as described in Section 2.4.2. The generalized pupil function is calculated and used to determine the estimated OTF,  $\tilde{H}(\vec{f})$ , for each phase screen as described in Section 2.6.2. What happens next depends on whether a point source object or an extended object is being imaged. For point source objects or those simulations requiring only information about the DWFS system transfer function, the quantity  $H(\vec{f})\tilde{H}^*(\vec{f})$  is calculated for each phase screen and statistical quantities used to determine the mean and variance of this term are stored. This is shown in Figure 6 by the dashed line leaving the “compute OTF” box. If an extended object is to be imaged, the photon-limited image,  $d(\vec{x})$ , and image spectrum,  $D(\vec{f})$ , are calculated. This is shown in Figure 6 by the solid line leaving the “compute OTF” box. Next, the quantity  $D(\vec{f})\tilde{H}^*(\vec{f})$  is computed for each phase screen and statistical quantities are accumulated. Deconvolution and the inverse FFT are then applied to produce the object spectrum estimate,  $\tilde{O}(\vec{f})$ , and estimated object intensity distribution,  $\tilde{o}(\vec{x})$ , respectively.

## 2.6 Performance Metrics

A number of performance metrics was used to test the effectiveness of the different wavefront estimation techniques. These metrics include the average pupil-

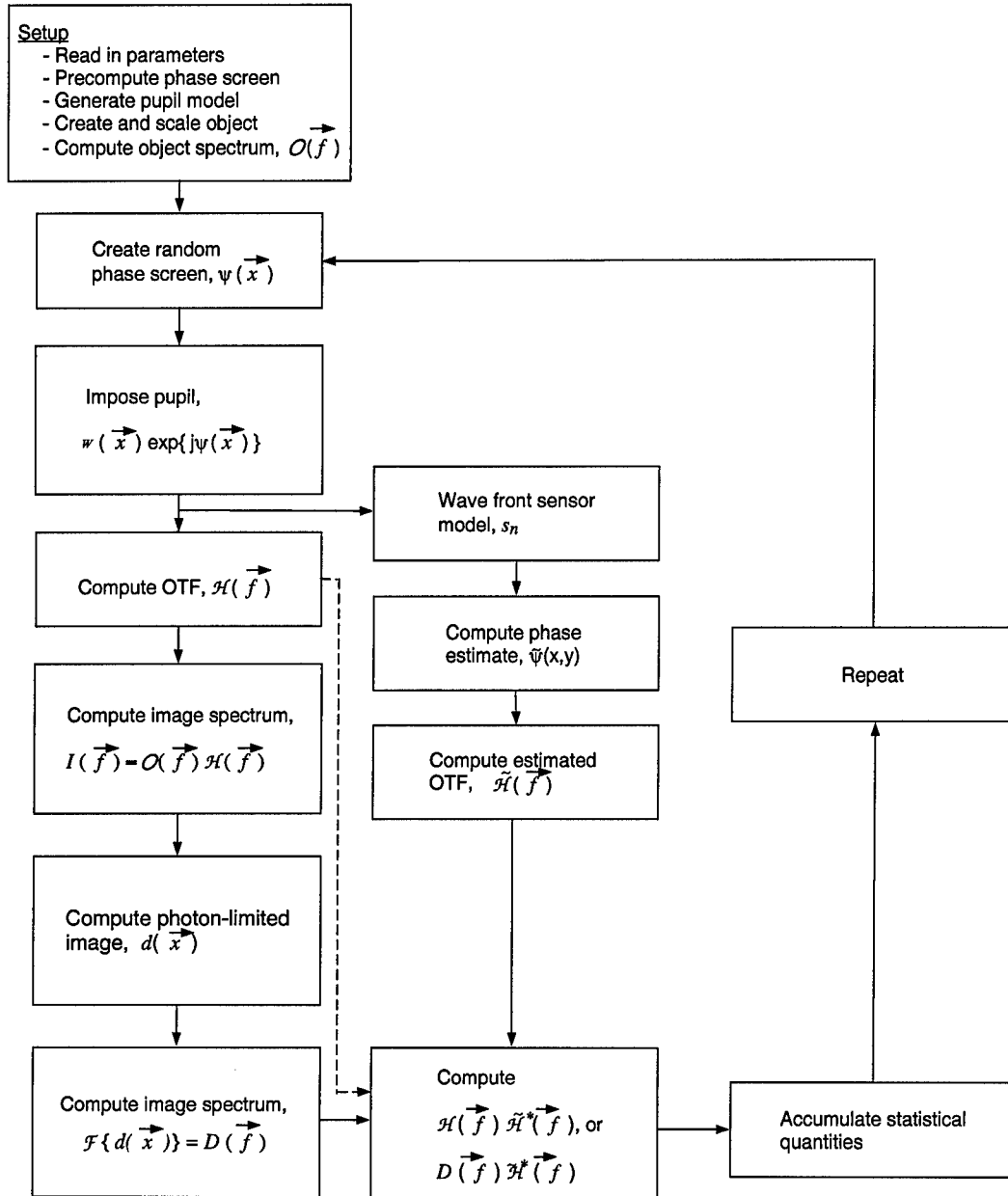


Figure 6. Simulating Deconvolution from Wavefront Sensing (DWFS) (29).

averaged mean square residual phase error ( $\langle \varepsilon^2 \rangle$ ), the average system transfer function ( $\langle H(\vec{f})\tilde{H}^*(\vec{f}) \rangle$ ), the signal-to-noise ratio of the average system transfer function ( $SNR_{\langle H(\vec{f})\tilde{H}^*(\vec{f}) \rangle}(\vec{f})$ ), and the OTF correlation ( $\gamma_{H\tilde{H}}(\vec{f})$ ). For the extended object simulations, three additional metrics were employed. First, a correlation algorithm was used to determine how well the estimated object intensity distribution,  $\tilde{o}(\vec{x})$ , correlated with the original object intensity distribution,  $o(\vec{x})$ . Second, the signal-to-noise ratio of the object spectrum estimate,  $SNR_{\tilde{o}(\vec{f})}(\vec{f})$  was calculated. And third, an estimate of the on-object resolution is made. These performance metrics are described in more detail below.

*2.6.1 Average Pupil-Averaged Mean Square Residual Phase Error.* The pupil-averaged mean square residual phase error,  $\varepsilon_i^2$ , is a measure of the average deviation of the phase estimate from the original phase and can be used as a performance measure of each wavefront estimation technique. Assuming no time delay, the residual phase for a single phase screen realization in the pupil plane is given by (29, 36)

$$\varepsilon_i(\vec{x}_p) = \tilde{\psi}_i(\vec{x}_p) - \psi_i(\vec{x}_p). \quad (33)$$

Averaging the value of  $\varepsilon_i^2(\vec{x}_p)$  over the pupil yields the pupil averaged mean square residual phase error,

$$\varepsilon_i^2 = \int W(\vec{x}_p) \langle \varepsilon_i^2(\vec{x}_p) \rangle d\vec{x}_p. \quad (34)$$

For the simulations used in this thesis, an *average* pupil-averaged mean square residual phase error was determined by averaging over the number of realizations  $I$ :

$$\langle \varepsilon^2 \rangle = \frac{1}{I} \sum_{i=1}^I \varepsilon_i^2 \quad (35)$$

Note that the expression in Equation 35 was also used to determine the optimal number of Zernike polynomials as discussed in Sections 3.5 and 4.2. The units for  $\langle \varepsilon^2 \rangle$  are radians<sup>2</sup>.

*2.6.2 Average System Transfer Function.* The average system transfer function is the expected value of the product of the OTF and the conjugate of the estimated OTF ( $\langle H(\vec{f}) \tilde{H}^*(\vec{f}) \rangle$ ). The OTF of an LSI system is the autocorrelation of the Generalized Pupil function (GPF) (11). The GPF is the product of the pupil function and a function describing the aberration and is defined as (29)

$$GPF(\vec{x}_p) = W(\vec{x}_p) e^{j\psi_i(\vec{x}_p)}. \quad (36)$$

Here,  $\psi_i(\vec{x}_p)$  is the  $i$ th wavefront phase screen. The OTF is then (11)

$$H(\vec{f}) = \frac{GPF(\vec{f}\lambda d_i) \star GPF(\vec{f}\lambda d_i)}{GPF(0) \star GPF(0)}, \quad (37)$$

where  $\star$  is the correlation operator (11),  $d_i$  is the distance between the exit pupil and the image plane, and  $\lambda$  is the imaging wavelength.

When an object is viewed through atmospheric turbulence the effect is the same as introducing an aberration into the telescope pupil. This makes the optical transfer function a random quantity varying in space and time and requires one to speak in terms of the instantaneous OTF,  $H_i(\vec{f})$ . The OTF for the  $i$ th phase screen realization is

$$H_i(\vec{f}) = N^{-1} \int W(\vec{x}_p) W(\vec{x}_p - \vec{f}\lambda d_i) \exp\{j[\psi_i(\vec{x}_p) - \psi_i(\vec{x}_p - \vec{f}\lambda d_i)]\} d\vec{x}_p, \quad (38)$$

where  $d_i$  is the distance between the exit pupil and the image plane,  $\lambda$  is the imaging wavelength, and the normalizing factor,  $N$ , is given by

$$N = \int |W(\vec{x}_p)|^2 d\vec{x}_p. \quad (39)$$

For DWFS, an estimate of this OTF is required. This is determined by replacing the original phase,  $\psi_i(\vec{x}_p)$ , with the estimated phase,  $\tilde{\psi}_i(\vec{x}_p)$  in Equation 38.

Recall that DWFS uses this average OTF estimate in a deconvolution procedure to get the estimate of the object spectrum,  $\tilde{O}(\vec{f})$ .

It should be noted that many quantities in this thesis such as the signal-to-noise ratio, or the system transfer function, are two-dimensional functions of spatial frequency  $(f_x, f_y)$  and are expressed as two-dimensional arrays. For easier display and interpretation, one-dimensional radial averages of these two-dimensional arrays are used. This averaging is accomplished by first binning the elements of the two-dimensional matrix that lie in equivalent radial distances from the center element and then averaging the elements in each bin. Each element of the resulting one-dimensional array represents the average value of the two-dimensional array elements that fall in each radial distance bin. It should also be noted that in this thesis, plots of quantities that are functions of spatial frequency are displayed as functions of *normalized spatial frequency*. Normalized spatial frequency is the spatial frequency divided by the cutoff frequency of the imaging system. The cutoff frequency is the system aperture diameter divided by the product of the imaging wavelength and the focal length.

*2.6.3 Signal-to-Noise Ratio.* This section presents expressions for the signal-to-noise ratio of a number of random quantities including the system transfer function, the image spectrum, and the estimated object spectrum. A general expression for the SNR of a random quantity was presented in Section 2.3.3. The SNR has previously been used as a measure of the information content of an image (26). High spatial frequencies are important to image quality because they contain the detail of the image. This follows from the scaling property of the Fourier transform which states that small changes in the spatial domain result in large changes in the spatial frequency domain (8). The expressions that follow are for a doubly stochastic Poisson random process that have randomness arising from shot noise and image additive noise due to a random OTF. In general, random fluctuations in the OTF tend to lower the SNR of the image spectrum (29).



**2.6.3.1 System Transfer Function SNR.** For point source simulations, the signal-to-noise ratio of the average system transfer function was used as a performance metric. For DWFS, the SNR of the average system transfer function is given by

$$SNR_{\langle H(\vec{f})\tilde{H}^*(\vec{f}) \rangle}(\vec{f}) = \frac{\bar{K}_I |O_n(\vec{f})| |\langle H(\vec{f})\tilde{H}^*(\vec{f}) \rangle|}{\sqrt{\bar{K}_I \langle |\tilde{H}(\vec{f})|^2 \rangle + \bar{K}_I^2 |O_n(\vec{f})|^2 var\{H(\vec{f})\tilde{H}^*(\vec{f})\}}}, \quad (40)$$

where  $O_n(\vec{f})$  is the normalized object spectrum and  $\bar{K}_I$  is the average number of photoevents per frame for the telescope pupil.

**2.6.3.2 Image Spectrum SNR.** For extended object simulations the additional metric of SNR of the image spectrum was used. The SNR for the image spectrum,  $I(\vec{f})$ , is (30)

$$SNR_{I(\vec{f})}(\vec{f}) = \frac{\bar{K}_I |\langle H(\vec{f}) \rangle| |O_n(\vec{f})|}{\sqrt{\bar{K}_I + \bar{K}_I^2 |O_n(\vec{f})|^2 var\{H(\vec{f})\}}}. \quad (41)$$

Notice that as the number of photons increases, the SNR of the image spectrum approaches the SNR of the OTF. This means that high light levels cannot overcome the randomness in the OTF caused by atmospheric turbulence (29).

**2.6.3.3 Object Estimate SNR.** The signal-to-noise ratio of the DWFS object spectrum estimate is given by (29)

$$SNR_{\tilde{O}(\vec{f})}(\vec{f}) = \frac{|\langle \tilde{O}(\vec{f}) \rangle|}{\sqrt{var\{\tilde{O}(\vec{f})\}}}, \quad (42)$$

where  $\tilde{O}(\vec{f})$  is given by Equation 32.

**2.6.4 OTF Correlation.** The OTF correlation,  $\gamma_{H\tilde{H}}(\vec{f})$ , has been previously identified as a measure of how well the estimated OTF correlates with the theoretical

OTF (18, 37). For a given spatial frequency,  $\gamma_{H\tilde{H}}(\vec{f})$  takes on values from zero to one. Values of  $\gamma_{H\tilde{H}}(\vec{f})$  close to unity over all spatial frequencies indicate that  $\tilde{H}(\vec{f})$  is a very good estimate of the theoretical OTF,  $H(\vec{f})$ . The OTF correlation will be affected by noise levels and turbulence conditions and will have the best values for the highest light levels and lowest turbulence conditions (37). The OTF correlation is expressed as

$$\gamma_{H\tilde{H}}(\vec{f}) = \frac{\langle H(\vec{f})\tilde{H}^*(\vec{f}) \rangle}{\sqrt{\langle |H(\vec{f})|^2 \rangle \langle |\tilde{H}(\vec{f})|^2 \rangle}}. \quad (43)$$

**2.6.5 Image Quality Assessment.** The performance parameters defined above quantify general imaging system performance. But what does this mean in terms of the quality of the image itself? For images of extended objects, an assessment of image quality can be made. Image quality and resolution are closely related with higher resolution images being associated with higher image quality. In addition to the SNR of the image spectrum and object spectrum estimate, the correlation coefficient and on-object resolution can be used to assess image quality. These are described below.

**2.6.5.1 Correlation Coefficient.** Seyrafi points out that the usefulness of images are related to image resolution (32). Pratt discusses how subjective ratings can be used along with various quantitative methods to quantify image quality (23). One method to quantify the quality of an aberrated image is to use a correlation coefficient (39). The correlation coefficient is a pixel-by-pixel measure of how well one image correlates with another. For the problem at hand this can be applied by determining the correlation coefficient between the estimate of the object intensity distribution  $\tilde{o}(x, y)$  and the original object intensity distribution  $o(x, y)$ . For  $256 \times 256$  images, the correlation coefficient (33) is described by

$$C = \frac{\sum_{x=1}^{256} \sum_{y=1}^{256} o(x, y)\tilde{o}(x, y)}{\left[ \sum_{x=1}^{256} \sum_{y=1}^{256} o^2(x, y)\tilde{o}^2(x, y) \right]^{1/2}}. \quad (44)$$

The correlation coefficient takes on values from 0 to 1, with the best correlations occurring at values closest to one. Note that the correlation coefficient of image with itself is one.

*2.6.5.2 Assessment of DWFS Resolution Improvement.* One method to assess the usefulness of the DWFS technique is to quantify the improvement it brings to on-object resolution. Resolution in this context is the distance between the two closest points on the object that can be distinguished. An upper bound for resolution is the diffraction-limited angular resolution which is given as (25)

$$\theta_{DL} \approx \frac{1.22\lambda}{D}, \quad (45)$$

where  $\lambda$  is the imaging wavelength and  $D$  is the telescope aperture diameter. This corresponds to a diffraction-limited cutoff frequency of

$$f_{DL} \approx \frac{D}{1.22\lambda}. \quad (46)$$

The random effects of atmospheric turbulence and shot noise act to reduce the diffraction-limited cutoff frequency to a lower value. For this lower value, the effective cutoff frequency,  $f_{eff}$ , can be defined as the normalized spatial frequency where the signal-to-noise ratio falls below a value of two. The unnormalized effective cutoff frequency is then  $f_{eff}(D/\lambda)$ . This results in a larger (worse) angular resolution. The effective angular resolution becomes

$$\theta_{eff} \approx \frac{1.22\lambda}{f_{eff}D}, \quad (47)$$

and the spatial resolution is then

$$\Delta x \approx R(\theta_{eff}), \quad (48)$$

where  $R$  is the range to the object. Equation 48 will be used in Section 4.4.2.3 to calculate the spatial resolution for the image intensity distribution,  $i(\vec{x})$  and the object estimate intensity distribution,  $\tilde{o}(\vec{x})$ . This will quantify the resolution improvements possible from application of the DWFS method.

## 2.7 Summary

This chapter has presented a variety of theoretical concepts that are necessary for the research conducted in this thesis. The key points in this chapter include the presentation of the linear shift invariant model for imaging systems and a discussion of the theory behind atmospheric turbulence. The theory involved with the DWFS method was also presented which included a discussion on the Hartmann wavefront sensor, reference beacon, and the deconvolution procedure used to determine the object estimate. The least-squares and minimum variance wavefront phase estimation techniques were also presented along with a discussion of Gaussian and Zernike polynomial elementary functions. Finally, the theory involved with each of the performance metrics used in this thesis was presented.

### III. Methodology

#### 3.1 Introduction

This chapter presents the methodology that was used in carrying out the research. First, a justification for conducting imaging simulations is presented. This is followed by a discussion of the simulations used. Next, the assumptions and key parameters used in the simulations are discussed. Finally, the parameters for the point source and extended object simulations are presented.

#### 3.2 Simulations

Imaging simulations were used to assess the performance of the different wave-front estimation techniques. Simulations were conducted for several reasons. First, the DWFS method has not been widely tested in ground-based telescopes and consequently experimental data are not readily available. Second, simulations are a way to avoid complex analytical expressions that must be solved to evaluate the performance of the imaging system (29). Third, analytical calculations cannot produce an image (26). And, fourth, simulations offer a convenient way to manipulate parameters. The simulation codes used have been tested against theoretical performance (26) and used in previous studies (15, 30, 37).

For these simulations, both a point source object and an extended object were imaged. Point source simulations were used to determine the general imaging performance. By definition, a *point source* is any object which subtends an angle less than the angle subtended by the first zero of the diffraction pattern (Airy disk) of the optical system. The object in question can be considered a point source when the following relationship is satisfied (27).

$$\frac{L_s}{R} < \frac{2.44\lambda}{D}. \quad (49)$$

Here,  $L_s$  is the diameter of the object in question,  $R$  is the range to the object from the imaging system,  $\lambda$  is the imaging wavelength, and  $D$  is the diameter of the imaging system aperture.

For this study, the object used for a point source is a delta function which has a Fourier transform equal to unity. A star can be considered a point source object and is used in practice as reference beacon for the WFS. For the point source simulations, established performance metrics were used to determine the best performing wavefront estimation technique.

Extended object simulations were also conducted in order to demonstrate the DWFS method, and to quantify image differences between the LS-Z and MV-Z wavefront estimation techniques. For these simulations, a computer graphics rendering of a satellite was used as the extended object. The extended object intensity distribution,  $o(x, y)$ , is shown in Figure 7. This satellite has a maximum dimension of 10 meters. Note that for the remainder of this thesis, negative images will be shown for clarity.

### 3.3 Imaging System

The imaging system used in the simulations was a ground-based telescope with a one-meter aperture diameter, no obscuration and an image field of view of  $24.1\mu\text{rad}$ <sup>1</sup>. The pupil area was sampled with 60 subapertures and uses a Hartmann wavefront sensor with an ideal quad-cell detector. This telescope geometry is shown in Figure 8. An imaging wavelength of  $0.6\mu\text{m}$  with a bandwidth of  $0.06\mu\text{m}$  was used. The wavefront sensor had a wavelength of  $0.5\mu\text{m}$  and a bandwidth of  $0.1\mu\text{m}$ . An overall transmission coefficient of 0.5 was assumed. This value is the product of several individual transmission coefficients including the detector quantum efficiency, the transmission of the telescope optics, and the atmospheric transmission.

---

<sup>1</sup>Note that this is the field of view for the images presented and is not necessarily the field of view of the telescope.

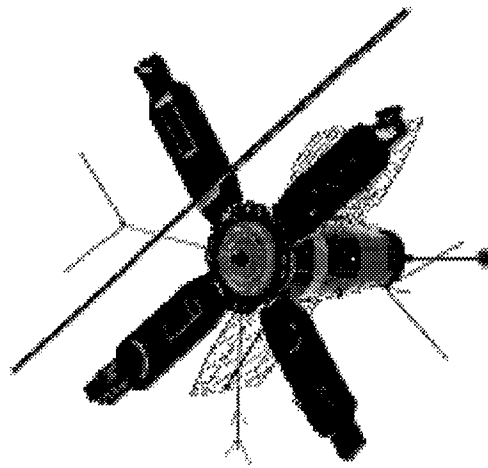


Figure 7. Generic Satellite Used for Extended Object Simulations.

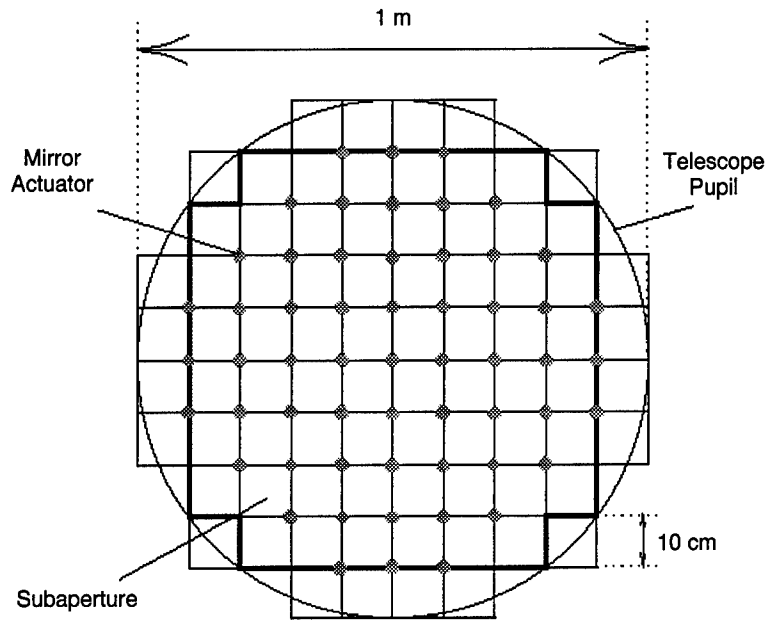


Figure 8. Telescope Pupil Geometry.

An integration time of 10 milliseconds was used which sets the photon flux parameter. Values used for the range from the telescope to the object were 500 km and 35780 km. These represent typical altitudes for satellites in low earth orbit (LEO) and geosynchronous orbit (GEO), respectively. These characteristics of the imaging system are summarized in Table 1.

### 3.4 Simulation Parameters

Four parameters were varied in order to investigate the effectiveness of the different wavefront estimation techniques over different telescope operational conditions. These parameters were light levels, atmospheric coherence diameter, pre-processing tilt removal, and the choice of wavefront estimation technique. Recall that a detailed discussion of the wavefront estimation techniques was made in Section 2.4.2. Variations in these parameters allowed the performance of the different wavefront estimation techniques in DWFS to be evaluated over realistic telescope operating conditions. Also, the optimal value for the number of Zernike polynomials was determined and used for the two wavefront estimation techniques that employed



| Parameter           | Value            |
|---------------------|------------------|
| Aperture diameter   | 1.0 m            |
| Subaperture length  | 10 cm            |
| Image field of view | 24.1 $\mu$ rad   |
| Range to target     | 500 km, 35780 km |
| Imaging wavelength  | 0.6 $\mu$ m      |
| Imaging bandwidth   | 0.06 $\mu$ m     |
| WFS wavelength      | 0.5 $\mu$ m      |
| WFS bandwidth       | 0.1 $\mu$ m      |
| Total efficiency    | 0.5              |
| Integration time    | 0.01 sec         |

Table 1. Imaging System Used for Simulations.

Zernike polynomial elementary functions. Each of the four parameters is described below.

*3.4.1 Light Levels.* Light level calculations were conducted to associate a particular visual magnitude with a photon flux. Visual magnitude is a luminous flux density measurement. It is a measure of the brightness of an object and is frequently used by the astronomy community. Photon flux is a direct measure of the number of photoevents per unit area per unit time. Here, it is described as the average number of photons arriving at the telescope pupil or at each subaperture per frame. The per frame integration time used was 0.01 sec.

Ignoring atmospheric absorption, the spectral irradiance of an object on the ground can be expressed as

$$E_{obj} = E_{sun}(1.944 \times 10^{-11})10^{-0.4m_v}, \quad (50)$$

where  $E_{sun}$  is the spectral irradiance of the sun on the ground ignoring atmospheric absorption, and  $m_v$  is the visual magnitude of the object (27). The values for  $E_{sun}$  were obtained from a space environment handbook (14). The average number of

| Parameter       | $\lambda_I=0.6\mu\text{m}$                       | $\lambda_{WFS}=0.5\mu\text{m}$                   |
|-----------------|--|--|
| $E_{obj}$       | $1750 \frac{\text{watt}}{\text{m}^2\mu\text{m}}$ | $1950 \frac{\text{watt}}{\text{m}^2\mu\text{m}}$ |
| $A$             | $0.785 \text{ m}^2$                              | $0.01 \text{ m}^2$                               |
| $\tau$          | 0.5  | 0.5  |
| $\Delta t$      | 0.01 sec   | 0.01 sec   |
| $\Delta\lambda$ | $0.06\mu\text{m}$                                | $0.1\mu\text{m}$                                 |

Table 2. Values Used for Light Level Calculations.

| $m_v$ | $\bar{K}_{WFS}$ | $\bar{K}_I$ | $SNR_{WFS}$ |
|-------|-----------------|-------------|-------------|
| 0     | 476,758         | 24,194,910  | 690.48      |
| 4     | 11,976          | 607,749     | 109.43      |
| 5.37  | 3,391           | 172,077     | 58.23       |
| 8     | 301             | 15,266      | 17.34       |
| 12    | 9               | 457         | 3           |
| 14    | 1.198           | 60.77       | 1.09        |

Table 3. Average Photoevents Per Frame for the Wavefront Sensor ( $\bar{K}_{WFS}$ ) and the Image Plane ( $\bar{K}_I$ ) for Different Visual Magnitudes.

photoevents per frame is given by

$$\bar{K} = \frac{E_{obj} A \tau \Delta\lambda \Delta t}{\frac{hc}{\lambda}}. \quad (51)$$

Here,  $A$  is the area (either aperture area or subaperture area),  $\Delta\lambda$  is the bandwidth,  $\tau$  is the overall transmission coefficient,  $\Delta t$  is the integration time,  $h$  is Planck's constant,  $\lambda$  is the imaging wavelength and  $c$  is the speed of light in a vacuum. The values used for Equations 50 and 51 are listed in Table 2.

The number of photoevents per frame must be determined for each subaperture and the entire telescope pupil because the telescope and WFS operate at different wavelengths with different bandwidths. Equations 50 and 51 were used to generate the average photon flux levels that were used in the simulations. These values are listed in Table 3.

The Air Force Maui Optical Station (AMOS) has accumulated statistics of the visual magnitudes of the objects it images. The data were taken with the 1.6 meter

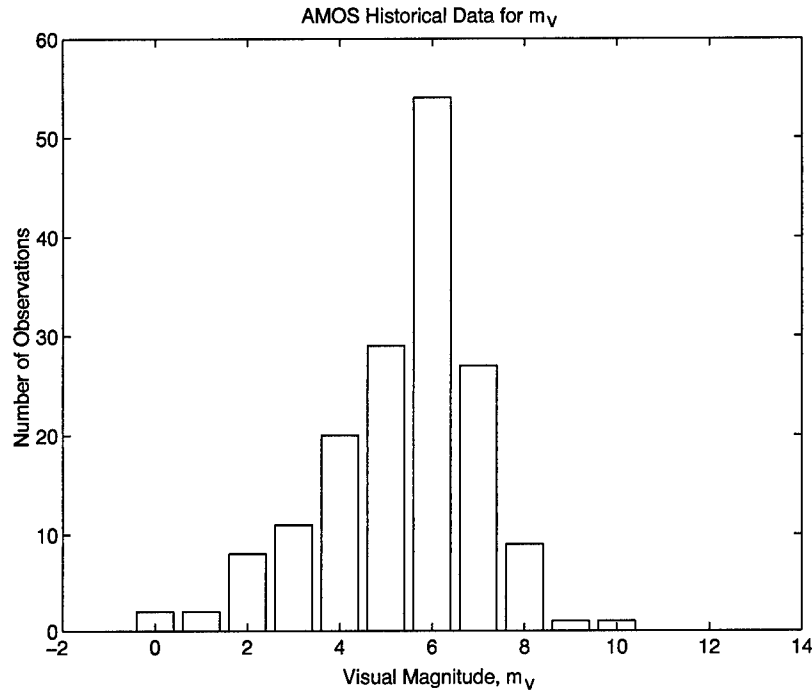


Figure 9. AMOS  $m_v$  Historical Data.

telescope located at Mt. Haleakala, Maui, Hawaii for the period of 1984 through 1991 (1). This telescope was primarily tasked to conduct imaging of satellites in LEO. The distribution is shown in Figure 9. These data give an indication of the light levels actually experienced during USAF telescope operations and present a justification for the light level values used in this study. The mean value for visual magnitude is 5.37. Note that the extreme values used in this study ( $m_v = 0$  and  $m_v = 14$ ) are rarely encountered.

*3.4.2 Atmospheric Coherence Diameter.* The atmospheric coherence diameter or Fried parameter,  $r_0$ , is a measure of the intensity of atmospheric turbulence. It is dependent on wavelength and is a first order measure of the effects of the atmosphere on imaging systems. It is given in terms of a size and has been defined as the effective aperture diameter that a telescope operating without atmospheric turbulence would require to match the same telescope operating through the atmosphere

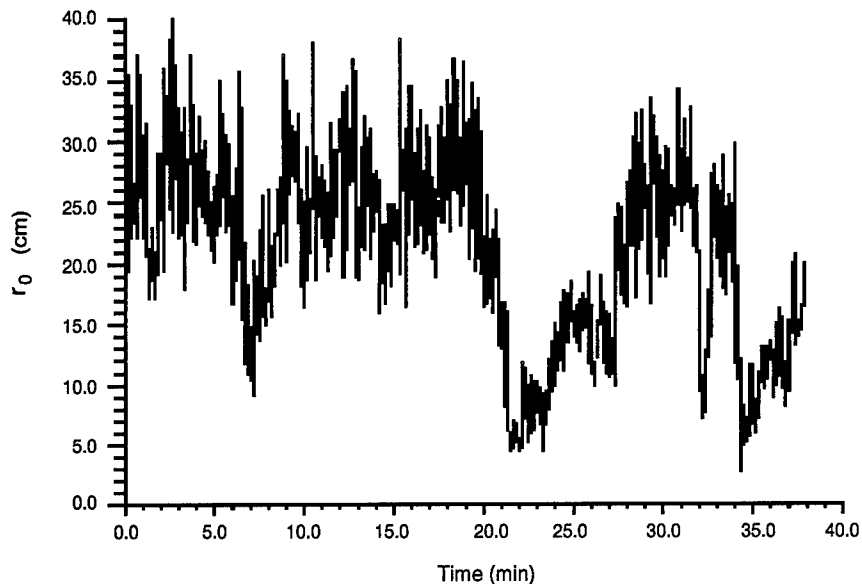


Figure 10. Variation in  $r_0$ .

in terms of resolution. The atmospheric coherence diameter can also be considered the effective aperture size of a telescope past which further increases in aperture size would not improve resolution (29). Larger values of  $r_0$  indicate a less turbulent atmosphere. Figure 10 shows how  $r_0$  can vary considerably over a single observing session (21). These data were taken at an observatory at Copella, United Kingdom, on 26 December 1993. For visible wavelengths, a good imaging system could expect  $r_0$  variations between 10 and 30 cm (21).

Figure 11 shows the historical data for  $r_0$  values at AMOS. The mean value is 9.79 cm (1). An  $r_0$  value of 50 cm can be considered an effective upper bound. It represents conditions where atmospheric turbulence effects are negligible and approaches the diffraction-limited performance.

*3.4.3 Pre-Processing Tilt Correction.* Tilt correction was another parameter that was varied in the simulations. *Tilt* is a fundamental aberration that is common to imaging systems operating with atmospheric turbulence and can be

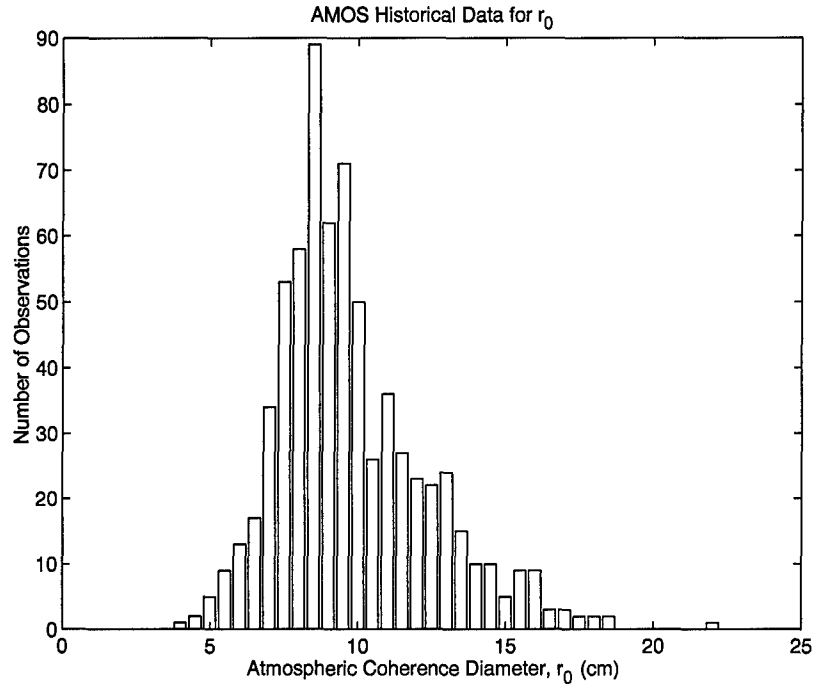


Figure 11. AMOS  $r_0$  Historical Data.

thought of as the overall angle of the incoming aberrated wavefront<sup>2</sup>. Early adaptive optics systems consisted of a flat mirror which could be tilted in two orthogonal directions (29). Initially removing tilt is an effective practice since it lowers the magnitude of the corrections that need to be made and since eighty-seven percent of the power in wavefront phase aberrations is due to random tilt (29). One half of the point source simulations in this thesis were conducted with tilt initially removed before an estimate of the wavefront was made. The other half of the simulations were conducted where tilt was not initially removed. The tilt-removed phase,  $\phi(\vec{x}_p)$ , is given in Reference (26) as

$$\phi(\vec{x}_p) = \psi(\vec{x}_p) - \left[ (16/D) \int \vec{x}_p W(\vec{x}_p) d^2 \vec{x}_p \right] \cdot \vec{x}_p, \quad (52)$$

<sup>2</sup>In contrast, *piston*, is an up and down aberration and single aperture imaging systems are unaffected by the piston component of the phase. Piston was removed for the simulations in this thesis.

where the term in brackets is the tilt component of the wave and  $D$  is the diameter of the telescope aperture.  $W(\vec{x}_p)$  is the pupil function, which is defined such that

$$\int W(\vec{x}_p) d^2 \vec{x}_p = 1 \quad (53)$$

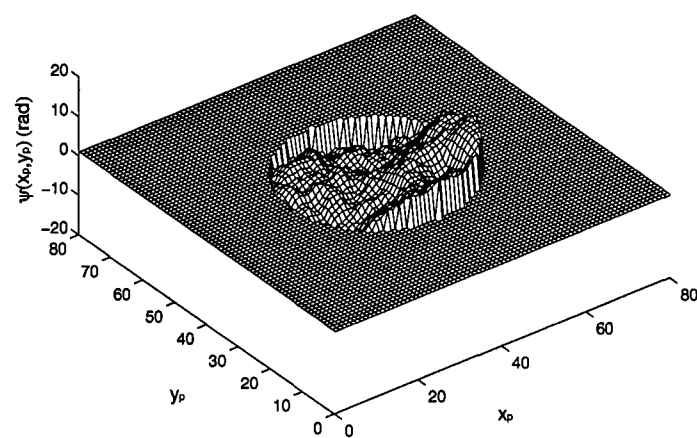
inside the pupil and  $W(\vec{x}_p) = 0$  outside the pupil.

Figure 12 shows examples of an aberrated wavefront within the telescope pupil where tilt is not removed (frame a) and where tilt is removed (frame b). This figure demonstrates how phase estimation (or reconstruction for AO) would be easier for the tilt-removed case since the dynamic range is reduced. Intuitively, one would expect the wavefront estimation technique to do a better job estimating the tilt-removed phase.

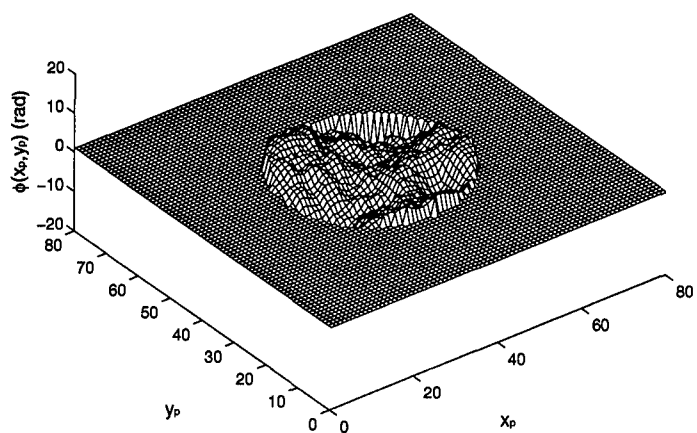
*3.4.4 Wavefront Estimation Technique.* The key parameter to be varied in this thesis is the choice of wavefront estimation technique. As was previously mentioned, four techniques were studied. A least-squares and a minimum variance approach were the two general optimization techniques used and each of these used both Gaussian and Zernike polynomial elementary functions. Recall that the four techniques will be abbreviated in the following manner: Least-squares with Gaussian elementary functions (LS-G), least-squares with Zernike polynomial elementary functions (LS-Z), minimum variance with Gaussian elementary functions (MV-G), and minimum variance with Zernike polynomial elementary functions (MV-Z). Recall that the major contributions of this thesis are the use of Zernike polynomial elementary functions with the minimum variance technique and the use of the minimum variance techniques in the DWFS method.

### *3.5 Number of Zernike Polynomials*

For those wavefront estimation techniques that use Zernike polynomial elementary functions, a decision had to be made as to the number of polynomials to use.



(a)



(b)

Figure 12. Wavefront With and Without Tilt Aberration Removed: (a) Wavefront,  $\psi(\vec{x}_p)$ , (b) Tilt-Removed Wavefront,  $\phi(\vec{x}_p)$ .

Roggemann and Welsh (29) note that for the case of the LS-Z technique there are bounds on the number of elementary functions which can be used to build the phase estimate,  $\tilde{\psi}(\vec{x}_p)$ . One bound is that there be more measurements than unknowns. This means that  $2N \geq J$ , where  $N$  is the number of subapertures and  $J$  is the number of Zernike polynomials. For the telescope model used in this thesis, this means that the number of Zernike polynomials must be less than or equal to twice the number of subapertures, or  $J \leq 120$ . A second bound occurs because the quantity  $(H^T H)^{-1}$  of Equation 20 does not exist when too many Zernike polynomials are used. The error manifests itself as large residual errors along the edges of the pupil. For the case of the minimum variance technique, the  $R_{jk}$  and  $S_{nm}$  matrices defined in Section 2.4.2.2 are always invertible so there are no instabilities past some threshold number of Zernike polynomials.

Previous work assumed a single value of  $J$  for the LS-Z wavefront estimation technique (15, 31, 28). For the present study, the choice for the number of Zernike polynomials for both the LS-Z and the newly implemented MV-Z estimator was optimized. This value was optimized for each of the 64 point source simulations, and each of the 16 extended object simulations that are described in Sections 3.6.1 and 3.6.2.  $J$  was optimized by minimizing the value of the average pupil-averaged mean square residual phase error,  $\langle \varepsilon^2 \rangle$ , which was defined in Section 2.6.1.

### 3.6 Simulation Matrices

*3.6.1 Point Source Simulations.* Simulations where the object was a point source were used to determine the general imaging performance. Table 4 shows the simulation matrix that was used for the point source runs. This simulation matrix shows the 128 simulations that were used for the different combinations of light levels,  $r_0$  values, tilt removal cases, and wavefront estimation techniques. It should also be noted that additional simulations needed to be run for each of the cases involving Zernike polynomials to determine the optimal number of Zernike Polynomials.



| Parameter                             | Values                    |
|---------------------------------------|---------------------------|
| Atmospheric coherence diameter, $r_0$ | 7 cm, 10 cm, 15 cm, 50 cm |
| Visual magnitude, $m_v$               | 0, 4, 8, 12               |
| Tilt removal                          | Yes, No                   |
| Wavefront estimation technique        | LS-G, LS-Z, MV-G, MV-Z    |

Table 4. Point Source Simulation Input Parameters.

| Parameter                             | Values               |
|---------------------------------------|----------------------|
| Atmospheric coherence diameter, $r_0$ | 9.79 cm              |
| Visual magnitude, $m_v$               | 5.37 (LEO), 14 (GEO) |
| Tilt removal                          | Yes                  |
| Range to target                       | 500 km, 35780 km     |
| Wavefront estimation technique        | MV-Z                 |

Table 5. DWFS Demonstration Simulation Input Parameters.

*3.6.2 Extended Object Simulations.* There were two objectives for running simulations using extended objects. The first was to demonstrate the capabilities of the DWFS technique to improve the resolution of images. The use of an extended object serves to package the performance metrics that were demonstrated using a point source object into a more tangible product, and to quantify the resolution improvements that can be obtained using DWFS. For these demonstration runs, the image intensity distribution  $i(x, y)$  is compared with the estimate of the object intensity distribution,  $\tilde{o}(x, y)$ . This demonstrates results before and after the application of DWFS. The parameters used for the DWFS demonstration simulations are shown in Table 5. For these simulations the MV-Z estimation technique was used with the optimal number of Zernike polynomials, tilt was initially removed, and two ranges corresponding to satellites at low earth orbit and geosynchronous orbit altitudes were used. Also, typical values for atmospheric coherence diameter and light levels for each altitude were used. Note that typical visual magnitudes for geosynchronous satellites are 14-15 (27).

A second objective for the extended object simulations was to quantify the comparative performance of the LS-Z and the MV-Z estimation techniques. This

| Parameter                             | Values      |
|---------------------------------------|-------------|
| Atmospheric coherence diameter, $r_0$ | 10 cm       |
| Visual magnitude, $m_v$               | 0, 4, 8, 12 |
| Tilt removal                          | Yes         |
| Range to target                       | 500 km      |
| Wavefront estimation technique        | LS-Z, MV-Z  |

Table 6. Extended Object Simulation Input Parameters.

allows for a direct comparison of the new technique implemented in this thesis and the previous least-squares technique that used Zernike polynomial elementary functions. This was done for a point source object by assessing general imaging system performance. Here, operational imaging system performance is evaluated using an assessment of the quality of the corrected image from each technique. Image spectrum SNR, object estimate spectrum SNR, the correlation coefficient and on-object resolution were used to quantify the corrected image quality. The parameters used for the extended object runs are shown in Table 6. These simulations all removed the tilt aberration prior to processing. A typical value for  $r_0$  was used along with four light levels. The object was at a range of 500 km and, as before, the optimal number of Zernike polynomials was used.

### 3.7 Summary

This chapter presented the methodology that was used to produce the results presented in the next chapter (Chapter IV). A justification for conducting imaging simulations was presented, followed by a description of the imaging system and a discussion of the simulations themselves, their assumptions and key parameters. Next, the methodology used to optimize the number of Zernike polynomials was described. Finally, the specific simulation parameters for the point source and extended object simulations were presented.

## IV. Results and Analysis

### 4.1 Introduction

Previous chapters have introduced the problem, described the requisite theory and discussed the methodology employed. This chapter presents and analyzes the results. The results are presented for the series of point source and extended object simulations that were described in Chapter III. The focus of this chapter is to present the results of the MV-Z wavefront estimation technique. Comparisons of all four wavefront estimation techniques are made for each performance metric in Appendices B through E. This chapter also presents the results for the extended object simulations in terms of the image intensity distribution,  $i(x, y)$ , and the estimate of the object intensity distribution,  $\tilde{o}(x, y)$ , of a satellite object. Image quality is assessed by using SNR, a correlation coefficient and on-object resolution. Additionally, the matter of implementation of the DWFS method into existing USAF telescopes is discussed.

### 4.2 Optimal Number of Zernike Polynomials

Two of the wavefront estimation techniques used in this study use Zernike polynomials as elementary functions. Section 3.5 discussed the method used to optimize the number of Zernike polynomials,  $J$ . The results of the optimization calculations are shown in Table 7. The values in the parenthesis are for the runs where the tilt aberration was initially removed. An asterisk, \*, indicates that a value for  $J$  was chosen before the minimum value of  $\langle \epsilon^2 \rangle$  was reached. In other words, for these cases, the value of  $\langle \epsilon^2 \rangle$  continued to decrease with an increasing number of Zernike polynomials. This was expected and only occurred for the highest light level MV-Z runs. A few things can be noted from Table 7. In general, it appears the optimal number of Zernike polynomials drops as light level decreases. Also,  $J$  remained constant over  $r_0$  for a particular light level except for the case when  $m_v = 8$

|            |      | $m_v = 0$ | $m_v = 4$ | $m_v = 8$ | $m_v = 12$ |
|------------|------|-----------|-----------|-----------|------------|
| $r_0 = 7$  | LS-Z | 20/(20)   | 20/(20)   | 20/(20)   | 5/(5)      |
|            | MV-Z | 60/(80*)  | 50/(80*)  | 40/(40)   | 5/(5)      |
| $r_0 = 10$ | LS-Z | 20/(20)   | 20/(20)   | 20/(20)   | 5/(5)      |
|            | MV-Z | 60/(80*)  | 50/(80*)  | 30/(30)   | 5/(5)      |
| $r_0 = 15$ | LS-Z | 20/(20)   | 20/(20)   | 10/(10)   | 5/(5)      |
|            | MV-Z | 60/(80*)  | 50/(80*)  | 20/(30)   | 5/(5)      |
| $r_0 = 50$ | LS-Z | 20/(20)   | 20/(20)   | 5/(5)     | 5/(5)      |
|            | MV-Z | 60/(80*)  | 50/(80*)  | 5/(5)     | 5/(5)      |

Table 7. Optimal Number of Zernike Polynomials (values for tilt removed runs are shown in parentheses).

where it dropped with increasing  $r_0$ . Also, there is a distinct difference for the value of optimal  $J$  between the LS-Z and MV-Z estimation techniques. Additionally, there is a difference in the value of optimal  $J$  for the cases where tilt was and was not initially removed. For the LS-Z technique, an increase in  $J$  caused instabilities in some of the matrix inversion operations that had to be performed during the calculation of the reconstruction matrix,  $M_{jn}^{LS}$  in Equation 20. Here, large phase estimation errors occurred for values of  $J$  different from the optimal value. The phase errors at the edges of the pupil were significant and increased the value of  $\langle \varepsilon^2 \rangle$ .

As a typical example, Figure 13 shows the variation in  $\langle \varepsilon^2 \rangle$  for both the LS-Z and MV-Z wavefront estimation techniques for the case when  $m_v = 0$ ,  $r_0 = 7$  cm and when tilt was and was not initially when  $m_v = 0$ ,  $r_0 = 7$  cm and when tilt was and was not initialremoved. Two trends should be noted from this figure. First, notice the more severe restriction for determining the optimal  $J$  for the LS-Z estimation technique. Away from the optimal value, the error significantly increases. The MV-Z estimation technique generally resulted in lower errors as the number of Zernike polynomials increased. A slight increase for the MV-Z cases when tilt was not initially removed was observed. The second thing to notice is the overall slight decrease in error that occurred when the tilt aberration was initially removed.

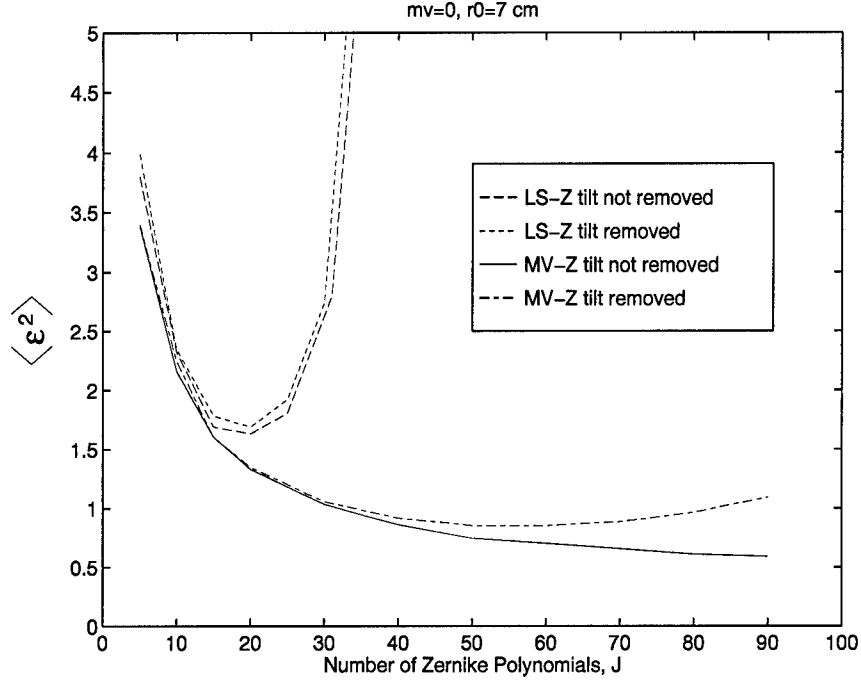


Figure 13. Determining the Optimal Number of Zernike Polynomials.

This study has shown that the performance metrics are sensitive to the choice of  $J$ . The results presented in this thesis would be different if the assumption was made that only a single, non-optimal value of  $J$  was appropriate for all conditions and for both the LS-Z and MV-Z techniques.

#### 4.3 Point Source Simulation Results

The goal of the point source simulations was to determine the comparative general optical performance of each wavefront estimation technique. The matrix of 128 point source simulations defined in Table 4 was conducted and the results are discussed here for each performance metric. A more detailed comparison and analysis of the four wavefront estimation techniques for each performance metric is provided in Appendices B through E. To summarize those results, the MV-Z technique generally out-performed all other techniques for each performance metric. With the exception

of a few examples included to show comparisons of each technique, the results that are presented in this section are specific to the MV-Z estimation technique.

*4.3.1 Average Pupil-Averaged Mean Square Residual Phase Error.* The average pupil-averaged mean square residual phase error defined in Section 2.6.1 is a measure of how well the estimated wavefront phase matches the original wavefront phase. The values of  $\langle \varepsilon^2 \rangle$  for each operational condition are presented in Appendix B in Tables 13 and 14. Incidentally, this metric was also used to determine the optimal number of Zernike polynomials. Figure 14 demonstrates the concept of the pupil-averaged mean square residual phase error. Here, the 200th realization of the original wavefront, the MV-Z estimated wavefront, and the difference between these two wavefronts (the residual wavefront) is shown for  $m_v = 0$ ,  $r_0 = 7$  cm and tilt not initially removed. The pupil-averaged mean square residual phase error,  $\varepsilon^2$ , for the estimation of this particular phase screen was  $0.825 \text{ rad}^2$ . The average pupil-averaged mean square residual phase error,  $\langle \varepsilon^2 \rangle$ , over all 200 phase screen realizations was  $0.85591 \text{ rad}^2$ .

*4.3.2 Average System Transfer Function.* A comparative analysis of the average system transfer function performance of each of the four wavefront estimation techniques is made in Appendix C where plots of the average system transfer function as a function of normalized spatial frequency are shown in Figures 31 through 38. Figure 15 shows a typical result where the average system transfer function for each of the four wavefront estimation techniques is displayed for the case where  $m_v = 4$ ,  $r_0 = 10$  cm, and tilt was initially removed.

Figures 16 and 17 show how the average system transfer function varies for the best performing wavefront estimation technique (MV-Z) over the different telescope operational conditions. Figure 16 is for the runs where tilt was not removed and Figure 17 shows the results for those runs where tilt was initially removed. A given frame in each figure shows how the average OTF changes with  $r_0$  for a particular

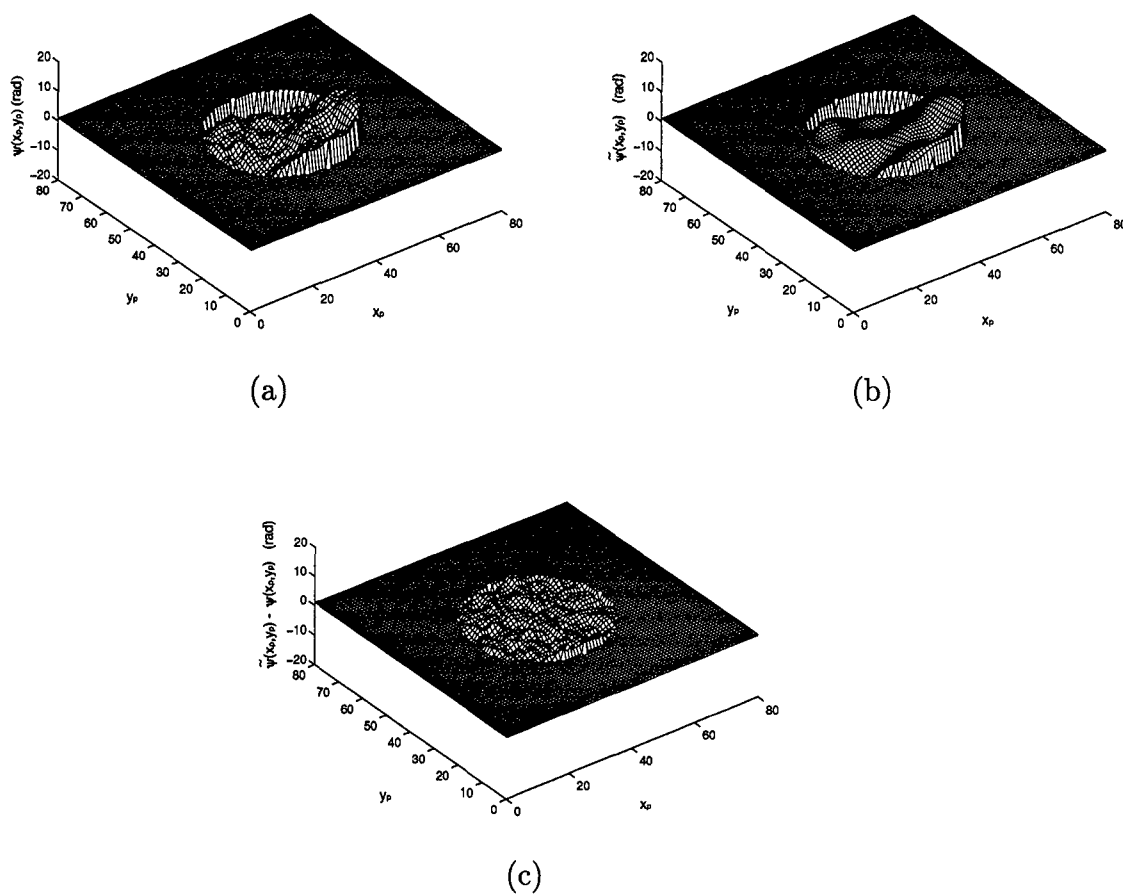


Figure 14. (a) Original Wavefront,  $\psi(\vec{x}_p)$  (b) Estimated Wavefront,  $\tilde{\psi}(\vec{x}_p)$ , (c) Residual Wavefront,  $\tilde{\psi}(\vec{x}_p) - \psi(\vec{x}_p)$ .

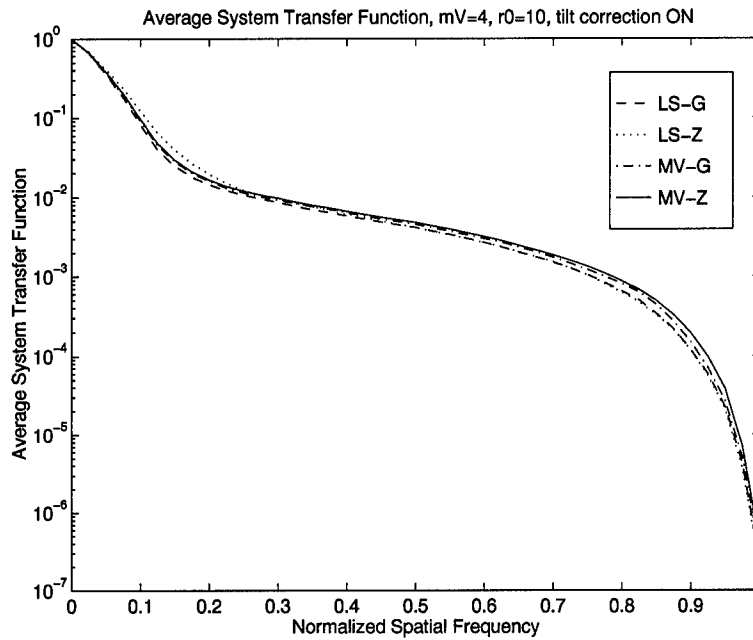


Figure 15. Average System Transfer Function for  $m_v = 4$ ,  $r_0 = 10$  cm (tilt corrected).

light level as a function of normalized spatial frequency. Note the effects of noise at the lowest light levels and how tilt removal increases performance.

*4.3.3 SNR of System Transfer Function.* A comparative analysis of the signal-to-noise ratio of the system transfer function for each of the four wavefront estimation techniques is made in Appendix D where Figures 39 through 46 show the system transfer function as a function of normalized spatial frequency. The MV-Z estimator out-performed all others with the performance improvement being most significant at the highest spatial frequencies. This is important because it is at these high spatial frequencies that the detail of the image is contained. The SNR of the system transfer function for each wavefront estimation technique is shown in Figure 18 for the case where  $m_v = 4$ ,  $r_0 = 10$  cm, and tilt was initially removed.

Figures 19 and 20 show how the SNR of the system transfer function using the MV-Z technique changes for different telescope operational conditions. Figure 19 is for the runs where tilt was not removed and Figure 20 shows the results for those



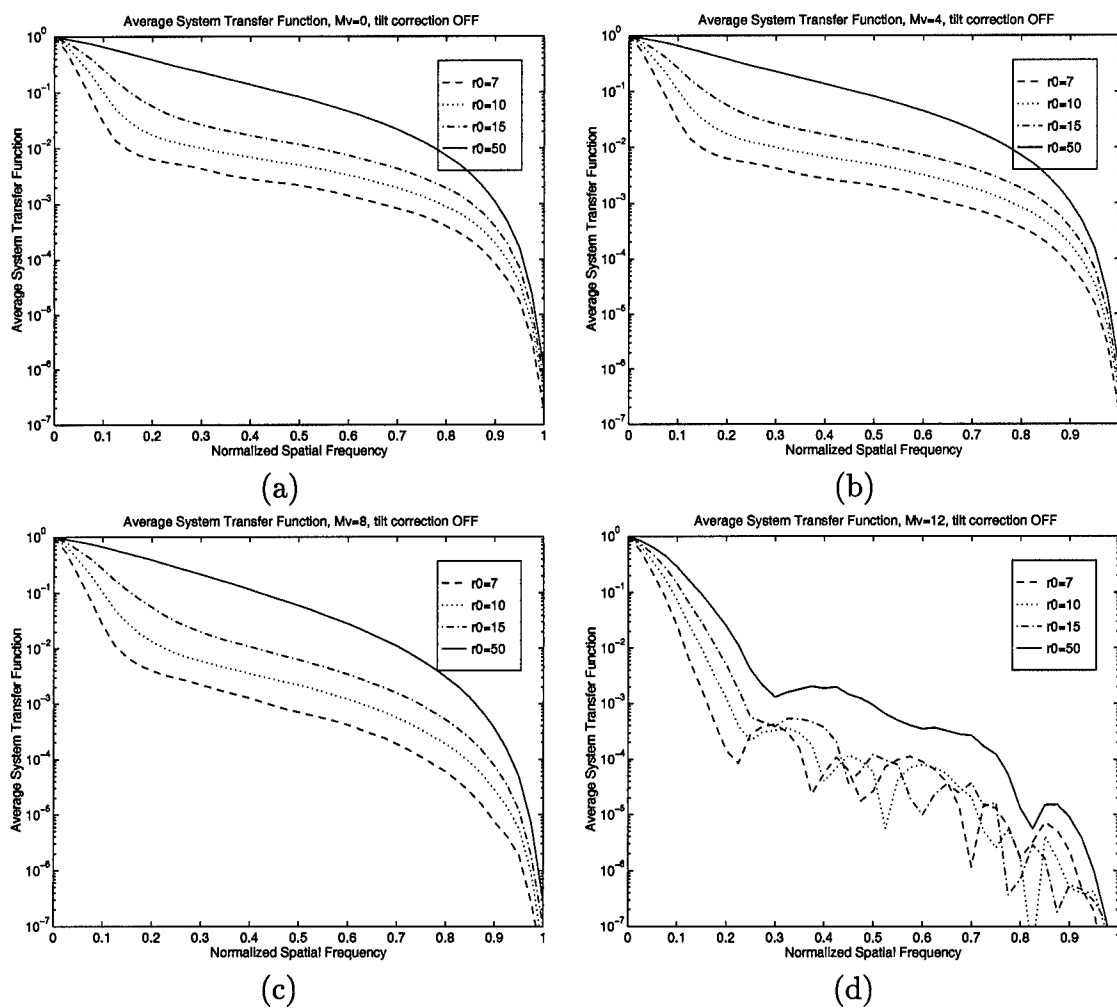


Figure 16. Average System Transfer Function for MV-Z Technique: (a)  $m_v=0$ , (b)  $m_v=4$ , (c)  $m_v=8$ , (d)  $m_v=12$ .

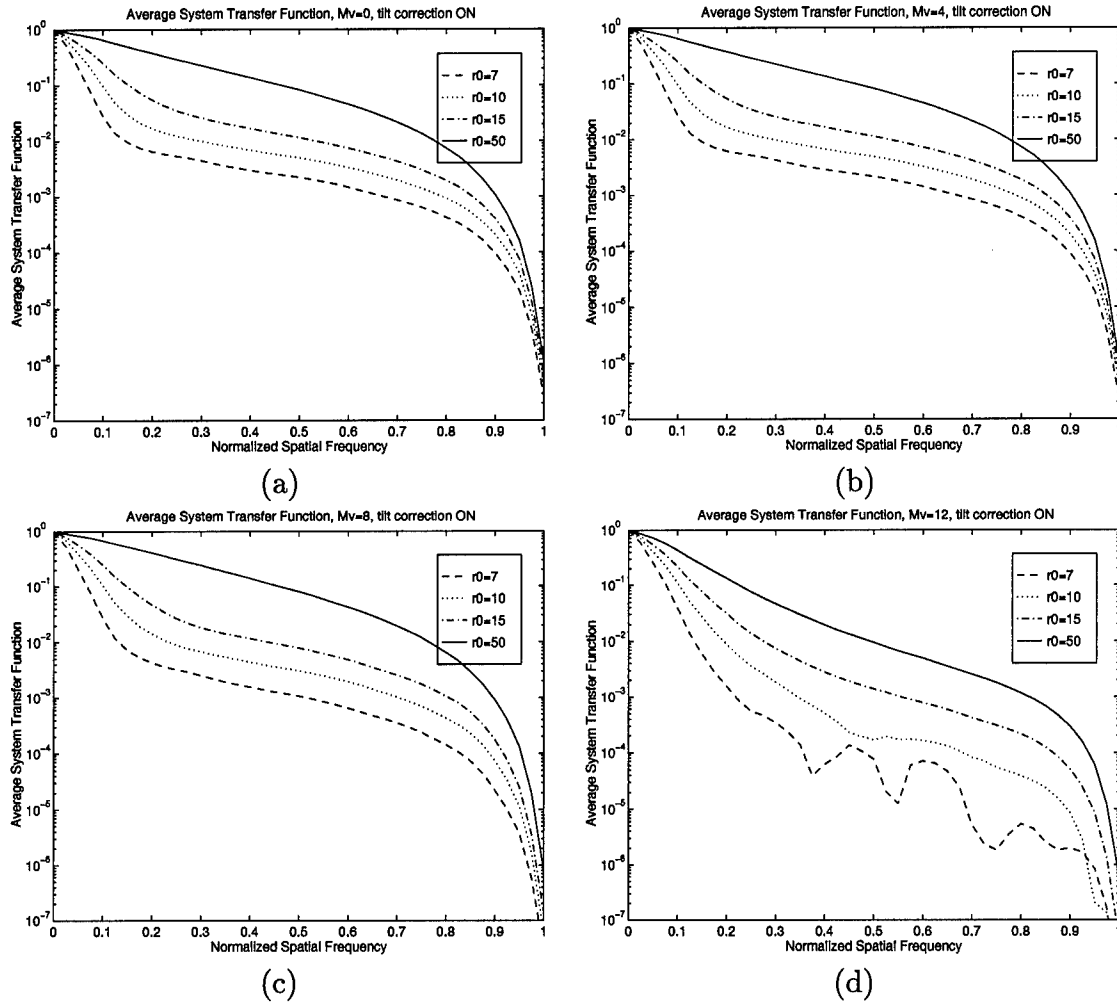


Figure 17. Average System Transfer Function for MV-Z Technique (tilt corrected):  
(a)  $m_v=0$ , (b)  $m_v=4$ , (c)  $m_v=8$ , (d)  $m_v=12$ .

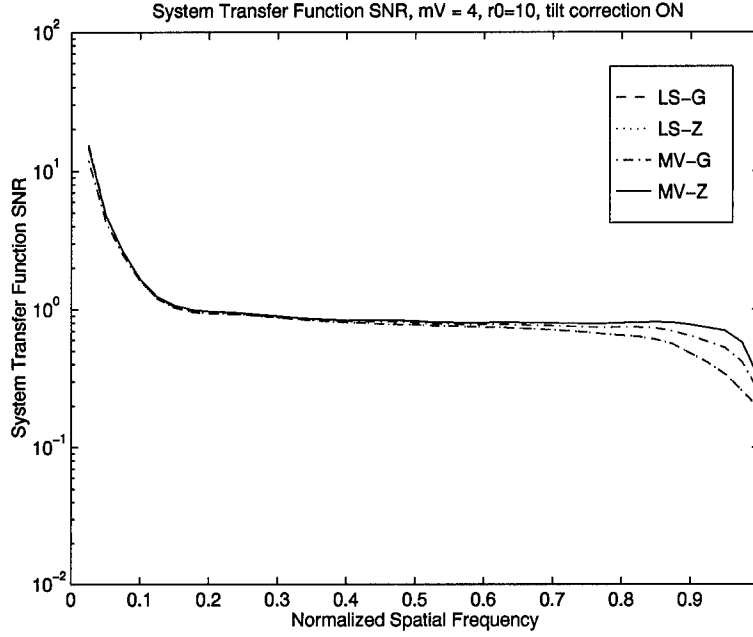


Figure 18. System Transfer Function SNR for  $m_v = 4$ ,  $r_0 = 10$  cm (tilt corrected).

runs where tilt was initially removed. A given frame in each figure shows how the system transfer function SNR changes with  $r_0$  for a given light level as a function of normalized spatial frequency.

**4.3.4 OTF Correlation.** A comparative analysis of the average OTF correlation for each of the four wavefront estimation techniques is made in Appendix E where Figures 47 through 54 show  $\gamma_{H\hat{H}}(\vec{f})$  as a function of normalized spatial frequency for each of the point source simulations defined in Table 4. The MV-Z estimation technique out-performed all others with the performance improvement being most significant at the highest spatial frequencies. An example of the OTF correlation output for each wavefront estimation technique is shown in Figure 21. This is for the case where  $m_v = 4$ ,  $r_0 = 10$  cm, and tilt was initially removed.

Figures 22 and 23 show the variation in the OTF correlation for the MV-Z technique and the different telescope operational conditions defined in Table 4. Figure 22 is for the runs where tilt was not removed and Figure 23 shows the results

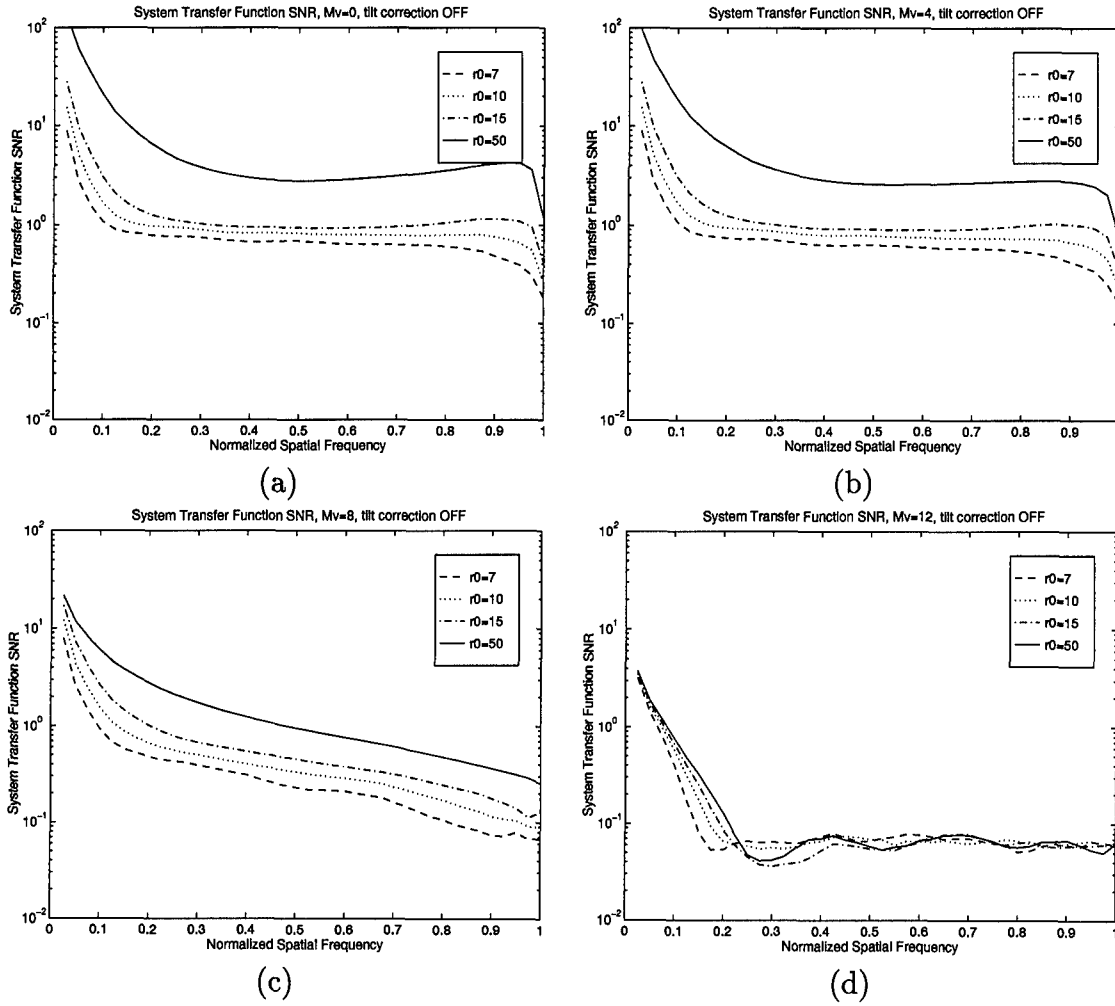


Figure 19. System Transfer Function SNR for MV-Z Technique: (a)  $m_v=0$ , (b)  $m_v=4$ , (c)  $m_v=8$ , (d)  $m_v=12$ .

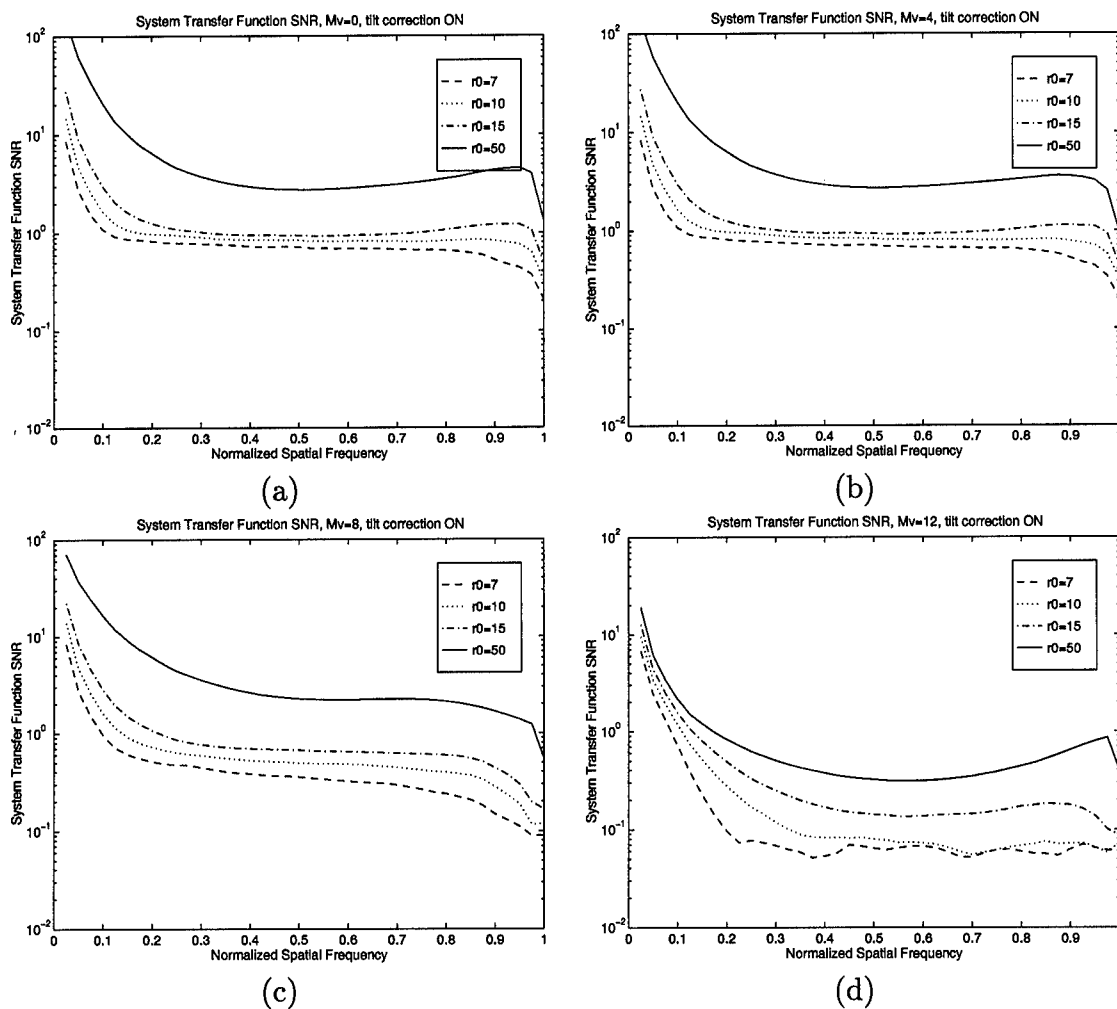


Figure 20. System Transfer Function SNR for MV-Z Technique (tilt corrected): (a)  $m_v=0$ , (b)  $m_v=4$ , (c)  $m_v=8$ , (d)  $m_v=12$ .

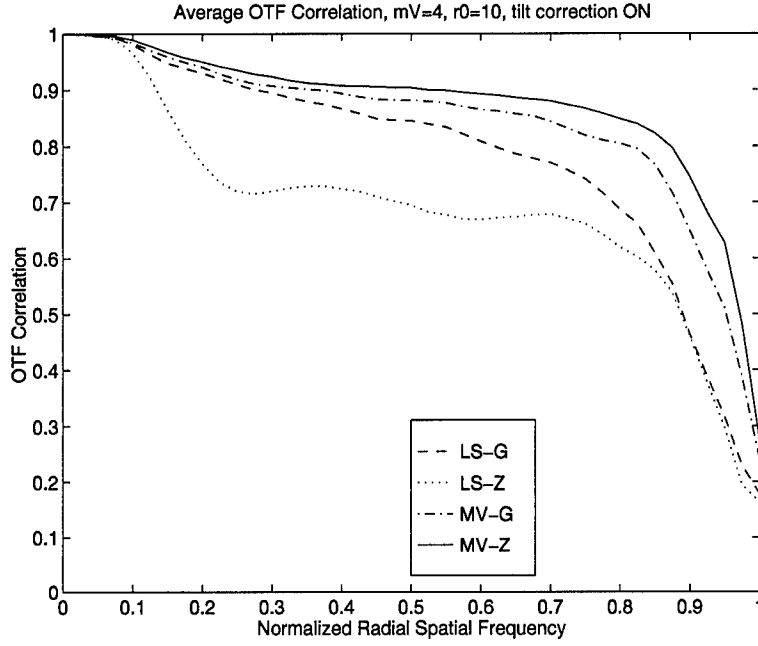


Figure 21. OTF Correlation for  $m_v = 4$ ,  $r_0 = 10$  cm (tilt corrected).

for those runs where tilt was initially removed. A given frame in each figure shows how  $\gamma_{H\tilde{H}}(\vec{f})$  changes with  $r_0$  for a particular light level as a function of normalized spatial frequency.

#### 4.4 Extended Object Simulation Results

This section presents the results for the extended object simulations. Recall that the objectives for running extended object simulations were two-fold. First, they allow for a tangible assessment and demonstration of the DWFS method. Second, they were conducted to quantify the improvements in the object estimate between the DWFS methods that use the MV-Z and the LS-Z wavefront estimation techniques. Three metrics were used to assess the quality of the object intensity distribution estimate,  $\tilde{o}(x, y)$ . The first metric is the signal-to-noise ratio of the estimate of the object spectrum. Second, a correlation coefficient is used to determine which technique's object estimate intensity distribution,  $\tilde{o}(x, y)$ , correlates better with the

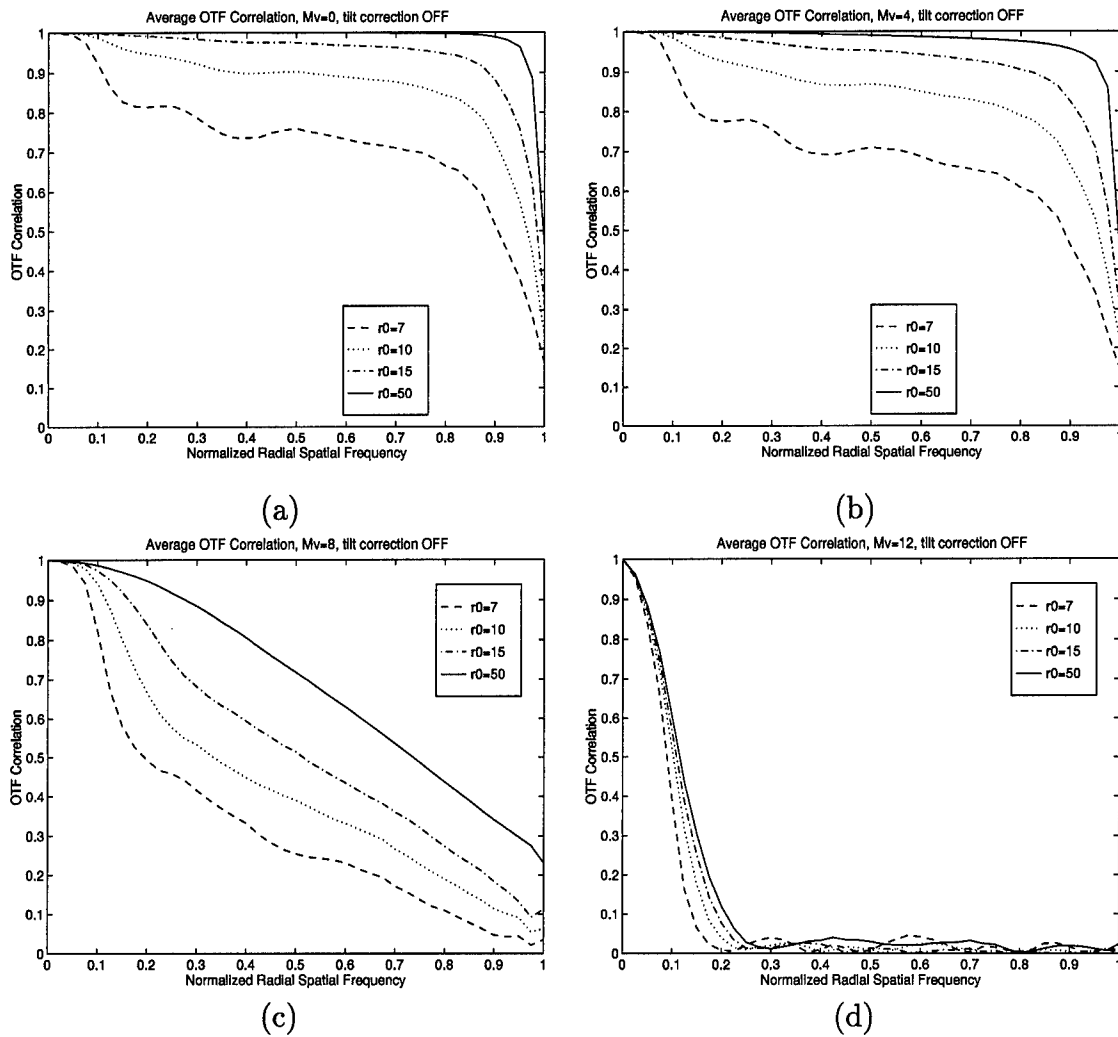


Figure 22. OTF Correlation for MV-Z Technique: (a)  $m_v=0$ , (b)  $m_v=4$ , (c)  $m_v=8$ , (d)  $m_v=12$ .

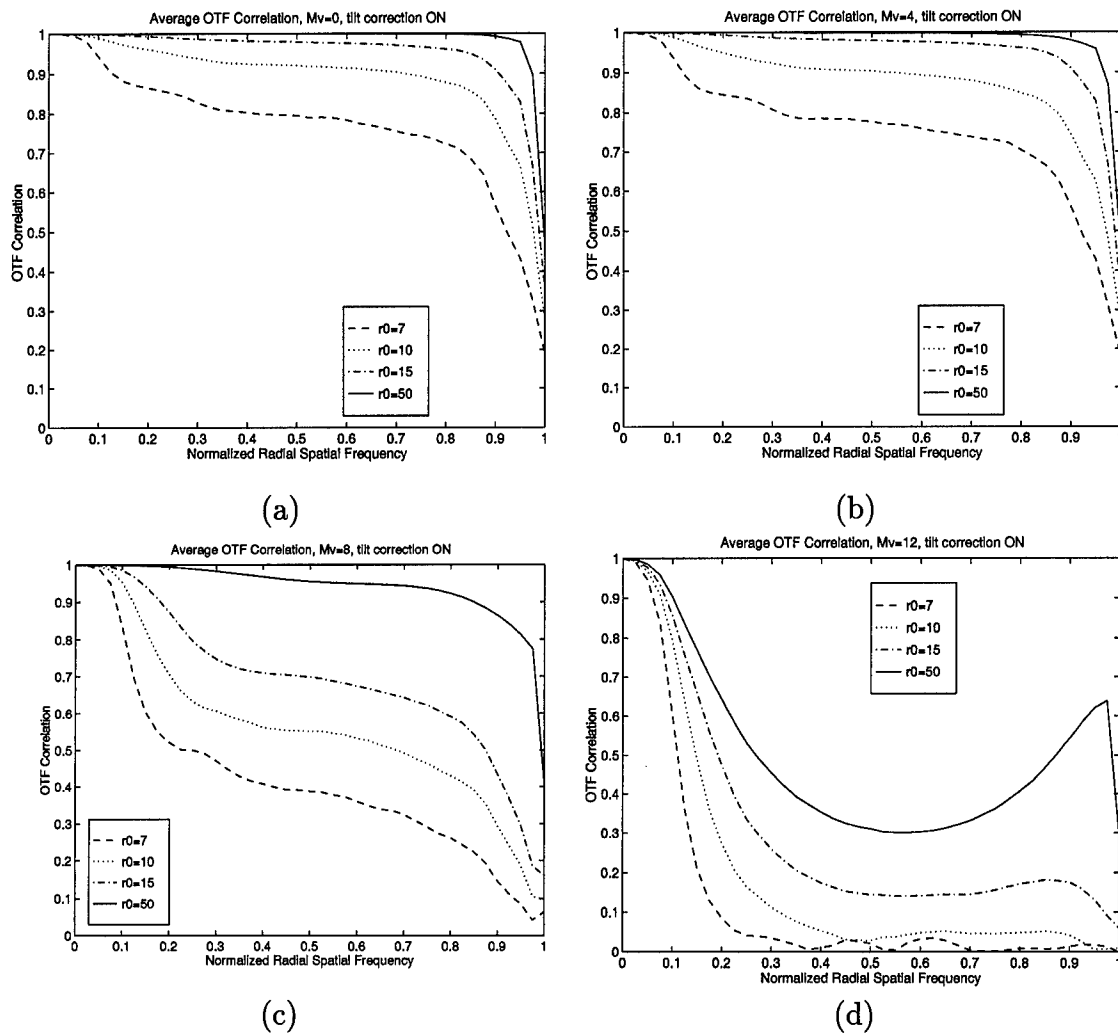


Figure 23. OTF Correlation for MV-Z Technique (tilt corrected): (a)  $m_v=0$ , (b)  $m_v=4$ , (c)  $m_v=8$ , (d)  $m_v=12$ .



original object intensity distribution,  $o(x, y)$ . The third metric is an assessment of the on-object resolution.

*4.4.1 DWFS Demonstration Results.* Figures 24 and 25 demonstrate the improvements in image quality that occur with the application of the DWFS method for typical telescope operational conditions. These simulations were conducted using the parameters outlined in Table 5. Results are shown for a generic satellite that is overhead at ranges corresponding to low Earth orbit and geosynchronous orbit altitudes. These figures are a direct comparison of the uncorrected image of a generic satellite and the improved image (object estimate) obtained when DWFS is used. Also shown in each figure is the signal-to-noise ratio of the original image spectrum (before applying DWFS) and the signal-to-noise ratio of the object spectrum estimate (after applying DWFS). Figure 24 shows an obvious visual improvement in image resolution and the increase in SNR that results from applying DWFS for a satellite in LEO. In terms of the Seyrafi's information levels, DWFS improves this image from detection to recognition and possibly identification. For GEO, the improvement is not visually obvious but an improvement in SNR is apparent for the case where DWFS was applied. This increase in SNR could improve the ability to detect objects in GEO.

*4.4.2 Comparison of LS-Z and MV-Z Object Estimates.* In this section, the results of extended object simulations that quantify the differences in image quality between the two estimation techniques that employ Zernike polynomials as elementary functions (LS-Z and MV-Z) are presented. This allows for a direct comparison of the modification to the DWFS method introduced in this thesis with a previous DWFS method. The parameters used for these simulations are listed in Table 6. Recall that for these simulations, the turbulence level was set at a typical level, tilt was initially removed, the optimal number of Zernike polynomials was used, and visual magnitudes of 0, 4, 8, and 12 were used. The differences between

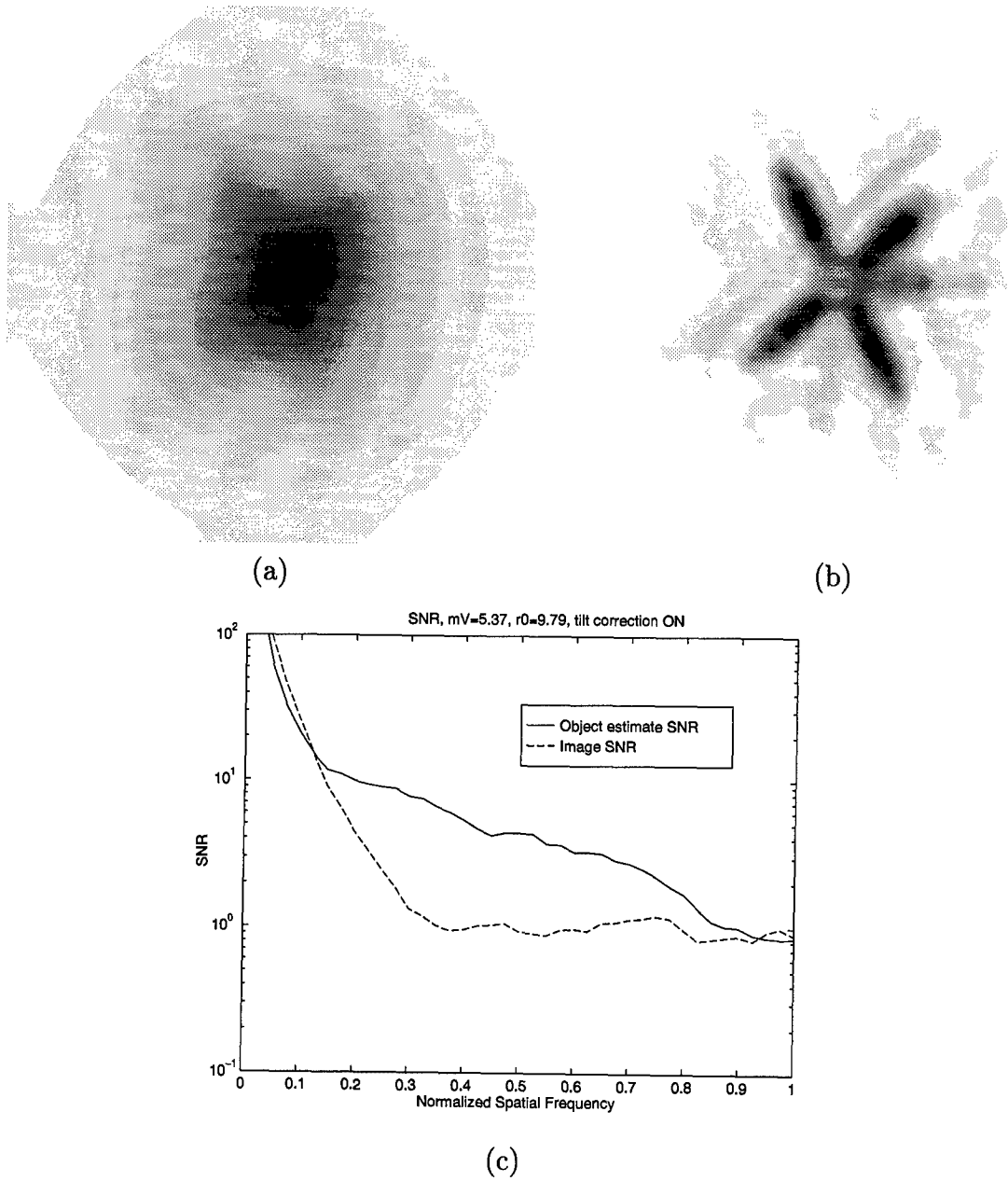


Figure 24. LEO Imaging, Range = 500 km,  $m_v = 5.37$ ,  $r_0 = 9.79$  cm: (a) Image Intensity Distribution,  $i(\vec{x})$ , (b) DWFS MV-Z Object Estimate,  $\tilde{o}(\vec{x})$ , (c) Image SNR and Object Estimate SNR.

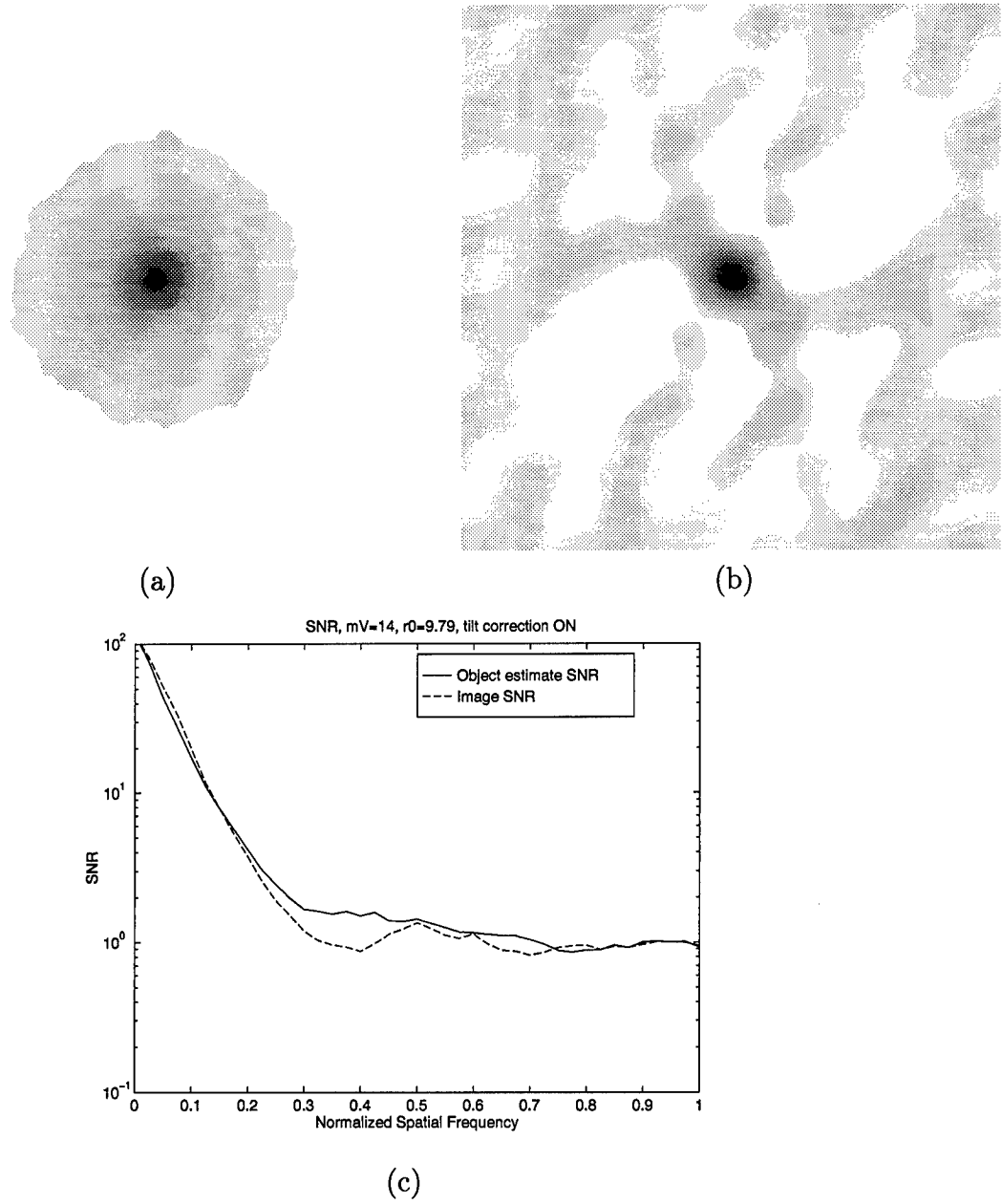


Figure 25. GEO Imaging, Range = 35780 km,  $m_v = 14$ ,  $r_0 = 9.79$  cm: (a) Image Intensity Distribution,  $i(\vec{x})$ , (b) MV-Z DWFS Object Estimate,  $\tilde{o}(\vec{x})$ , (c) Image SNR and Object Estimate SNR.

the two techniques are demonstrated through the use of the signal-to-noise ratio, by determining the correlation coefficient of the object estimate (the corrected image) and the original object, and by determining the on-object resolution improvement.

*4.4.2.1 SNR.* Figures 26 through 29 show the object estimate,  $\tilde{o}(x, y)$ , for each technique along with a comparative plot of the SNR. The SNR plot shows the SNR of the object spectrum estimate for each technique as well as the SNR of the (uncorrected) image spectrum for reference. Differences in resolution for each technique are not obvious from a visual inspection of the object estimate. The MV-Z technique has a better estimated object spectrum SNR especially for the brightest light levels. Note the general decrease in image quality for decreasing light levels. The SNR plots for each figure show that the MV-Z technique outperforms the LS-Z technique for all light levels with the most significant improvements occurring for the highest light levels. The SNR plots for the three highest light levels also show the general improvement in the SNR of the object spectrum estimate over the SNR of the image spectrum. Note that for the lowest light level ( $m_v = 12$ ) it appears that the DWFS technique was not effective because the SNR of the object spectrum estimate for both techniques was worse than the SNR of the image spectrum. However, in terms of a visual inspection the DWFS object estimate, frame (b) of Figure 29 appears to contain characteristics of the original object structure where frame (a) does not.

*4.4.2.2 Correlation Coefficient.* The correlation coefficients between original object,  $o(x, y)$ , and the object estimate,  $\tilde{o}(x, y)$ , for the LS-Z and MV-Z wavefront phase estimation techniques are shown in Table 8. Results show that the correlation coefficients for the MV-Z technique are slightly better than the correlation coefficients for the LS-Z technique. This indicates that the corrected image created using the MV-Z technique more closely correlates with the original object. These results are consistent with the SNR results.

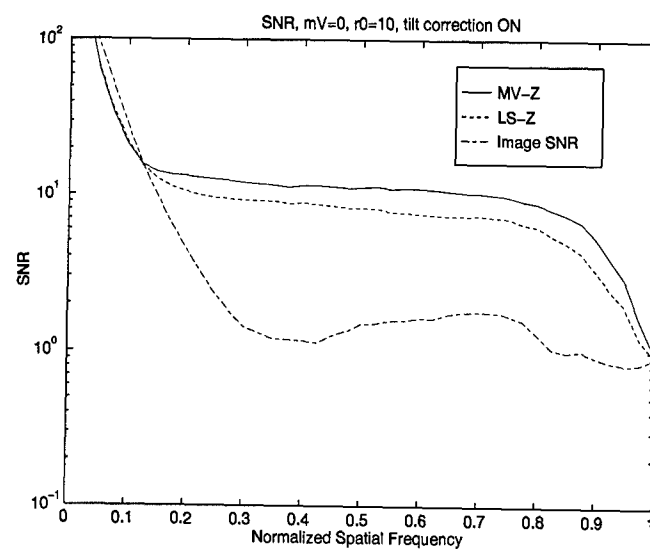
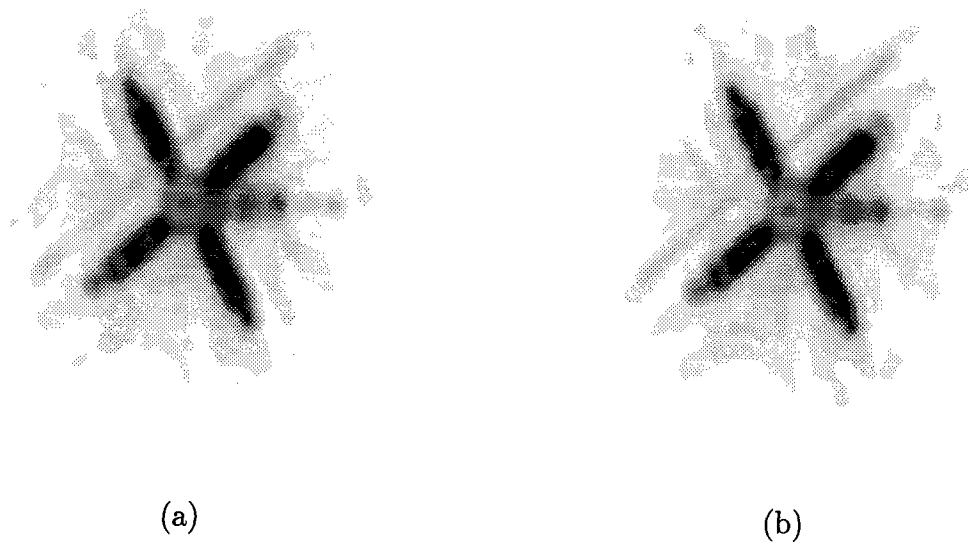


Figure 26. LS-Z and MV-Z Object Estimates for  $m_v = 0$ ,  $r_0 = 10$  cm: (a) LS-Z Object Estimate, (b) MV-Z Object Estimate, (c) Image SNR and Object Estimate SNR.

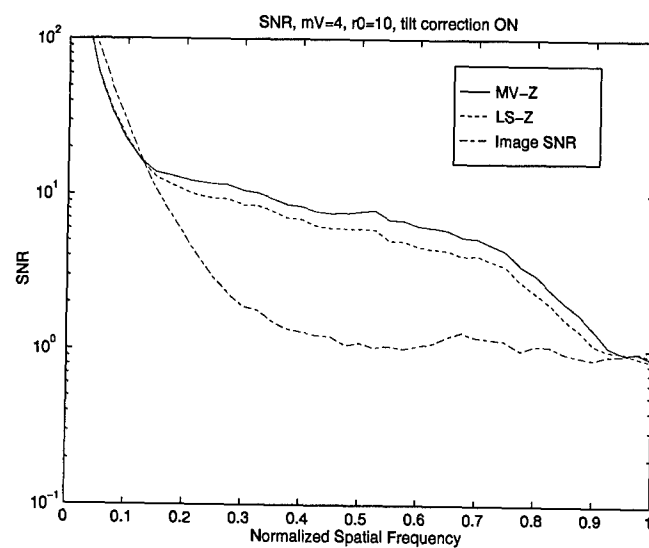
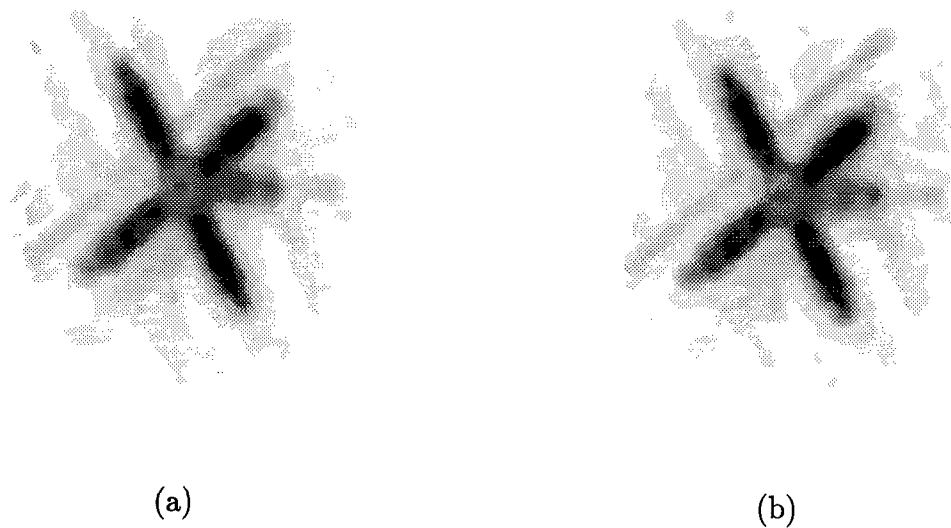
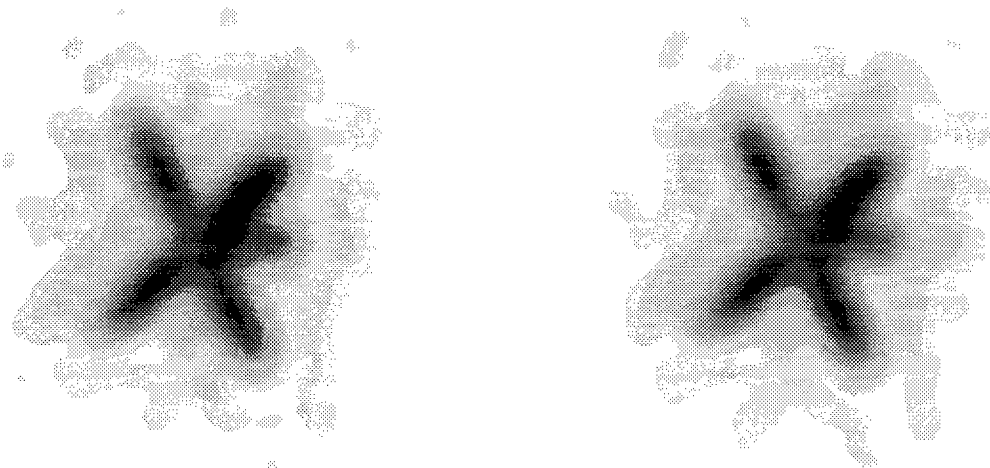
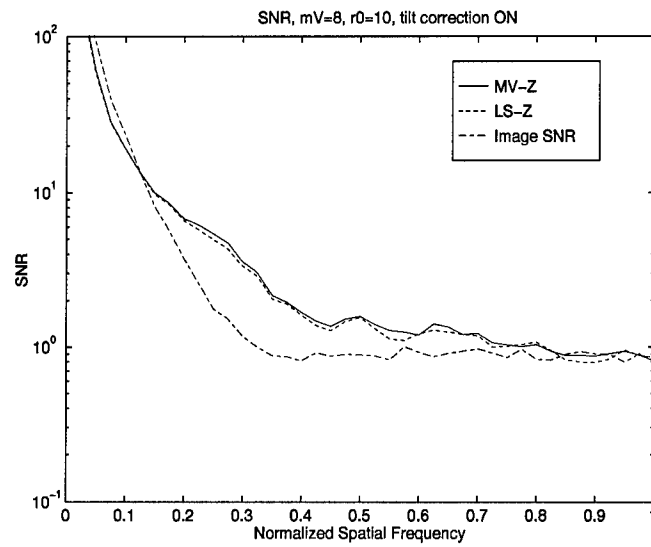


Figure 27. LS-Z and MV-Z Object Estimates for  $m_v = 4$ ,  $r_0 = 10$  cm: (a) LS-Z Object Estimate, (b) MV-Z Object Estimate, (c) Image SNR and Object Estimate SNR.



(a)

(b)



(c)

Figure 28. LS-Z and MV-Z Object Estimates for  $m_v = 8$ ,  $r_0 = 10$  cm: (a) LS-Z Object Estimate, (b) MV-Z Object Estimate, (c) Image SNR and Object Estimate SNR.

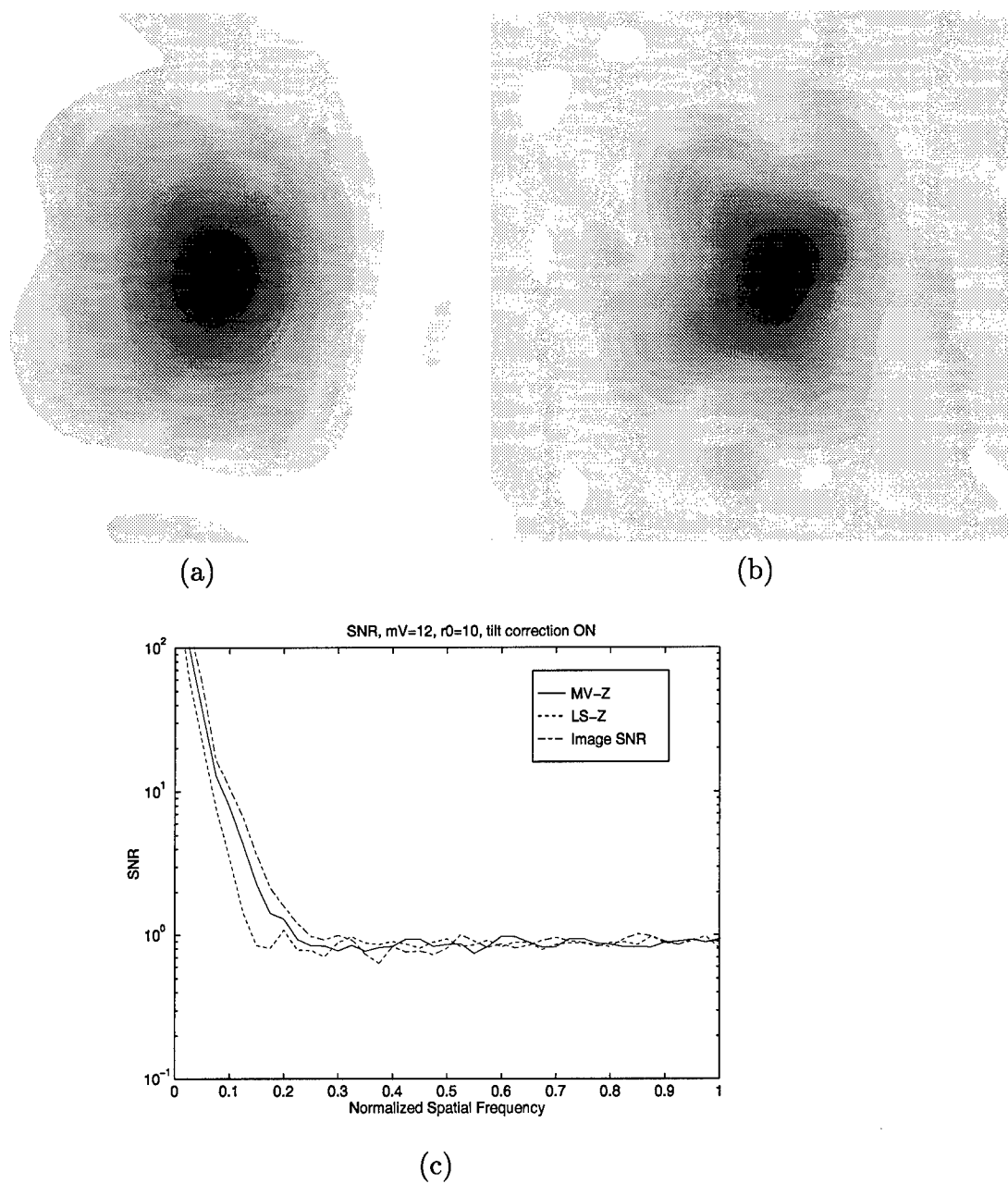


Figure 29. LS-Z and MV-Z Object Estimates for  $m_v = 12$ ,  $r_0 = 10$  cm: (a) LS-Z Object Estimate, (b) MV-Z Object Estimate, (c) Image SNR and Object Estimate SNR.



|            | LS-Z   | MV-Z   |
|------------|--------|--------|
| $m_v = 0$  | 0.9408 | 0.9440 |
| $m_v = 4$  | 0.9311 | 0.9366 |
| $m_v = 8$  | 0.8620 | 0.8628 |
| $m_v = 12$ | 0.6595 | 0.7083 |

Table 8. Object Estimate Correlation Coefficient.

|            | Before DWFS | After DWFS |
|------------|-------------|------------|
| $m_v = 0$  | 1.33 m      | 0.39 m     |
| $m_v = 4$  | 1.46 m      | 0.43 m     |
| $m_v = 8$  | 1.63 m      | 1.05 m     |
| $m_v = 12$ | 2.09 m      | 2.44 m     |

Table 9. On-object Resolution.

*4.4.2.3 DWFS Resolution Improvement.* Table 9 shows the on-object resolutions for the satellite object at a range of 500 km. These results are for an atmospheric coherence diameter value of 10 cm, and visual magnitudes of 0, 4, 8, and 12. The simulations were run using the MV-Z phase estimation technique where tilt was initially removed. The resolutions were calculated using Equation 48 for a one-meter aperture telescope with an imaging wavelength of  $0.6 \mu\text{m}$ . The diffraction-limited resolution at 500 km is 0.37 m. However, the diffraction-limited resolution for the GEO altitude is 26.19 m. Therefore, no details of the 10 m satellite at the GEO range could be resolved. This is consistent with Figure 25. An improvement in resolution for objects in GEO is still important for object detection. Note that the resolution did not improve for the low light level case, which is consistent with the correlation coefficient and signal-to-noise ratio results presented in Section 4.4.2.1.

#### 4.5 Implementation

This section addresses the question of how DWFS can be used by the USAF. This thesis has demonstrated that DWFS offers increased resolution without the expensive elements of adaptive optics systems. This increase in resolution is useful for detection, orientation, recognition, and identification. It increases the ability to

resolve detail on an object and the ability to detect small objects. For these reasons, DWFS appears to be an effective way to provide additional optical imaging assets to the USAF.

*4.5.1 USAF Optical Sites.* The USAF has a total of 26 space surveillance sites located throughout the world. This network consists of a combination of radar and optical facilities. There are 8 optical sites that currently contribute to the space surveillance mission. These include four Ground-based Electro-Optical Deep Space Surveillance (GEODSS) sites, the Air Force Maui Optical Station (AMOS), Maui Optical Tracking and Identification Facility (MOTIF), the Starfire Optical Range (SOR), and the Experimental Test System (ETS) (9, 12, 16, 20). Of the eight optical systems, only SOR and AMOS have the capability (through the use of adaptive optics) to compensate for atmospheric turbulence effects (12, 20). The location of the USAF optical sensors is shown in Figure 30 (5, 20). Also shown in this figure is the field of view of these sensors at a 500 km altitude.

The USAF categorizes space surveillance sensors based on the level of contribution each makes to the space surveillance mission. *Dedicated sensors* are those with a primary mission of space surveillance, *contributing sensors* are those which are owned and operated by other agencies but, through agreement, are occasionally tasked to provide space surveillance data as a secondary mission. *Collateral sensors* are USAF assets that have a primary mission other than space surveillance (12, 20). A summary of the USAF optical sites, their locations, and their surveillance mission category is presented in Table 10.

*4.5.1.1 GEODSS.* The primary mission of the GEODSS sites is the surveillance of deep space and the geosynchronous satellite belt (4, 12, 16). A secondary mission includes LEO taskings for space debris detection (13). A typical GEODSS site has three separate observatories. These include two primary Cassegrain telescopes each having one-meter diameter apertures and 2° fields-of-

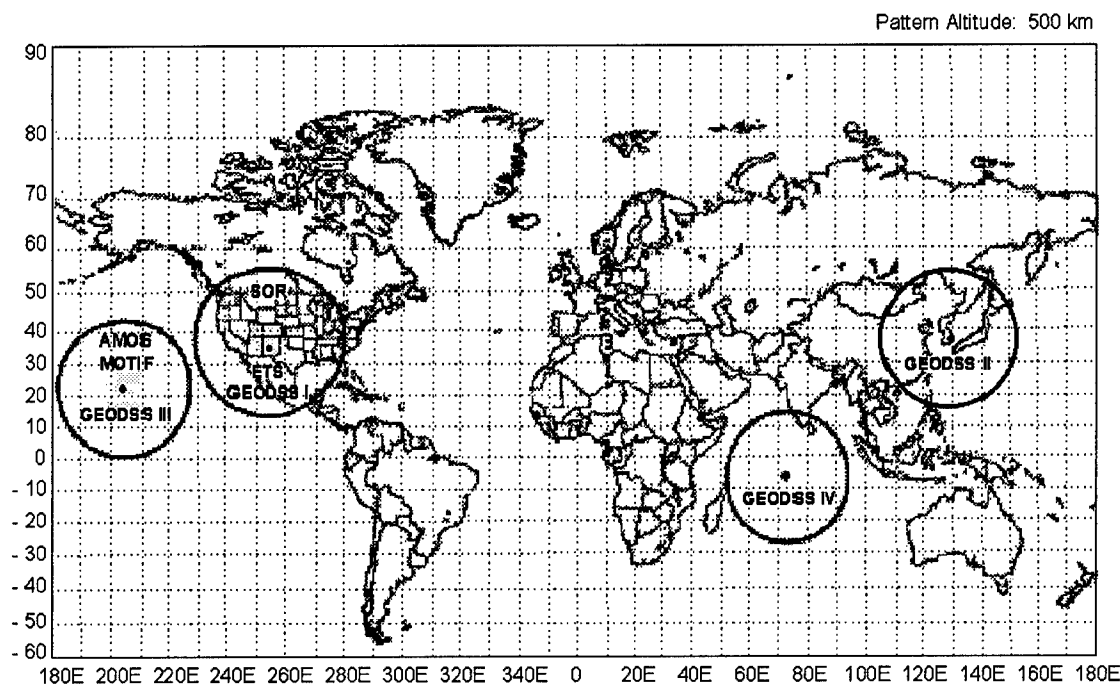


Figure 30. USAF Optical Space Surveillance Sites (5, 20).

view (FOV) and one auxiliary folded-Schmidt telescope with a 0.38 meter aperture and a larger  $6^\circ$  FOV which is good for object acquisition. These systems have mounts that enable the telescopes to track objects. Traditionally the GEODSS sites have been used for deep-space surveillance and can operate down to  $16.5 m_v$  (13, 16). There is also a GEODSS research and development prototype site operated by the Massachusetts Institute of Technology called the Experimental Test System (ETS). ETS has two 0.8 meter telescopes with EBSICON cameras (9). Proposed upgrades to GEODSS under the space surveillance network improvement program include development of prototype charged coupled devices to replace the EBSICON cameras, development of a relocatable prototype GEODSS system, mission hardware and software upgrades, and the development of an integrated space operations center (4).

**4.5.1.2 MOTIF.** The Maui Optical Tracking and Identification Facility (MOTIF) is a dedicated sensor that consists of two 1.2 meter telescopes that

| System     | Location                       | AO ? | SSN Category |
|------------|--------------------------------|------|--------------|
| AMOS       | Hawaii<br>(29.7N 203.7E)       | YES  | Contributing |
| MOTIF      | Hawaii<br>(20.7N, 203.7E)      | NO   | Dedicated    |
| GEODSS I   | CONUS<br>(33.8N, 253.3E)       | NO   | Dedicated    |
| GEODSS II  | South Korea<br>(35.7N, 128.6E) | NO   | Dedicated    |
| GEODSS III | Hawaii<br>(20.7N, 203.7E)      | NO   | Dedicated    |
| GEODSS IV  | Diego Garcia<br>(7.4S, 72.5E)  | NO   | Dedicated    |
| ETS        | CONUS<br>(33.8N, 253.3E)       | NO   | Contributing |
| SOR        | CONUS<br>(35.1N, 253.3E)       | YES  | Contributing |

Table 10. USAF Electro-Optical Telescopes (16, 20).

operate on a single mount. Optical and IR signatures on objects as faint as 19th visual magnitude can be obtained (16).

*4.5.1.3 AMOS.* The Air Force Maui Optical Station (AMOS) consists of a 1.6 meter telescope that includes a laser radar system called the beam director tracker, and an AO system that uses a deformable mirror. AMOS is a testbed for new surveillance technologies. It also maintains an infrared database for space objects. Its primary mission is research and development but it also serves as a contributing sensor for the SSN (12, 20).

*4.5.1.4 SOR.* The Starfire Optical Range (SOR) has a 3.5 meter telescope, a 1.5 meter telescope, and a 1.0 meter beam director. It is a research center for optical wavefront control technologies and is operated by the USAF Phillips Laboratory (6).

The justification for the implementation of the DWFS method into USAF telescopes comes from the deficiencies documented in the 1993 fiscal year space surveillance Mission Area Plan. Deficiencies that could be addressed with the implementation of DWFS into USAF telescopes include: incomplete space object catalog, limited space intelligence support, and high operations and maintenance costs (19). An auxiliary imaging capability could result from using DWFS in the current USAF sensors that do not use AO. This would provide more space surveillance assets for imagery. DWFS would, however, add to operations and maintenance cost. For this reason a cost effectiveness study should be conducted to determine if the utility of improved capabilities outweigh the costs involved.

DWFS would be best implemented in one or more of the six optical sites that do not currently have adaptive optics capabilities. Initial testing in one of the research and development sites could allow operational procedures and techniques to be developed. An established and proven technique could then be implemented into the GEODSS sites where the primary detection and tracking missions could occasionally be supplemented with taskings for object imaging. Also, the general increase in resolution could be utilized to improve the completeness of the space object catalog. Since DWFS is a relatively cheap way to mitigate the effects of atmospheric turbulence on imaging it could be implemented without expensive modifications. The required equipment includes a wavefront sensor, high speed shutter, beam splitter, computer workstation and software for image post-processing, and a reference beacon. A natural reference beacon using a guide star could be used but the use of an artificial laser beacon would increase the opportunities for imaging objects.

#### *4.6 Summary*

This chapter has presented the results of the DWFS point source and extended object simulations. These simulations quantified the general imaging system performance and demonstrated the operational performance of the DWFS method. Point

source object simulations were conducted over a variety of telescope operational conditions and established the general imaging performance for the four different wavefront estimation techniques. Overall, the results showed that the minimum variance wavefront estimation technique that used Zernike polynomial elementary functions offered the best performance. Next, extended object simulations demonstrated the improvements in operational performance that DWFS can bring to ground-based telescopes. The extended object simulations also quantified the improvements in image resolution that result from the application of minimum variance wavefront estimation techniques over previous least squares estimation techniques for typical telescope operating conditions. Finally, a preliminary analysis suggests that implementation of DWFS into USAF telescopes could reduce current space surveillance deficiencies.

## *V. Conclusions*

### *5.1 Introduction*

Remotely imaging space objects from the ground is an important mission of the United States Air Force (USAF) and it presents several challenges. One of the most significant challenges is due to the adverse effects that atmospheric turbulence has on the performance of ground-based imaging systems. One of the existing mitigation methods is called Deconvolution from Wavefront Sensing (DWFS). DWFS is an alternative to mechanically extensive adaptive optics systems. It combines the use of measurements from a wavefront sensor and image post-processing to boost the resolution of space object images taken through atmospheric turbulence.

This thesis improved the DWFS method by implementing minimum variance wavefront estimation techniques that used both two-dimensional Gaussian and Zernike polynomial elementary functions. The minimum variance estimation technique accounts for the known statistics of the measured wavefront. Imaging simulations were used to quantify the performance of these wavefront estimation techniques.

### *5.2 Summary of Research Advancements*

This thesis is the first work to implement minimum variance wavefront estimation techniques into the DWFS method and the first to use Zernike polynomial elementary functions with the minimum variance wavefront estimation technique. Additionally, it is the first to optimize the number of Zernike polynomials over a variety of light levels and turbulence conditions. In addition to establishing general imaging performance for point source objects, this thesis assessed operational imaging performance by simulating the imaging of extended objects for realistic operational conditions. This, along with an implementation investigation provided the first steps toward establishing the operational utility of DWFS.

### *5.3 Summary of Results Obtained*

- The deconvolution from wavefront sensing atmospheric turbulence mitigation method was modified by incorporating minimum variance wavefront estimation techniques that employed two-dimensional Gaussian and Zernike polynomial elementary functions.
- The minimum variance technique that used Zernike polynomial elementary functions was shown to provide lower residual error and superior OTF, signal-to-noise ratio and image quality over previous wavefront estimation techniques.
- The biggest performance improvements occurred at the highest spatial frequencies for the brightest objects imaged through the most turbulent atmospheric conditions and for the cases when tilt was not initially removed.
- Simulations were conducted that demonstrated and quantified the improvement in telescope performance that the DWFS techniques can bring to space object imaging.
- It appears that implementing DWFS into existing USAF telescopes would provide an auxiliary imaging capability which would overcome space surveillance mission area deficiencies in a cost effective manner by increasing the number of surveillance assets capable of providing intelligence support and improving the space object catalog.

### *5.4 Conclusions Drawn from Research*

The minimum variance wavefront estimation technique that uses Zernike polynomial influence functions offers improved performance over all other DWFS wavefront estimation techniques for each performance metric. It appears that six USAF optical sites could use DWFS to augment the space surveillance mission. This would help to reduce some of the current USAF space surveillance mission area deficiencies.



### 5.5 Recommendations for Future Research

Further work is needed to investigate the optimization of the number of Zernike polynomials. It was observed that the value of  $\langle \varepsilon^2 \rangle$  did not always correspond to the best OTF, SNR, and OTF correlation. For, example, in some cases, a selection of  $J$  slightly larger than the optimal choice yielded slightly better results in the average OTF, OTF SNR and OTF correlation for some spatial frequencies. Also, the choice of optimal  $J$  could be made on a finer scale. It is also unknown whether or not the optimal choice varies with different telescope configurations or for other simulation parameters that were held constant in this study.

Further research is also needed to investigate the implementation of hybrid or post-processing techniques other than DWFS (*e.g.* speckle imaging) into existing USAF telescopes. A cost effectiveness study is needed to determine whether the utility of implementing DWFS or some other hybrid or post-processing technique outweighs the costs. It would also be useful to look at the effect of using wavefront sensors other than the Hartmann wavefront sensor (*e.g.* shearing interferometer or phase diversity).

Further work should be conducted to determine the performance of the different wavefront estimation techniques for varying telescope parameters such as aperture diameter, imaging wavelength, and subaperture geometry. Also, the use of different image reconstruction techniques after applying DWFS might show improved performance.

### 5.6 Summary

The results obtained indicate that the minimum variance wavefront estimation technique that uses Zernike polynomial elementary functions is the best wavefront estimation technique for improving DWFS imaging performance. The DWFS method was demonstrated to provide significant improvement in imaging capability for tele-

scope operations and could be implemented to reduce current space surveillance deficiencies.

## *Appendix A. Programs and Simulation Parameters*

### *A.1 Computer Programs*

The computer programs listed in Table 11 were used to generate the results that were presented in this thesis.

### *A.2 Simulation Input Parameters*

Input parameters for these programs are presented in Table 12.

| Code         | Function       |
|--------------|----------------|
| sholoz3.f    | LS-Z           |
| sholo4.f     | LS-G, MV-G     |
| sholo4z.f    | MV-Z           |
| sholozimg3.f | LS-Z (imaging) |
| sholozimg4.f | MV-Z (imaging) |

Table 11. Simulation Programs.

| Parameter   | Variable Name | Value                          |
|---|---------------|--------------------------------|
| Number of frames  | nframes       | 200                            |
| Number of subapertures<br>across diameter                 | iradius       | 10                             |
| Random seed   | iseed         | 732939                         |
| Mirror diameter   | dmir          | 1.0 m                          |
| Obscuration diameter                                      | lobs          | 0.0                            |
| Imaging wavelength  | wvl           | 0.6 $\mu m$                    |
| WFS wavelength  | wfswvl        | 0.5 $\mu m$                    |
| Target distance   | ranget        | 500.0 km, 35780.0 km           |
| $r_0$ at 0.5 $\mu m$                                      | r0            | 7 cm , 10 cm, 15 cm , 50 cm    |
| Tilt correction<br>(1=correct tilt, 0=don't)              | itilt         | 1, 0                           |
| AO (1=use AO, 0=don't)                                    | iest          | 0                              |
| Array length  | arrlen        | 10.0 m                         |
| Wavefront estimator                                       | mvflag        | LS-G, LS-Z, MV-G, MV-Z         |
| nstep   | nstep         | 20                             |
| DM actuator separation<br>grid size                       | actsep        | 0.12                           |
| Elementary function separation<br>grid for pupil estimate | actsep1       | 0.12                           |
| Number of photons<br>per subaperture                      | pchnt         | see $\bar{K}_{WFS}$ in Table 3 |
| Total number of photons                                   | phot          | see $\bar{K}_I$ in Table 3     |
| vt  | vt            | 0                              |
| velx  | velx          | 0                              |
| vely  | vely          | 0                              |
| time delay  | tau           | 0 sec                          |
| Number of Zernike Polynomials                             | nmax          | optimized (see Table 7)        |

Table 12. Simulation Input Parameters.

## *Appendix B. Average Pupil-Averaged Mean Square Residual Phase Error Results*

### *B.1 Introduction*

The pupil-averaged mean square residual phase errors for each of the 128 point source simulations are listed in Tables 13 and 14. Table 13 presents the results for those simulations where tilt was not removed. Table 14 presents the results for the simulation runs where tilt was initially removed.

*B.1.1 Effect of Light Level,  $m_v$ .* In general, the average pupil-averaged mean square residual phase error,  $\langle \varepsilon^2 \rangle$ , decreased with increasing light levels. In other words, the techniques did a better job for stronger signals.

*B.1.2 Effect of Atmospheric Coherence Diameter,  $r_0$ .* In general,  $\langle \varepsilon^2 \rangle$  decreased with increasing  $r_0$ . Thus, each wavefront estimator did a better job estimating the wavefront as the amount of turbulence decreased.

*B.1.3 Effect of Tilt Removal.* A comparison between the two cases where tilt was and was not initially removed shows lower values of  $\langle \varepsilon^2 \rangle$  for the tilt removed cases.

### *B.2 Summary*

The MV-Z technique had the lowest average pupil-averaged mean square residual phase error in 28 out of 32 cases. For four of the cases with the lowest light levels the LS-Z technique performed the best. For all cases the LS-G technique performed the worst. For the highest light levels the performance order (best to worst) was MV-Z, MV-G, LS-Z, and LS-G. For the lowest light levels the two techniques that used Zernike polynomials performed the best. This may be due to the fact that the optimal number of Zernike polynomials was small. This effectively allowed the Zernike

|            |      | $m_v = 0$ | $m_v = 4$ | $m_v = 8$ | $m_v = 12$ |
|------------|------|-----------|-----------|-----------|------------|
| $r_0 = 7$  | LS-G | 2.02549   | 2.05700   | 3.28226   | 43.9141    |
|            | MV-G | 1.18569   | 1.22654   | 2.59223   | 35.6155    |
|            | LS-Z | 1.69045   | 1.71617   | 2.58278   | 18.5421    |
|            | MV-Z | 0.85591   | 0.888756  | 2.02595   | 18.9715    |
| $r_0 = 10$ | LS-G | 1.11816   | 1.14895   | 2.35305   | 42.3190    |
|            | MV-G | 0.65401   | 0.69443   | 1.89593   | 32.0230    |
|            | LS-Z | 0.93329   | 0.957436  | 1.80272   | 16.5274    |
|            | MV-Z | 0.47282   | 0.505280  | 1.46595   | 16.8191    |
| $r_0 = 15$ | LS-G | 0.569276  | 0.594582  | 1.79066   | 41.3545    |
|            | MV-G | 0.333152  | 0.370040  | 1.41978   | 29.2261    |
|            | LS-Z | 0.475210  | 0.498150  | 1.22484   | 15.3112    |
|            | MV-Z | 0.241042  | 0.271690  | 1.09878   | 15.4588    |
| $r_0 = 50$ | LS-G | 0.0772131 | 0.106973  | 1.28568   | 40.4862    |
|            | MV-G | 0.0455972 | 0.071287  | 0.88027   | 21.9982    |
|            | LS-Z | 0.0644468 | 0.0856507 | 0.570486  | 14.2258    |
|            | MV-Z | 0.0331698 | 0.0555765 | 0.564382  | 13.6337    |

Table 13. Average Pupil-Averaged Mean Square Residual Phase Error.

techniques to avoid matching the noisy wavefront structures that are common for low light levels.

|            |      | $m_v = 0$ | $m_v = 4$ | $m_v = 8$ | $m_v = 12$ |
|------------|------|-----------|-----------|-----------|------------|
| $r_0 = 7$  | LS-G | 1.07882   | 1.10528   | 2.06822   | 33.6510    |
|            | MV-G | 0.63962   | 0.87190   | 1.93346   | 25.2551    |
|            | LS-Z | 1.63257   | 1.65035   | 2.21111   | 11.9618    |
|            | MV-Z | 0.60305   | 0.805450  | 1.64071   | 8.80780    |
| $r_0 = 10$ | LS-G | 0.595719  | 0.621081  | 1.56426   | 32.6166    |
|            | MV-G | 0.462366  | 0.495416  | 1.40304   | 22.0613    |
|            | LS-Z | 0.901252  | 0.917667  | 1.46250   | 6.85700    |
|            | MV-Z | 0.424269  | 0.459196  | 1.14919   | 6.90584    |
| $r_0 = 15$ | LS-G | 0.303444  | 0.328003  | 1.25836   | 31.9783    |
|            | MV-G | 0.235555  | 0.226513  | 1.02919   | 19.5102    |
|            | LS-Z | 0.458809  | 0.474153  | 0.93257   | 5.78939    |
|            | MV-Z | 0.216315  | 0.247679  | 0.806749  | 5.70092    |
| $r_0 = 50$ | LS-G | 0.0413676 | 0.0648327 | 0.981364  | 31.3956    |
|            | MV-G | 0.0323234 | 0.0509922 | 0.583113  | 12.6586    |
|            | LS-Z | 0.0620710 | 0.0758428 | 0.282235  | 4.83066    |
|            | MV-Z | 0.0297627 | 0.0488851 | 0.276042  | 4.17243    |

Table 14. Average Pupil-Averaged Mean Square Residual Phase Error (tilt corrected).

## *Appendix C. Average System Transfer Function Results*

### *C.1 Introduction*

The results of the Average system transfer function for each wavefront estimation technique are presented in Figures 31 through 38.

*C.1.1 Effect of Light Level,  $m_v$ .* In general, the Average OTF for all techniques decreased as the light level decreased. Also, the largest spread in the performance results of the different estimation techniques occurred for the lowest light levels. The two techniques that use Zernike polynomial elementary functions stand apart from the two techniques that use Gaussian elementary functions for the case when  $m_v = 12$ . This is probably due to the fact that the optimal number of Zernike polynomials was small. The wavefront estimate using such a small number of polynomials essentially bypassed the need to match the high noise levels in the original wavefront.

*C.1.2 Effect of Atmospheric Coherence Diameter,  $r_0$ .* The results of each technique converge as the atmosphere becomes less turbulent (increasing  $r_0$ ). The system transfer function generally lowers and collapses at low spatial frequencies as the level of turbulence increases.

*C.1.3 Effect of Tilt Removal.* A couple of things happen when tilt is removed prior to wavefront estimation. The average system transfer function improves, and the results of the different wavefront estimation techniques converge.

### *C.2 Summary*

The MV-Z estimation technique matched or out-performed all other techniques.



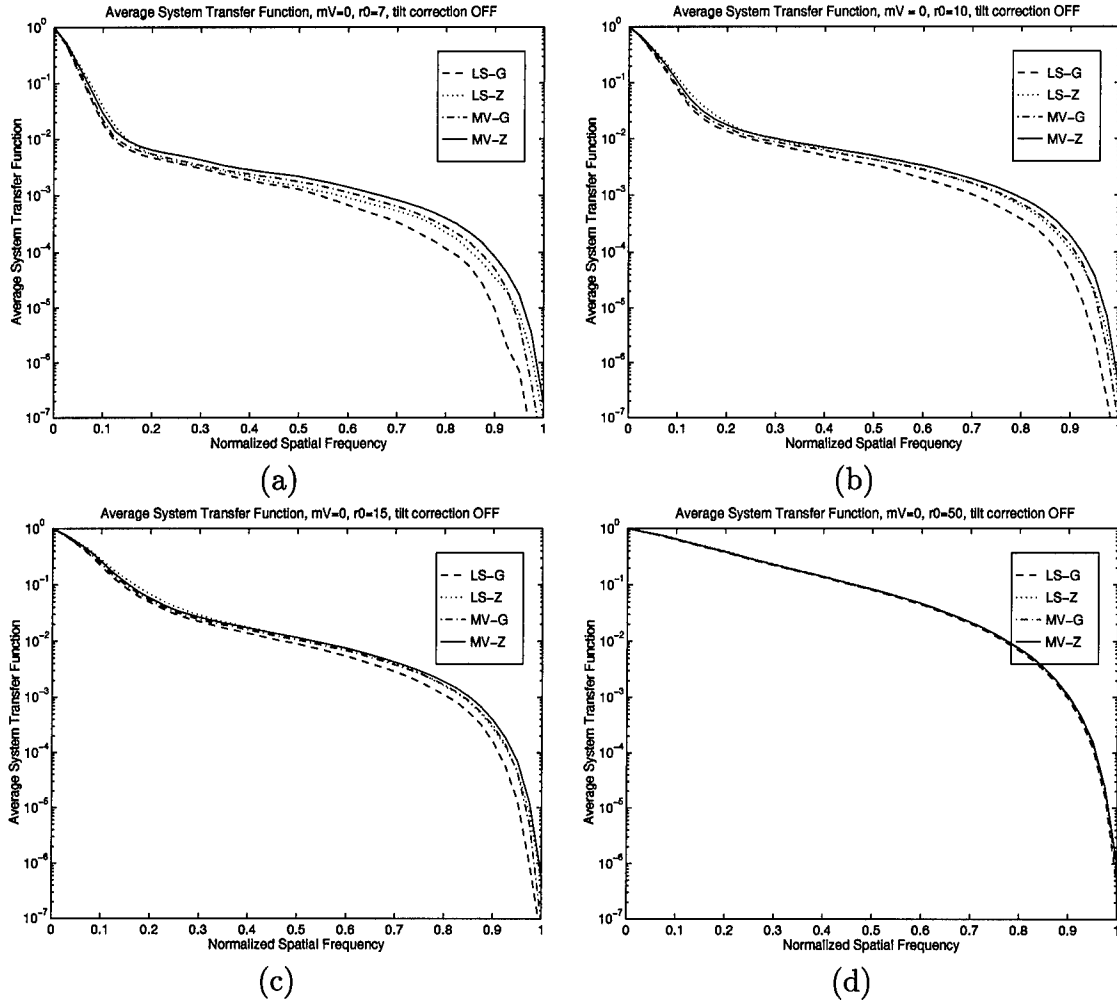


Figure 31. Average System Transfer Function for  $m_v = 0$ : (a)  $r_0=7$  cm, (b)  $r_0=10$  cm, (c)  $r_0=15$  cm, (d)  $r_0=50$  cm.

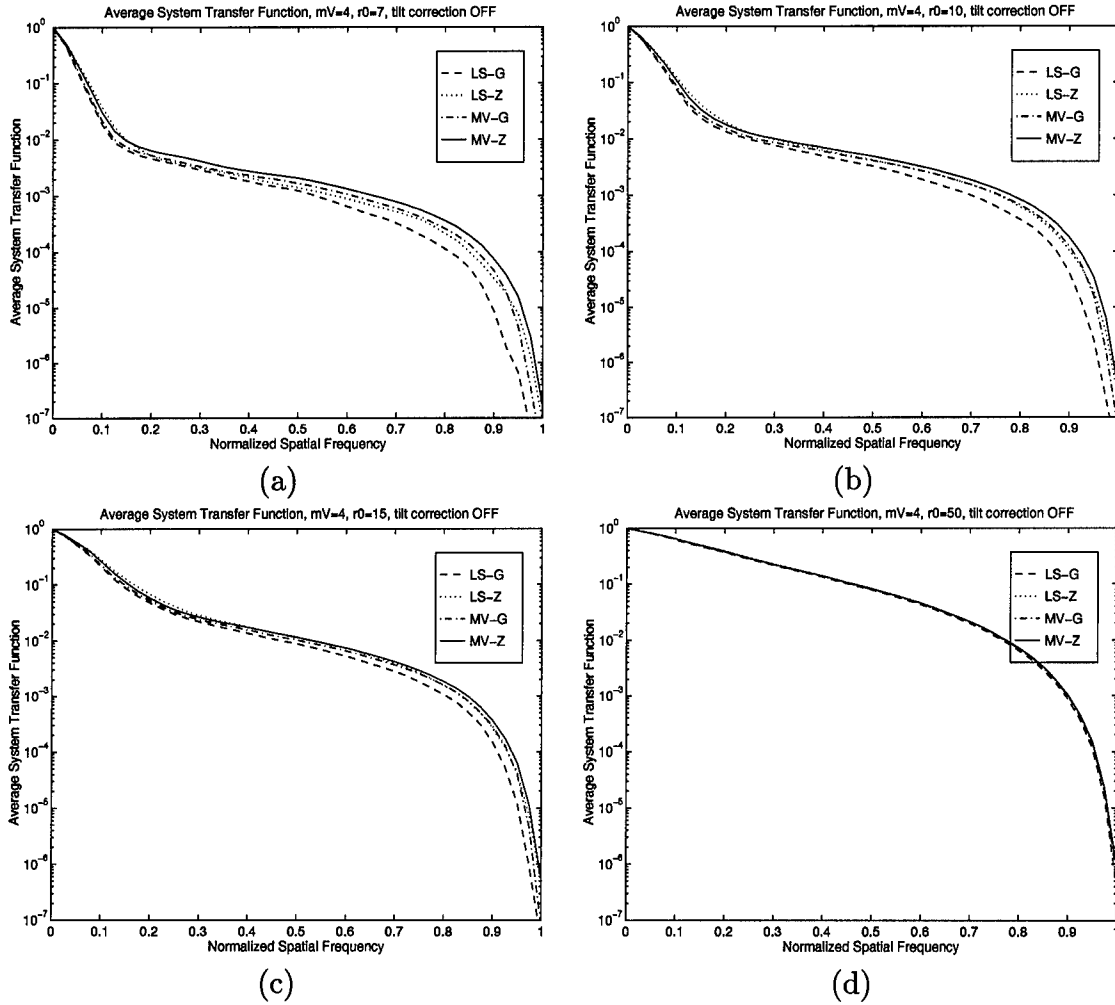


Figure 32. Average System Transfer Function for  $m_v = 4$ : (a)  $r_0 = 7$  cm, (b)  $r_0 = 10$  cm, (c)  $r_0 = 15$  cm, (d)  $r_0 = 50$  cm.

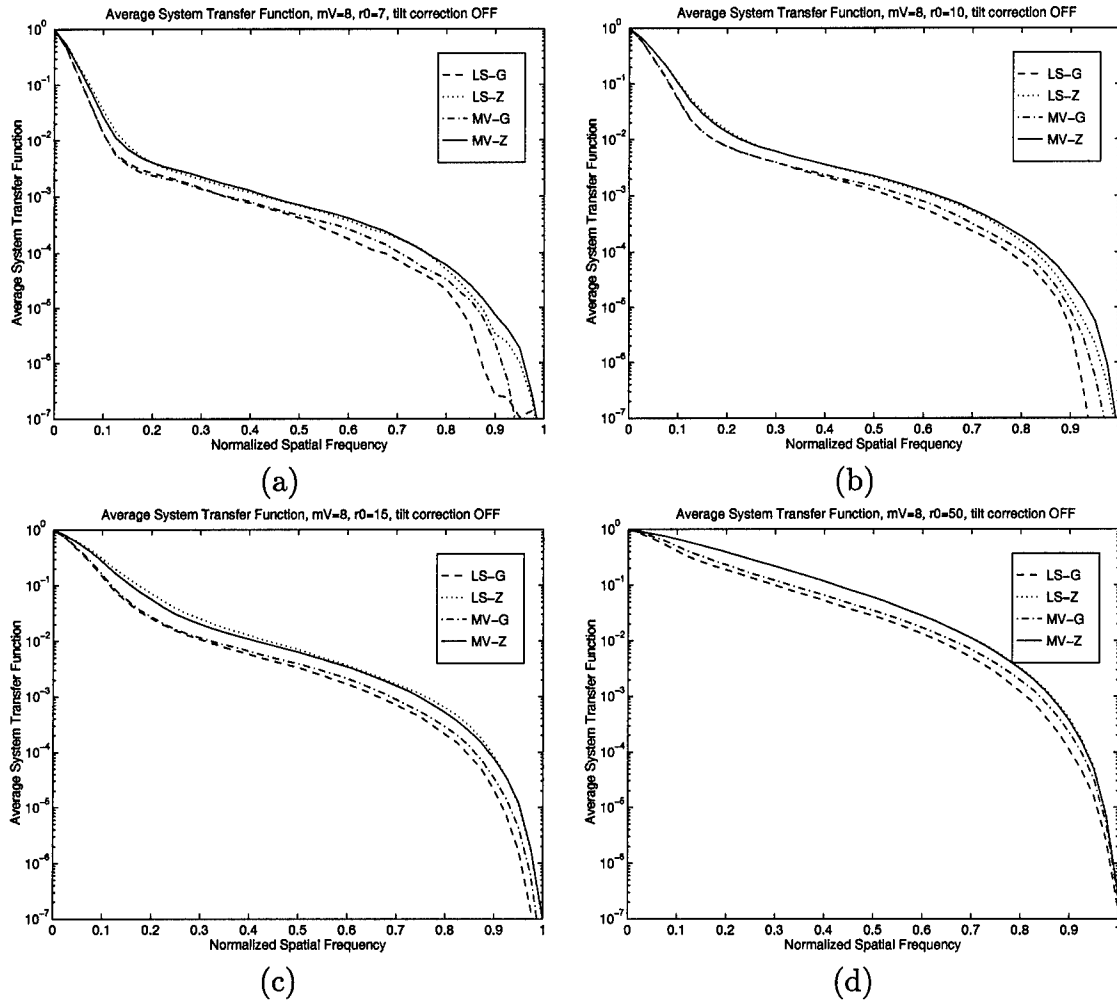


Figure 33. Average System Transfer Function for  $m_v = 8$ : (a)  $r_0=7$  cm, (b)  $r_0=10$  cm, (c)  $r_0=15$  cm, (d)  $r_0=50$  cm.

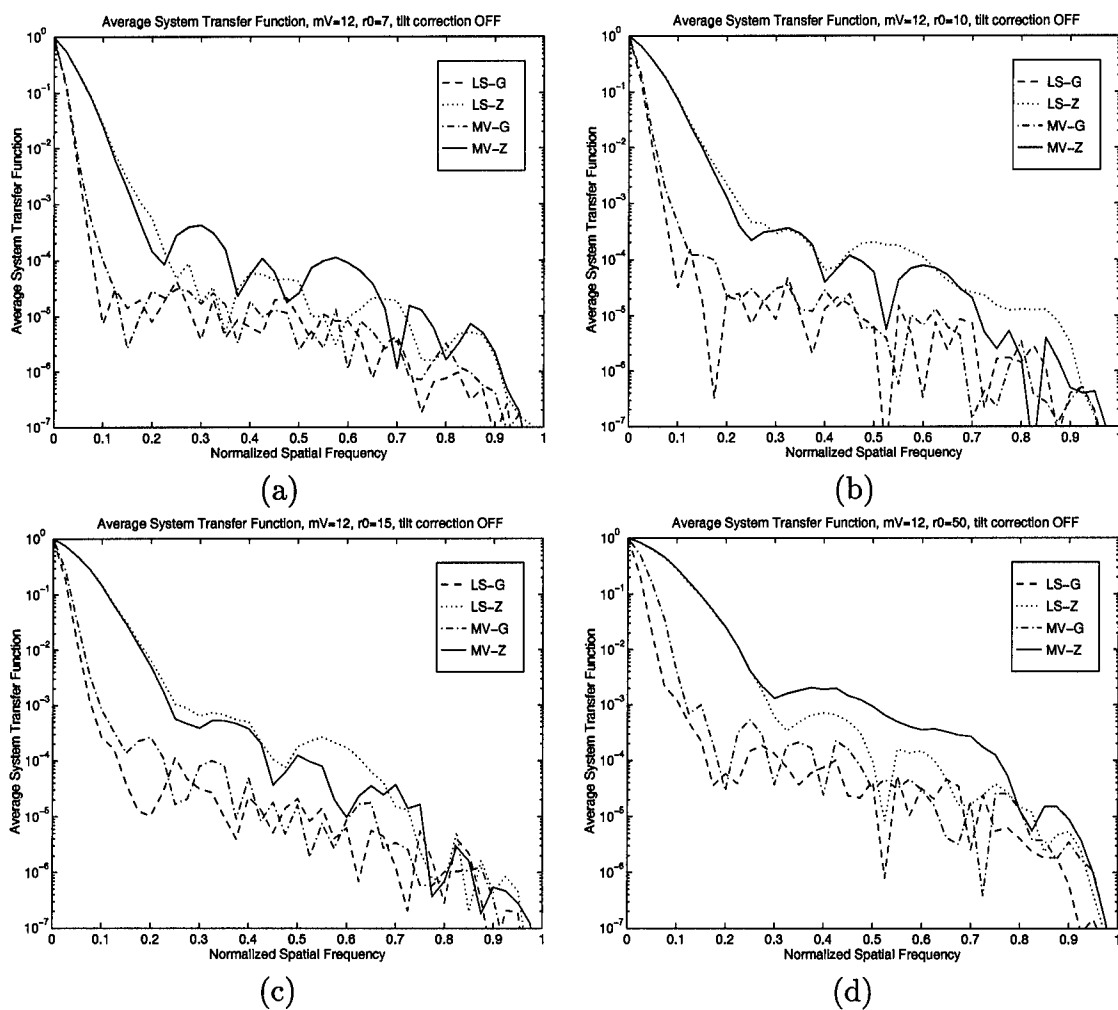


Figure 34. Average System Transfer Function for  $m_v = 12$ : (a)  $r_0=7$  cm, (b)  $r_0=10$  cm, (c)  $r_0=15$  cm, (d)  $r_0=50$  cm.

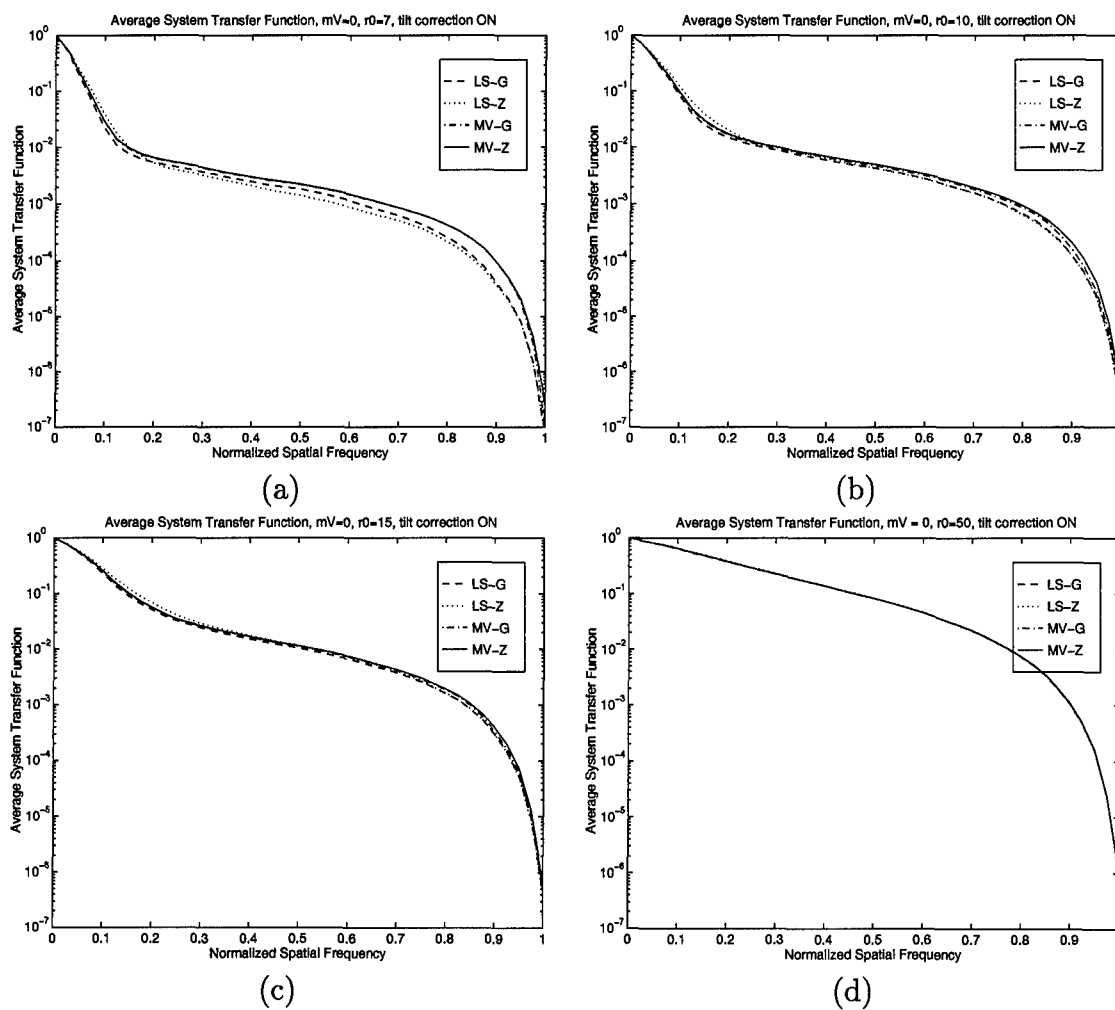


Figure 35. Average System Transfer Function for  $m_v = 0$  (tilt corrected): (a)  $r_0=7$  cm, (b)  $r_0=10$  cm, (c)  $r_0=15$  cm, (d)  $r_0=50$  cm.

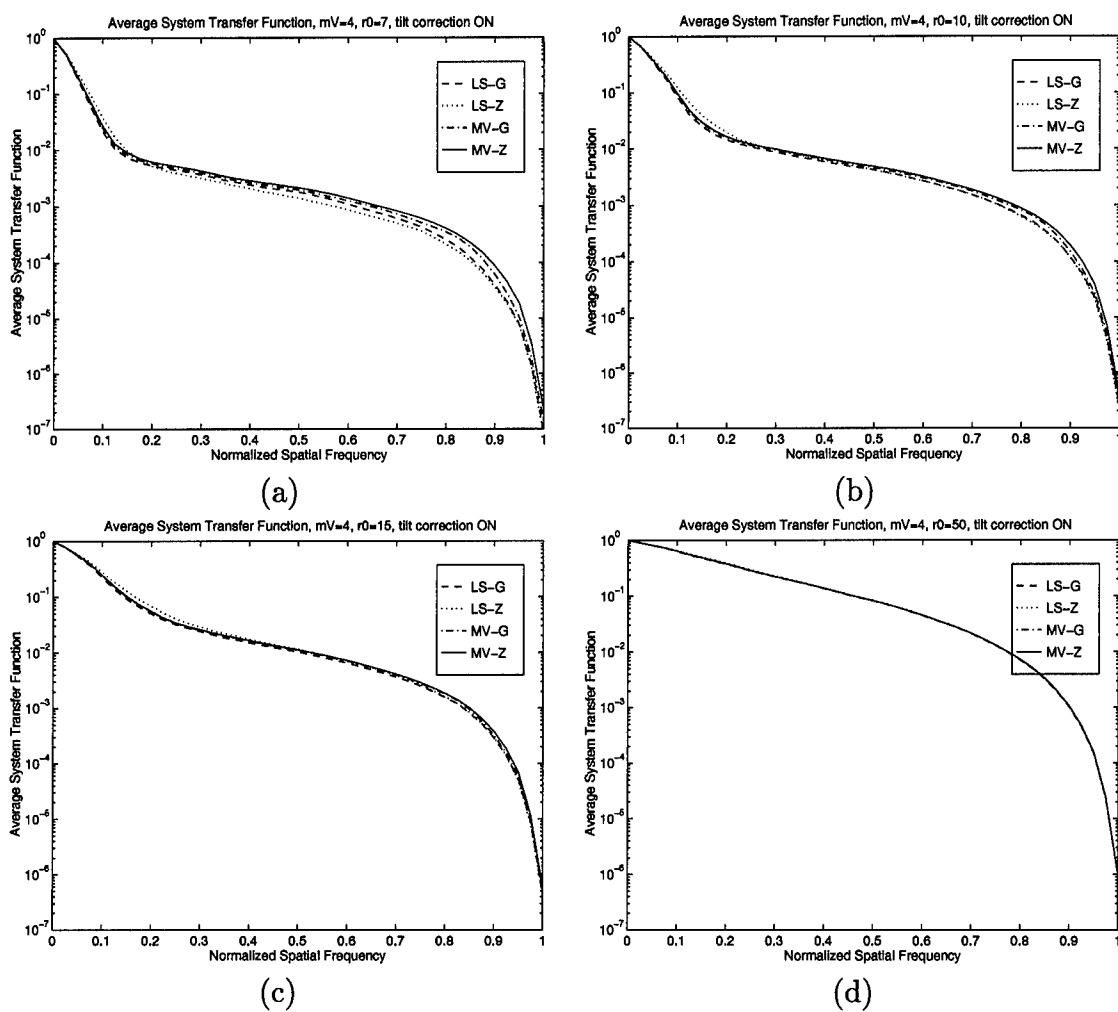


Figure 36. Average System Transfer Function for  $m_v = 4$  (tilt corrected): (a)  $r_0 = 7$  cm, (b)  $r_0 = 10$  cm, (c)  $r_0 = 15$  cm, (d)  $r_0 = 50$  cm.

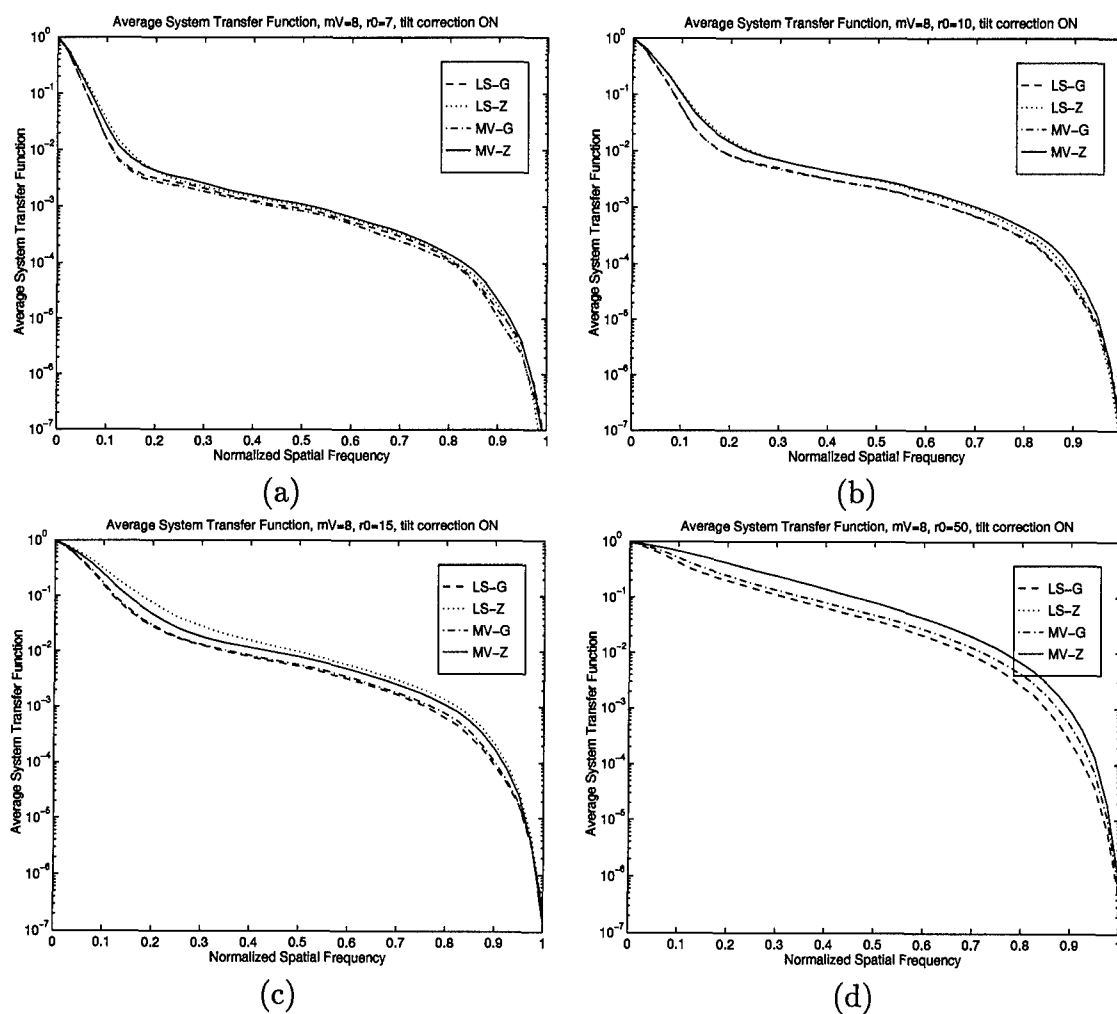


Figure 37. Average System Transfer Function for  $m_v = 8$  (tilt corrected): (a)  $r_0=7$  cm, (b)  $r_0=10$  cm, (c)  $r_0=15$  cm, (d)  $r_0=50$  cm.

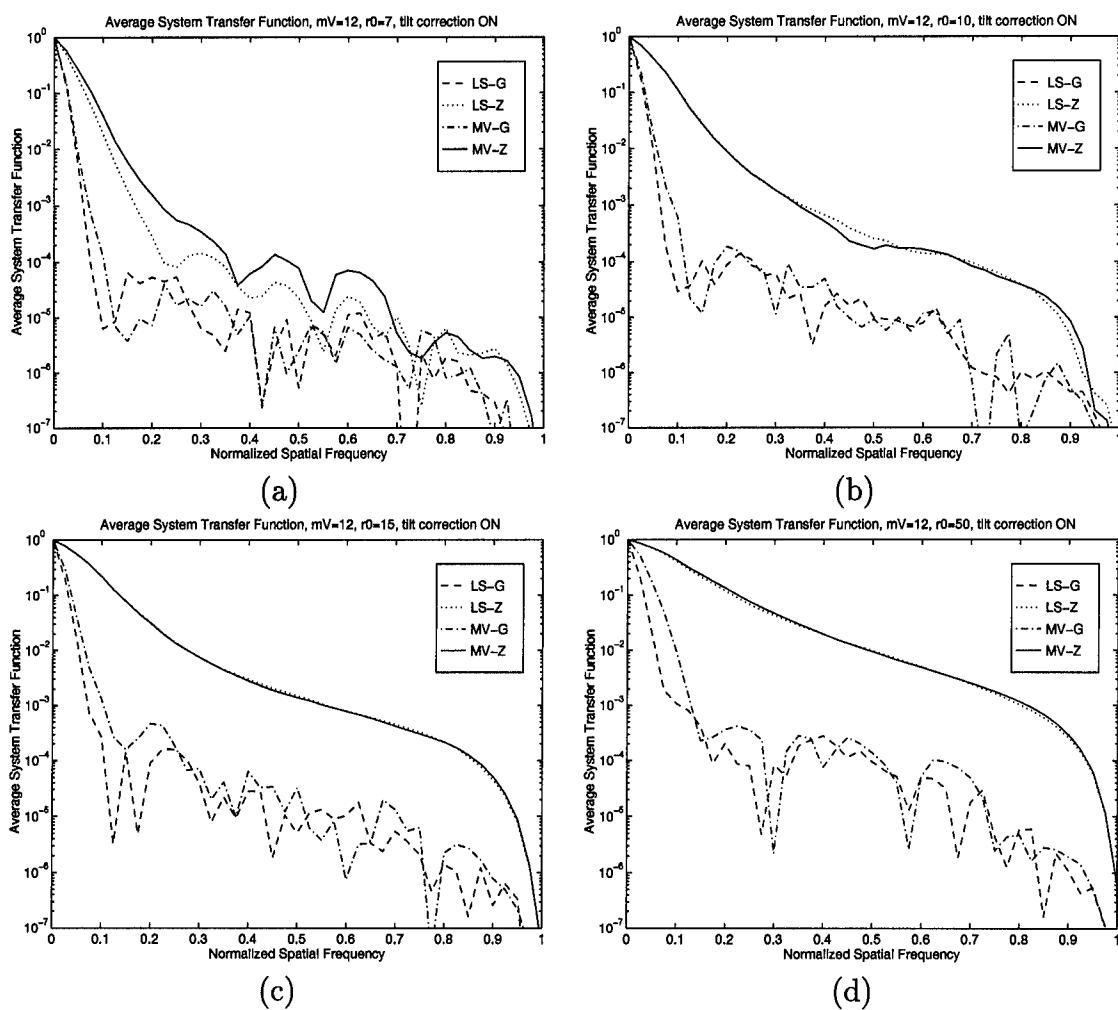


Figure 38. Average System Transfer Function for  $m_v = 12$  (tilt corrected): (a)  $r_0 = 7$  cm, (b)  $r_0 = 10$  cm, (c)  $r_0 = 15$  cm, (d)  $r_0 = 50$  cm.



## *Appendix D. System Transfer Function SNR Results*

### *D.1 Introduction*

The results of the signal-to-noise ratio of the system transfer function for each wavefront estimation technique are presented in Figures 39 through 46.

*D.1.1 Effect of Light Level,  $m_v$ .* In general, the system transfer function SNR decreased as the light level decreased. Also, the largest spread in the performance results of the different estimators occurred for the lowest light levels. Again the effect of the small number of Zernike polynomials is noted. It results in boost for the smallest spatial frequencies and a drop in the highest frequencies.

*D.1.2 Effect of Atmospheric Coherence Diameter,  $r_0$ .* The results of the various techniques converge as the value of  $r_0$  increases. In general, the system transfer function SNR improves as the value of  $r_0$  increases.

*D.1.3 Effect of Tilt Removal.* When tilt is removed prior to wavefront estimation, the system transfer function SNR improves slightly and the different wavefront estimation techniques converge.

### *D.2 Summary*

The minimum variance technique with Zernike polynomial elementary functions generally had higher system transfer function SNR than other techniques. This was particularly apparent for the three highest light levels where the largest improvements in system transfer function SNR occurred for the highest spatial frequencies.

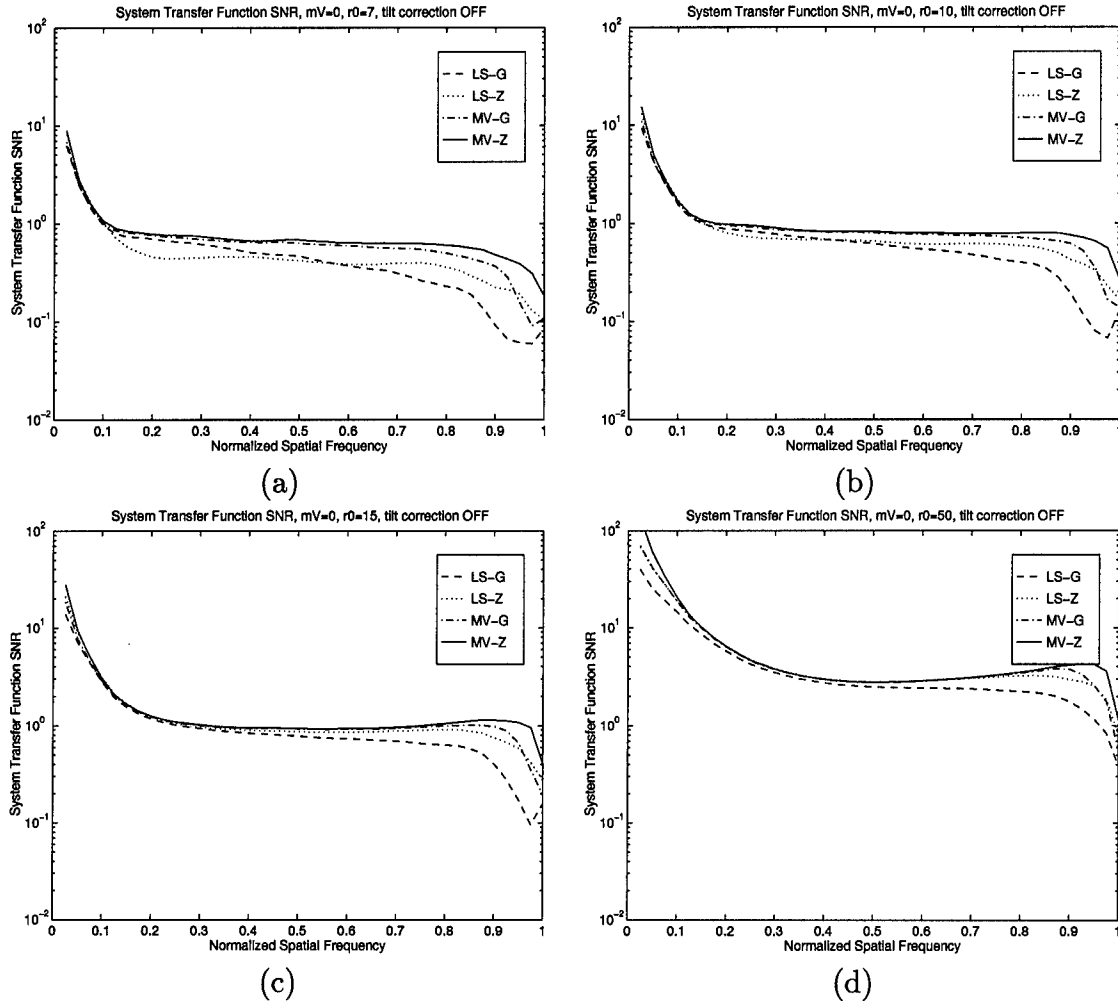


Figure 39. SNR of System Transfer Function for  $m_v = 0$ : (a)  $r_0=7$  cm, (b)  $r_0=10$  cm, (c)  $r_0=15$  cm, (d)  $r_0=50$  cm.

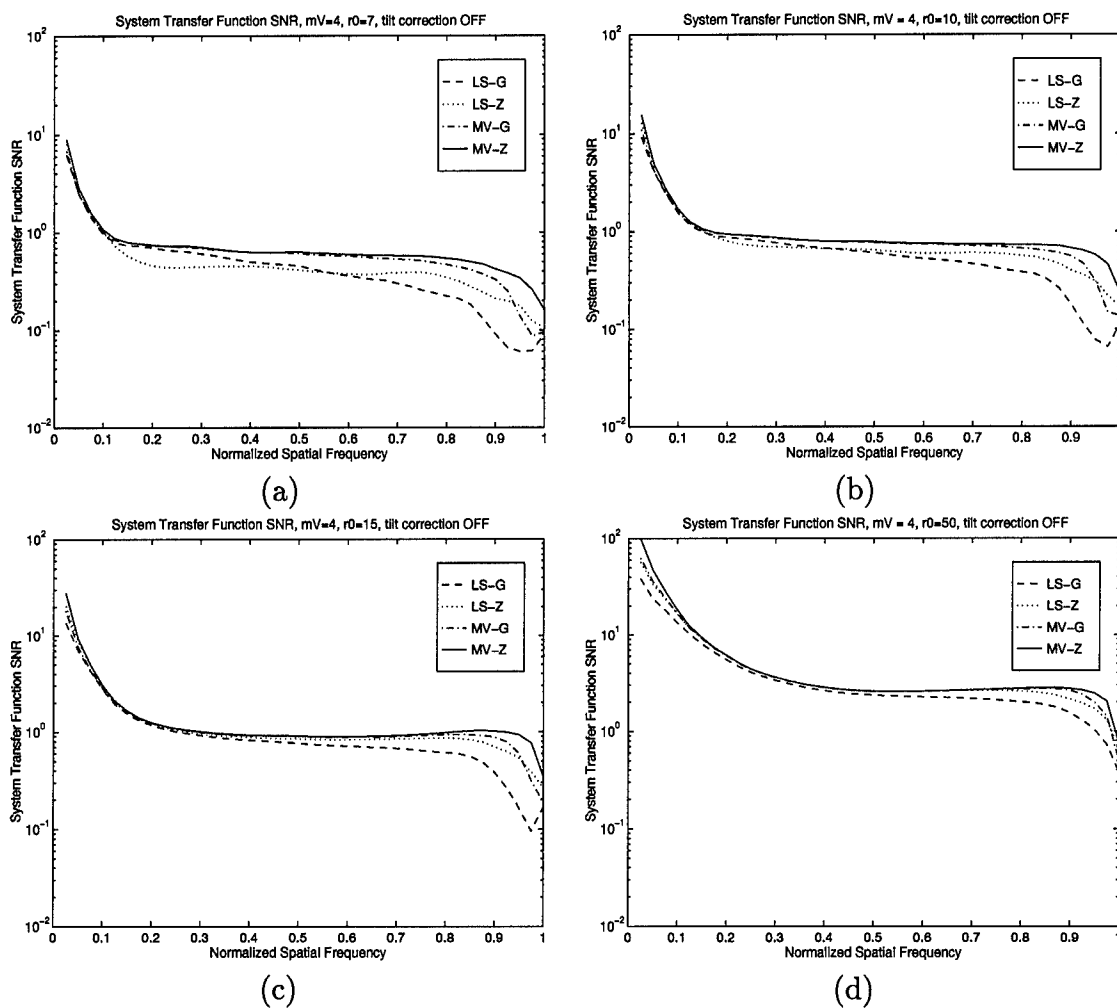


Figure 40. SNR of System Transfer Function for  $m_v = 4$ : (a)  $r_0=7$  cm, (b)  $r_0=10$  cm, (c)  $r_0=15$  cm, (d)  $r_0=50$  cm.

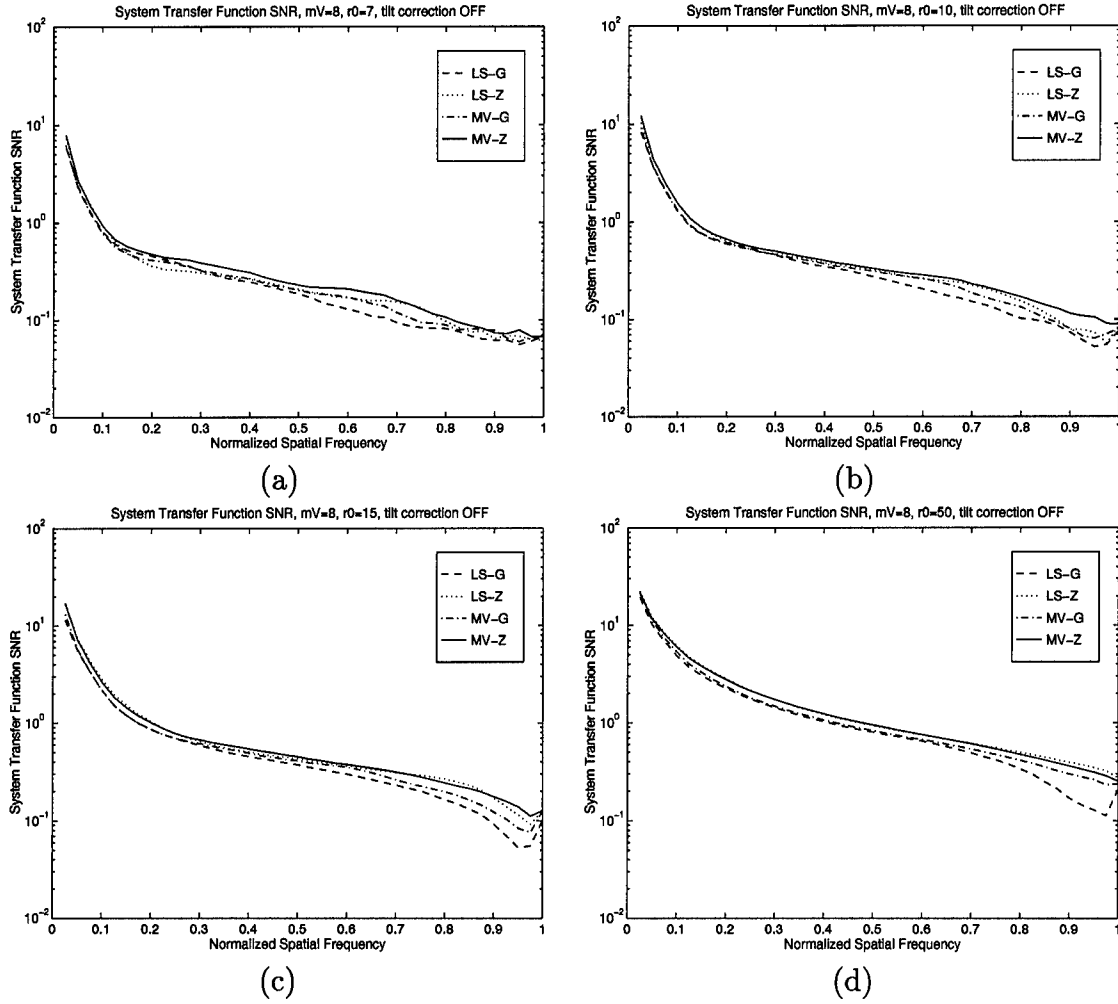


Figure 41. SNR of System Transfer Function for  $m_v = 8$ : (a)  $r_0=7$  cm, (b)  $r_0=10$  cm, (c)  $r_0=15$  cm, (d)  $r_0=50$  cm.

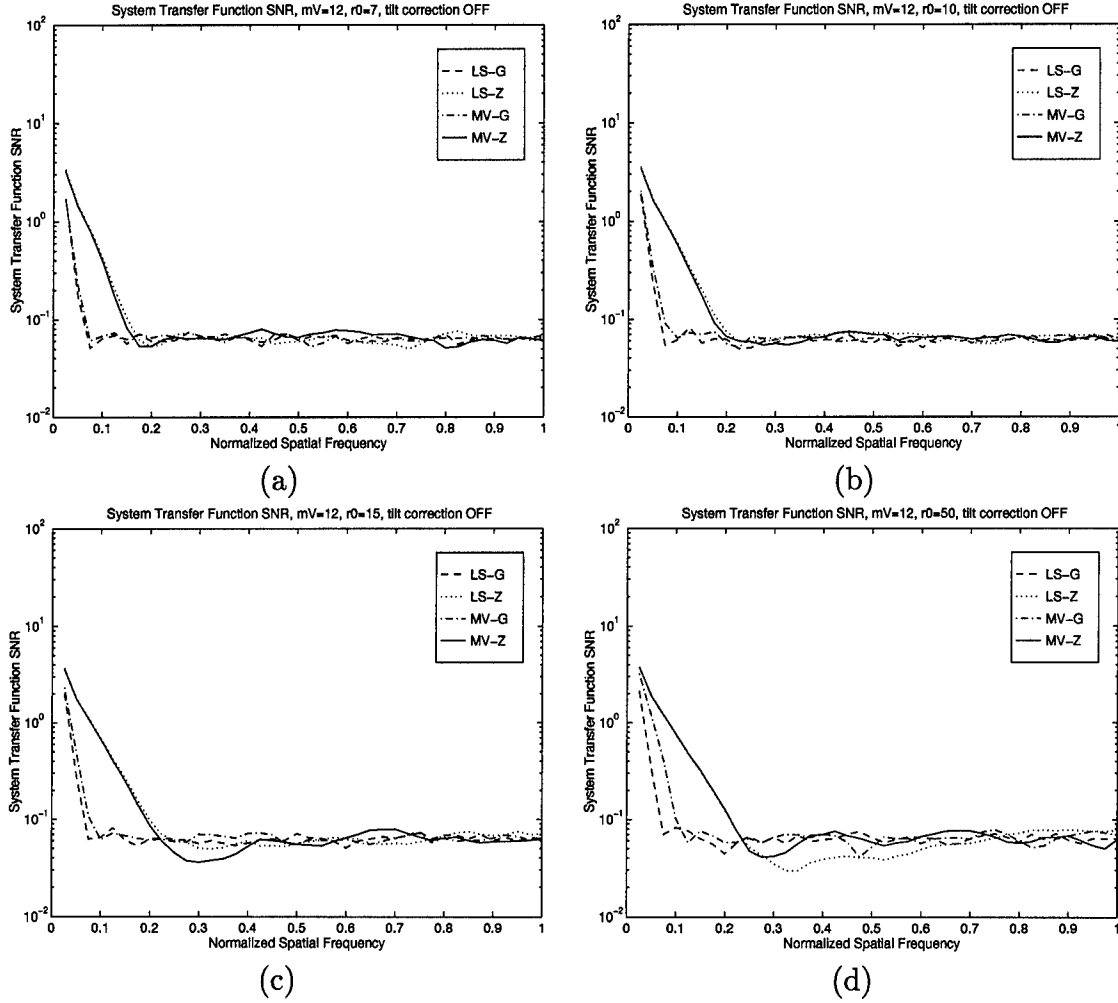


Figure 42. SNR of System Transfer Function for  $m_v = 12$ : (a)  $r_0=7$  cm, (b)  $r_0=10$  cm, (c)  $r_0=15$  cm, (d)  $r_0=50$  cm.

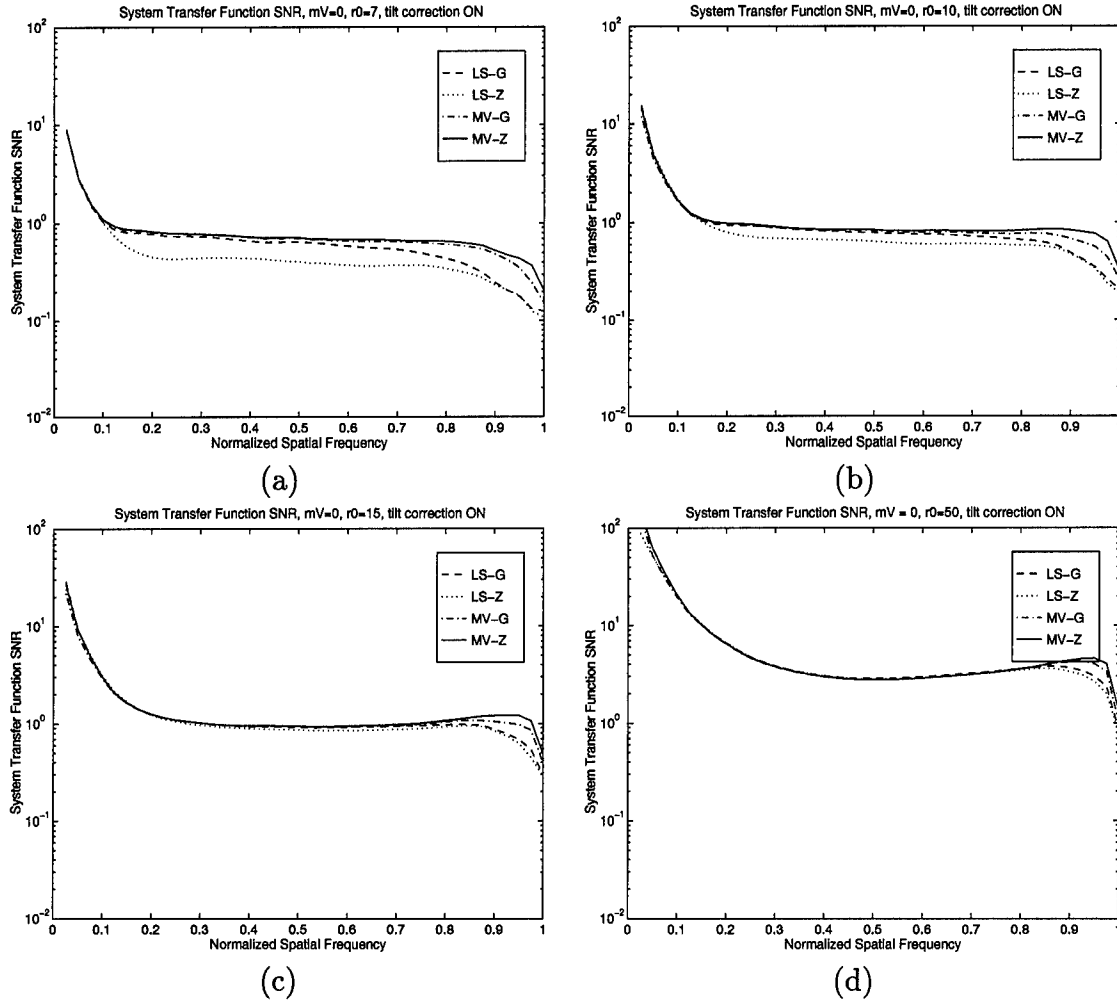


Figure 43. SNR of System Transfer Function for  $m_v = 0$  (tilt corrected): (a)  $r_0=7$  cm, (b)  $r_0=10$  cm, (c)  $r_0=15$  cm, (d)  $r_0=50$  cm.

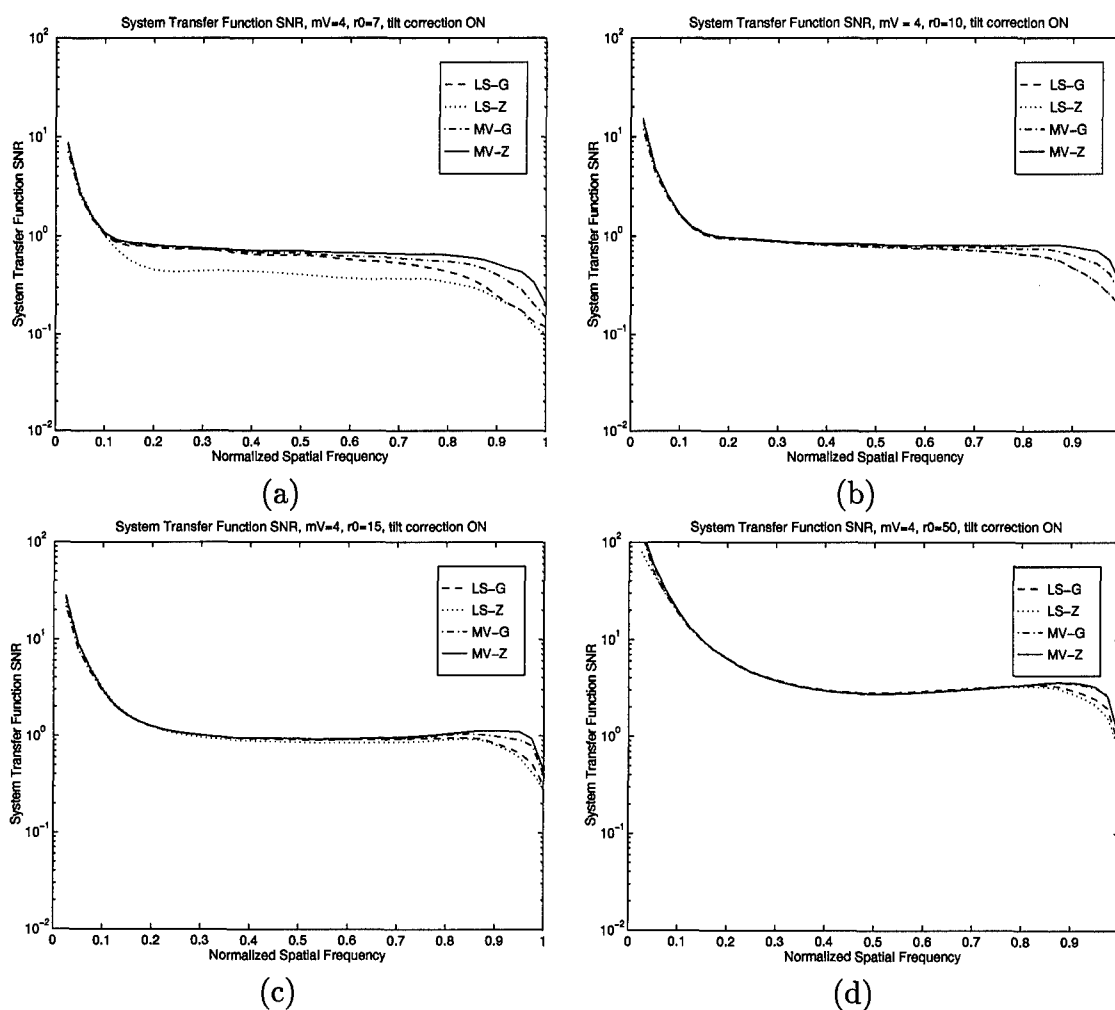


Figure 44. SNR of System Transfer Function for  $m_v = 4$  (tilt corrected): (a)  $r_0=7$  cm, (b)  $r_0=10$  cm, (c)  $r_0=15$  cm, (d)  $r_0=50$  cm.

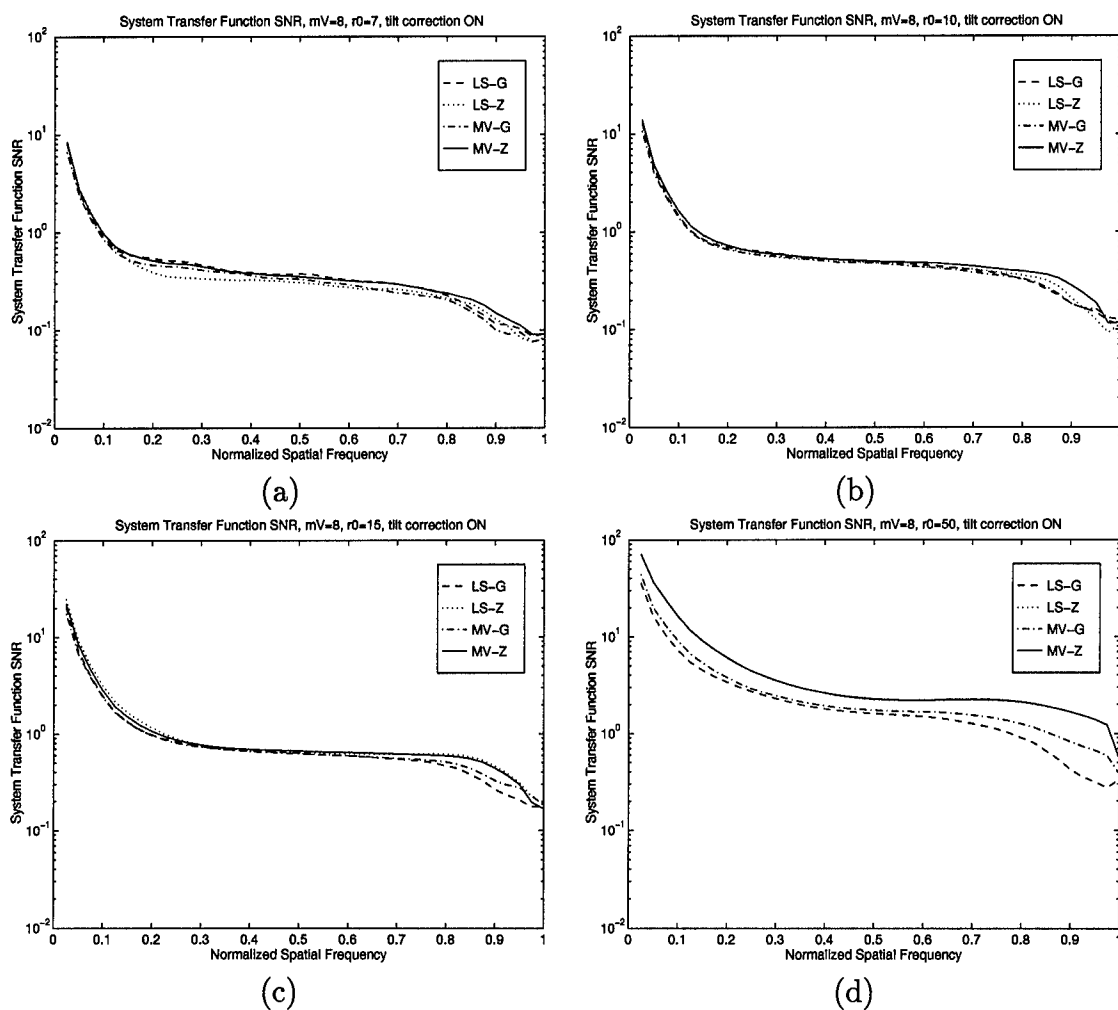


Figure 45. SNR of System Transfer Function for  $m_v = 8$  (tilt corrected): (a)  $r_0=7$  cm, (b)  $r_0=10$  cm, (c)  $r_0=15$  cm, (d)  $r_0=50$  cm.



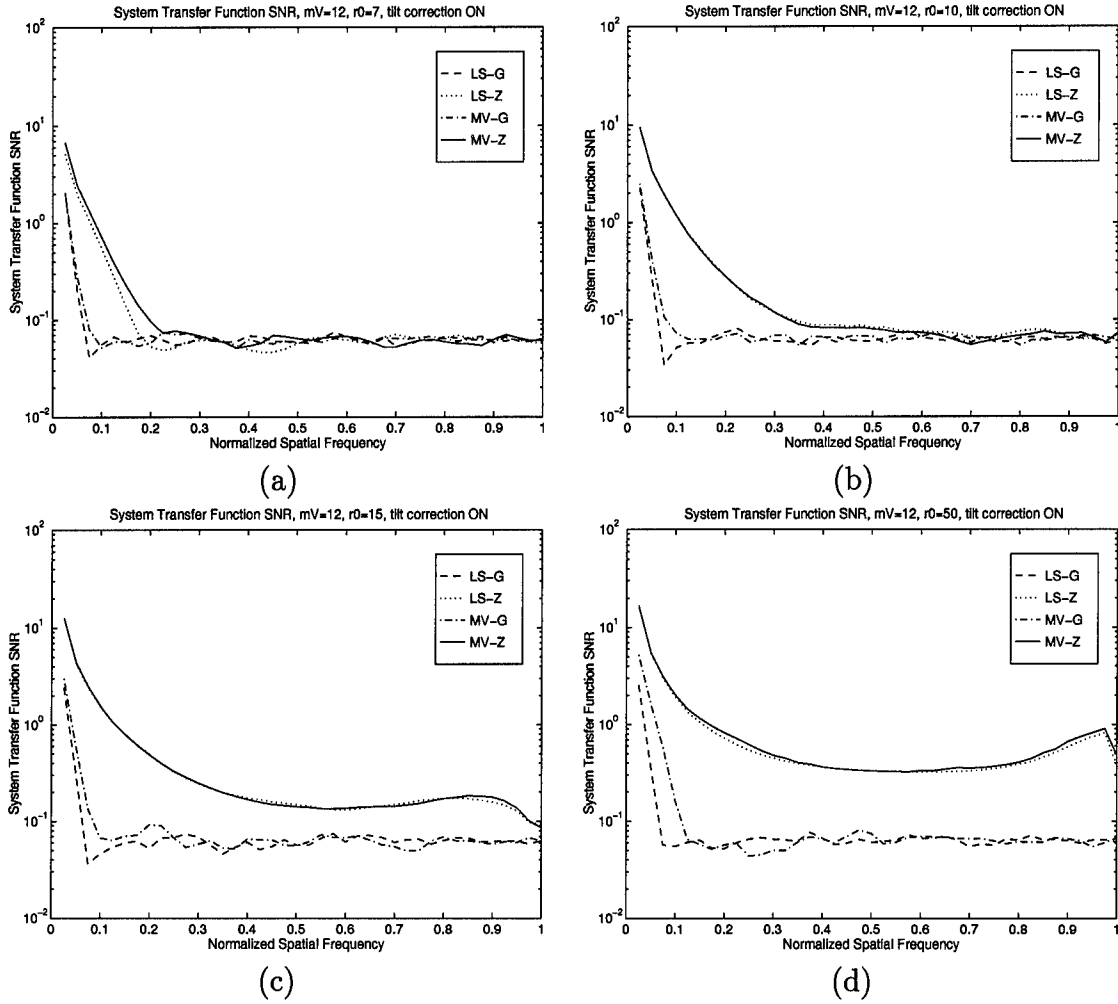


Figure 46. SNR of System Transfer Function for  $m_v = 12$  (tilt corrected): (a)  $r_0=7$  cm, (b)  $r_0=10$  cm, (c)  $r_0=15$  cm, (d)  $r_0=50$  cm.

## *Appendix E. OTF Correlation Results*

### *E.1 Introduction*

The results of the Average OTF correlation for each wavefront estimation technique are presented in Figures 47 through 54.

*E.1.1 Effect of Light Level,  $m_v$ .* The largest spread in the performance results of the different estimators occurred for the highest light levels ( $m_v = 0, 4, 8$ ). In general the OTF correlation decreased for decreasing light levels.

*E.1.2 Effect of Atmospheric Coherence Diameter,  $r_0$ .* The results of the different techniques converge as the level of  $r_0$  increases. In general, the OTF correlation improved for increasing values of  $r_0$ .

*E.1.3 Effect of Tilt Removal.* When tilt is removed prior to wavefront estimation the OTF correlation improves and the results of the different wavefront estimation techniques converge.

### *E.2 Summary*

In general, the MV-Z technique had the best OTF correlation. For the highest light levels this was most pronounced for the highest spatial frequencies.

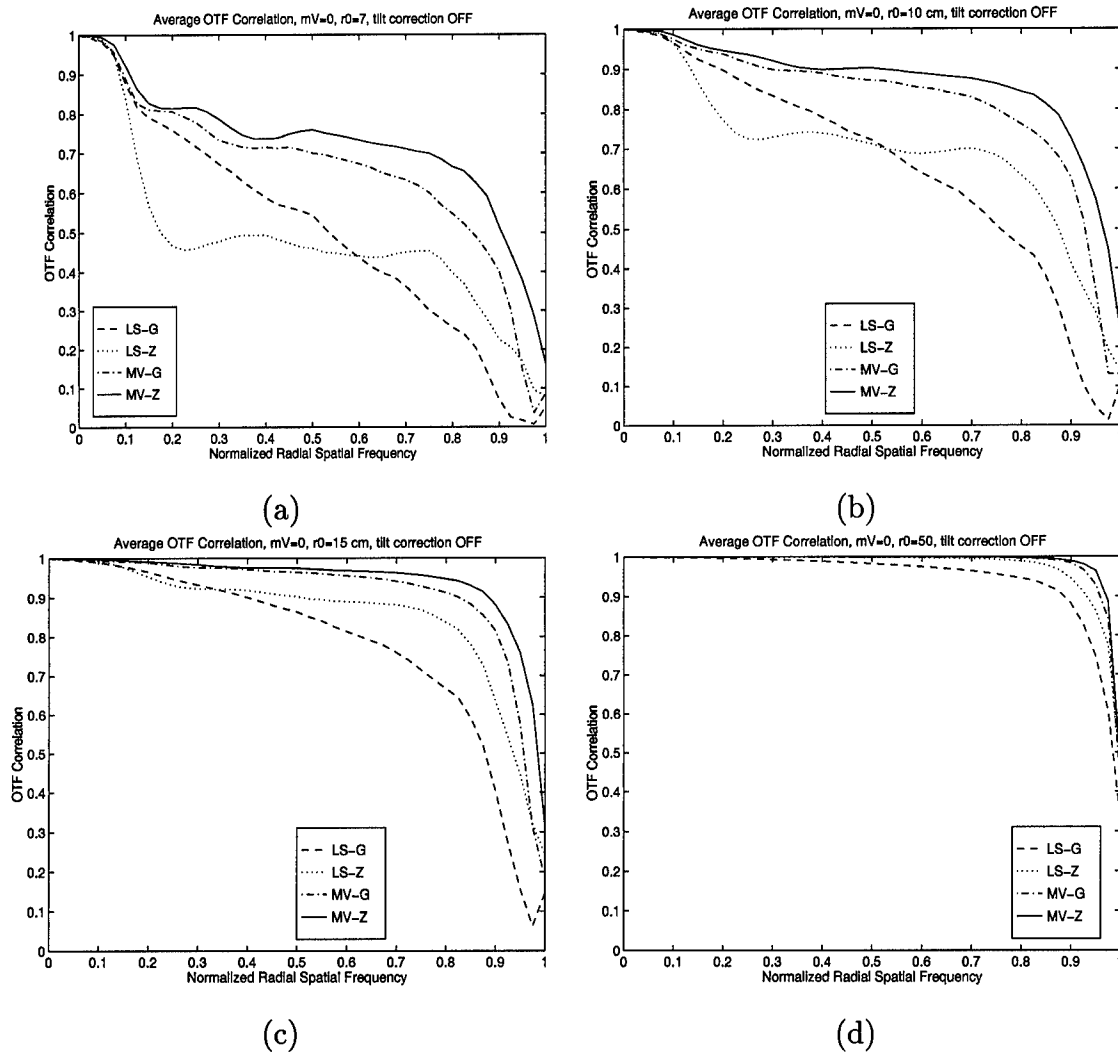


Figure 47. OTF Correlation for  $m_v = 0$ : (a)  $r_0=7$  cm, (b)  $r_0=10$  cm, (c)  $r_0=15$  cm, (d)  $r_0=50$  cm.

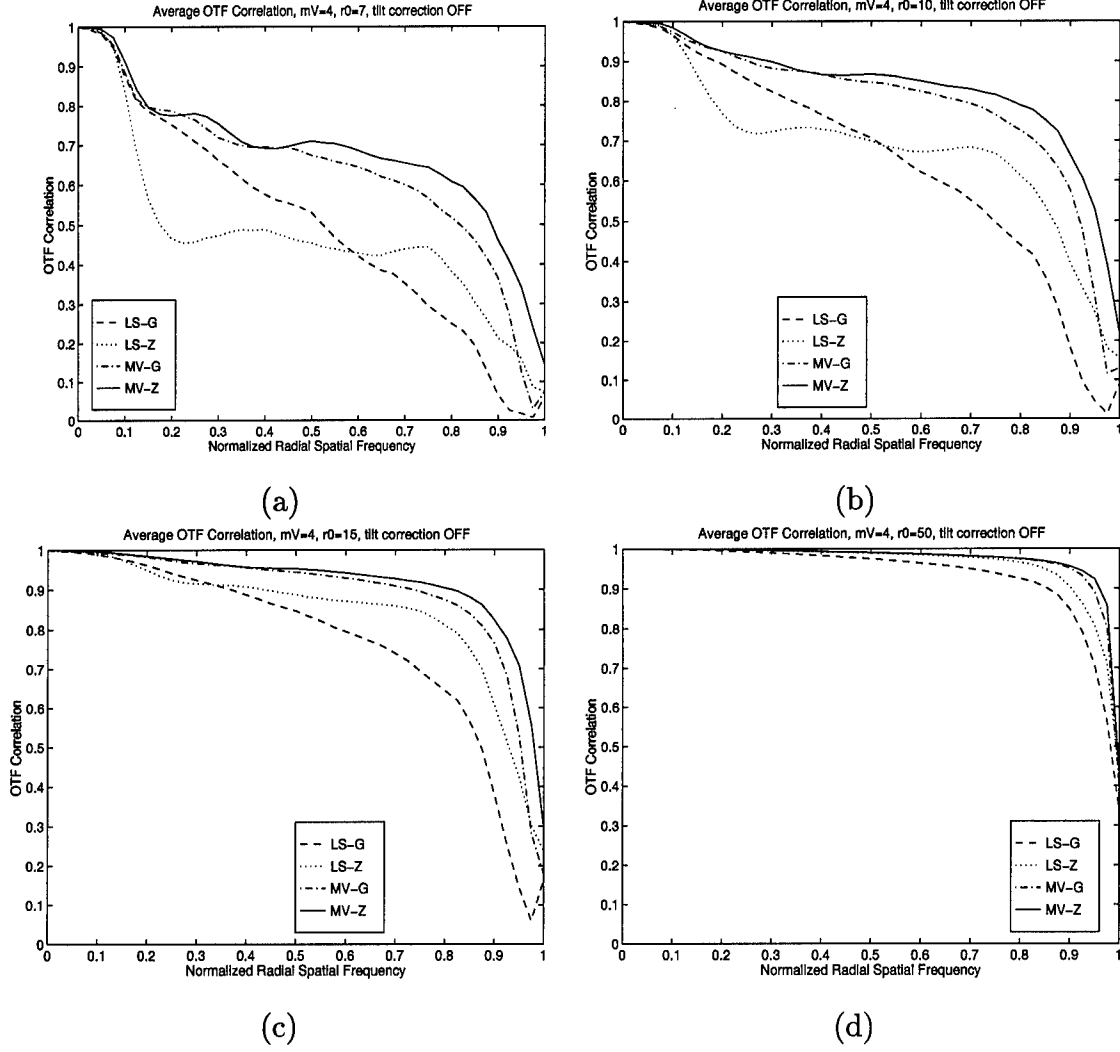


Figure 48. OTF Correlation for  $m_v = 4$ : (a)  $r_0=7$  cm, (b)  $r_0=10$  cm, (c)  $r_0=15$  cm, (d)  $r_0=50$  cm.

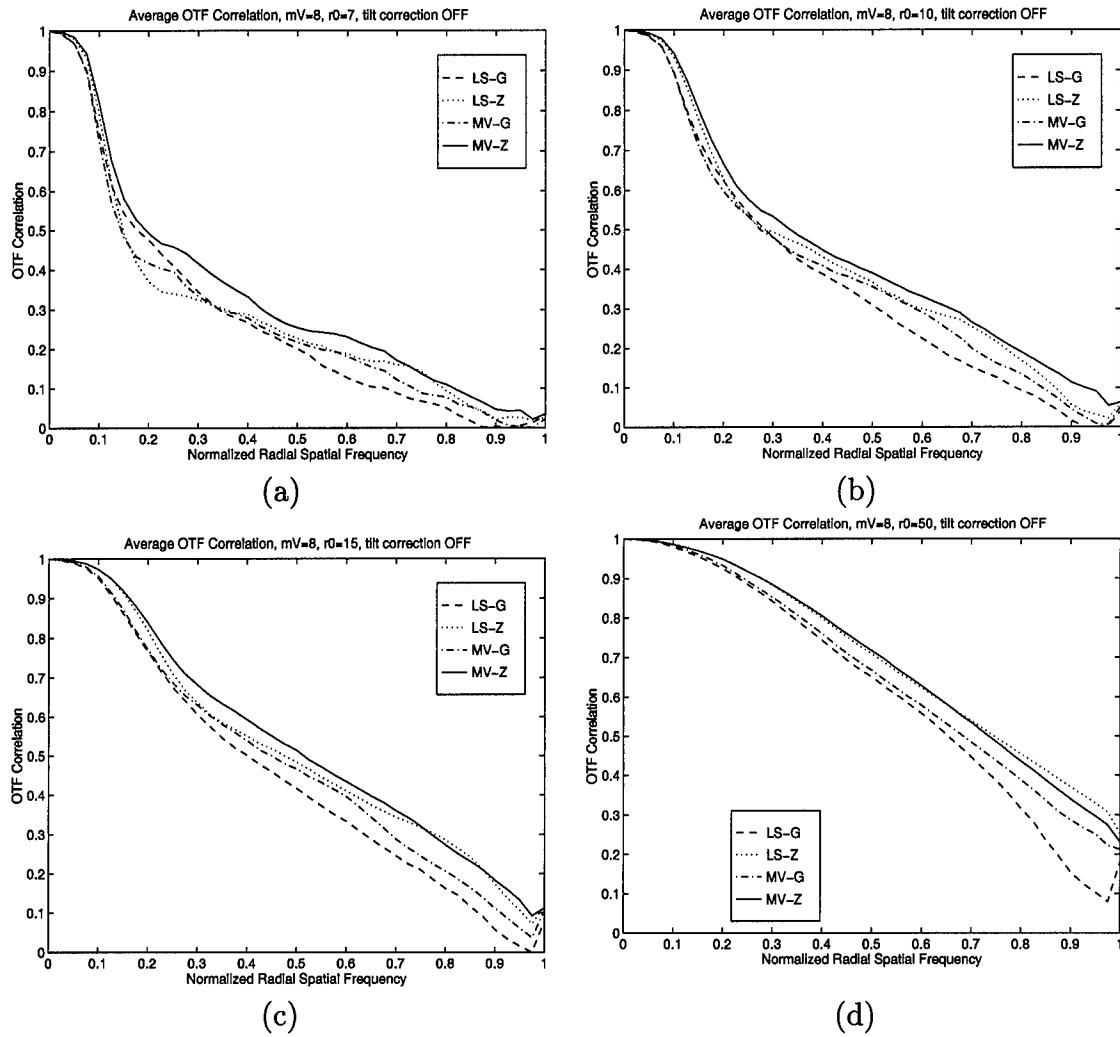


Figure 49. OTF Correlation for  $m_v = 8$ : (a)  $r_0 = 7$  cm, (b)  $r_0 = 10$  cm, (c)  $r_0 = 15$  cm, (d)  $r_0 = 50$  cm.

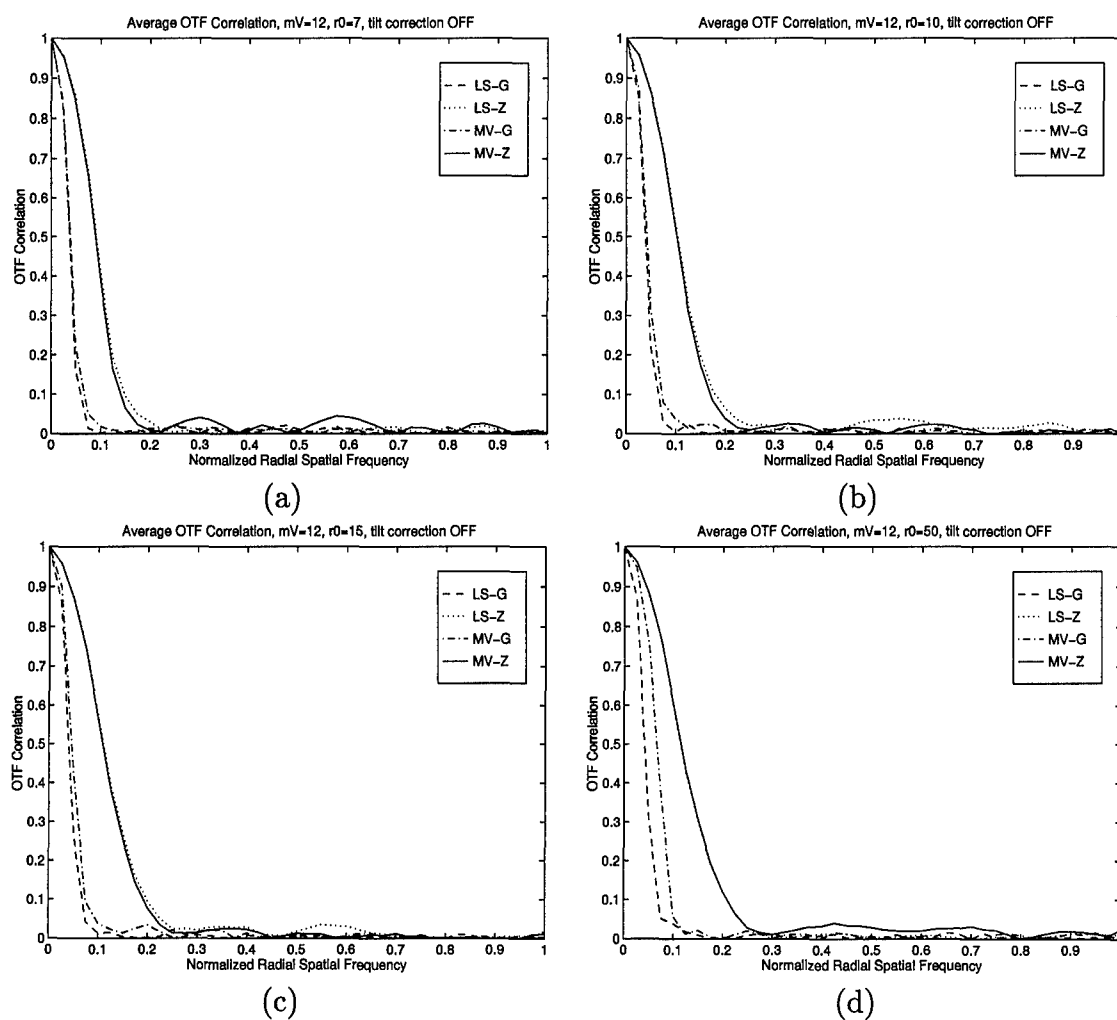


Figure 50. OTF Correlation for  $m_v = 12$ : (a)  $r_0=7$  cm, (b)  $r_0=10$  cm, (c)  $r_0=15$  cm, (d)  $r_0=50$  cm.

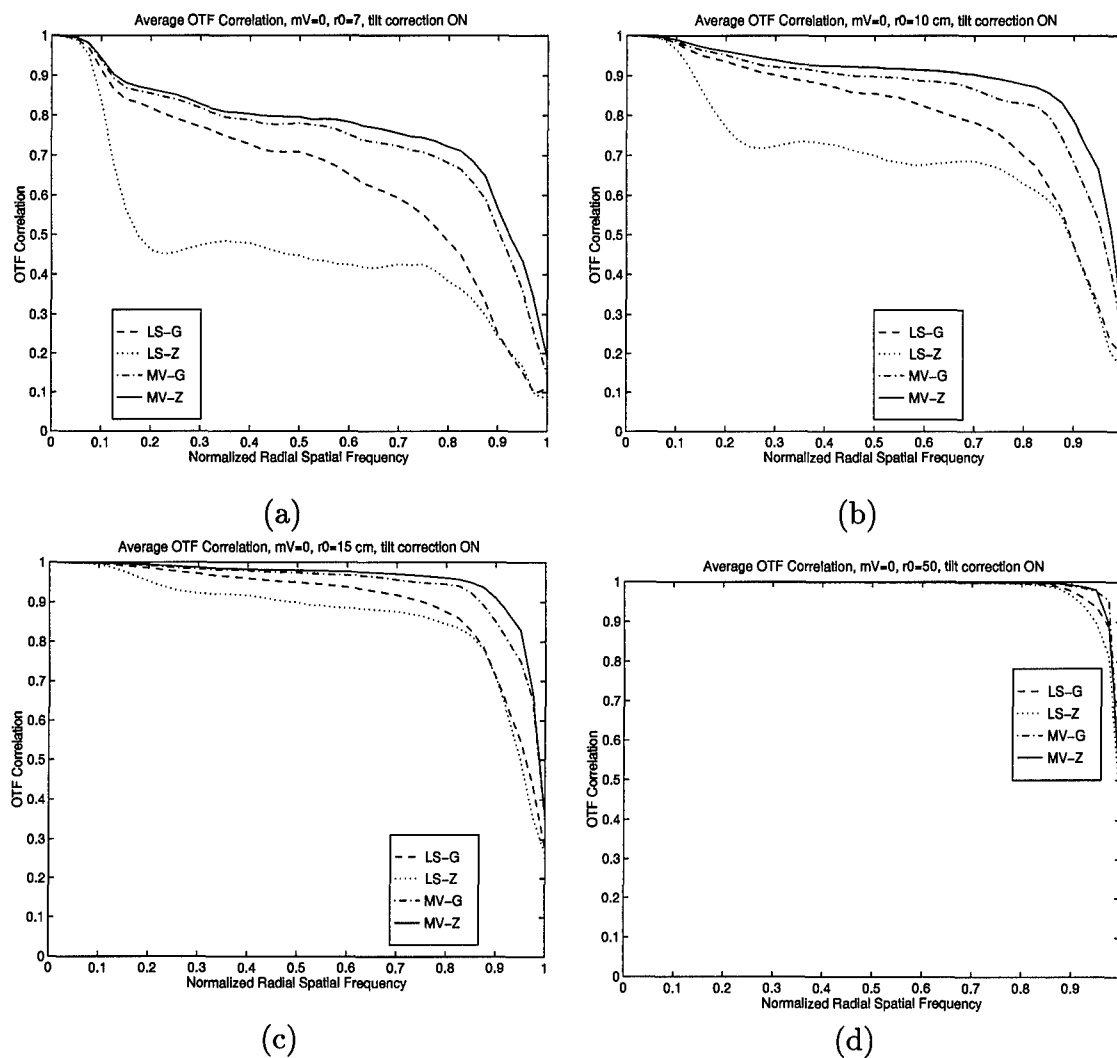


Figure 51. OTF Correlation for  $m_v = 0$  (tilt corrected): (a)  $r_0=7$  cm, (b)  $r_0=10$  cm, (c)  $r_0=15$  cm, (d)  $r_0=50$  cm.

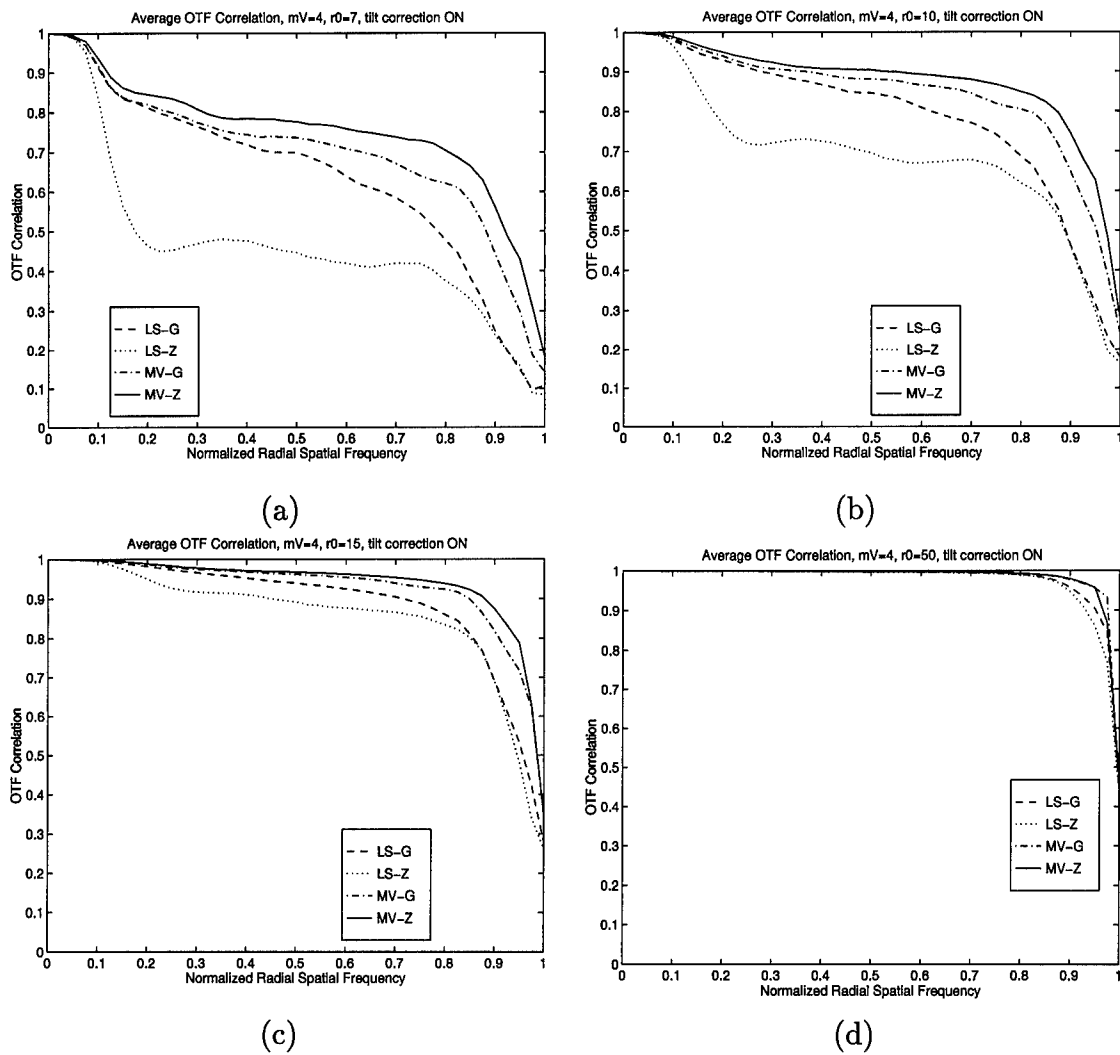


Figure 52. OTF Correlation for  $m_v = 4$  (tilt corrected): (a)  $r_0 = 7$  cm, (b)  $r_0 = 10$  cm, (c)  $r_0 = 15$  cm, (d)  $r_0 = 50$  cm.



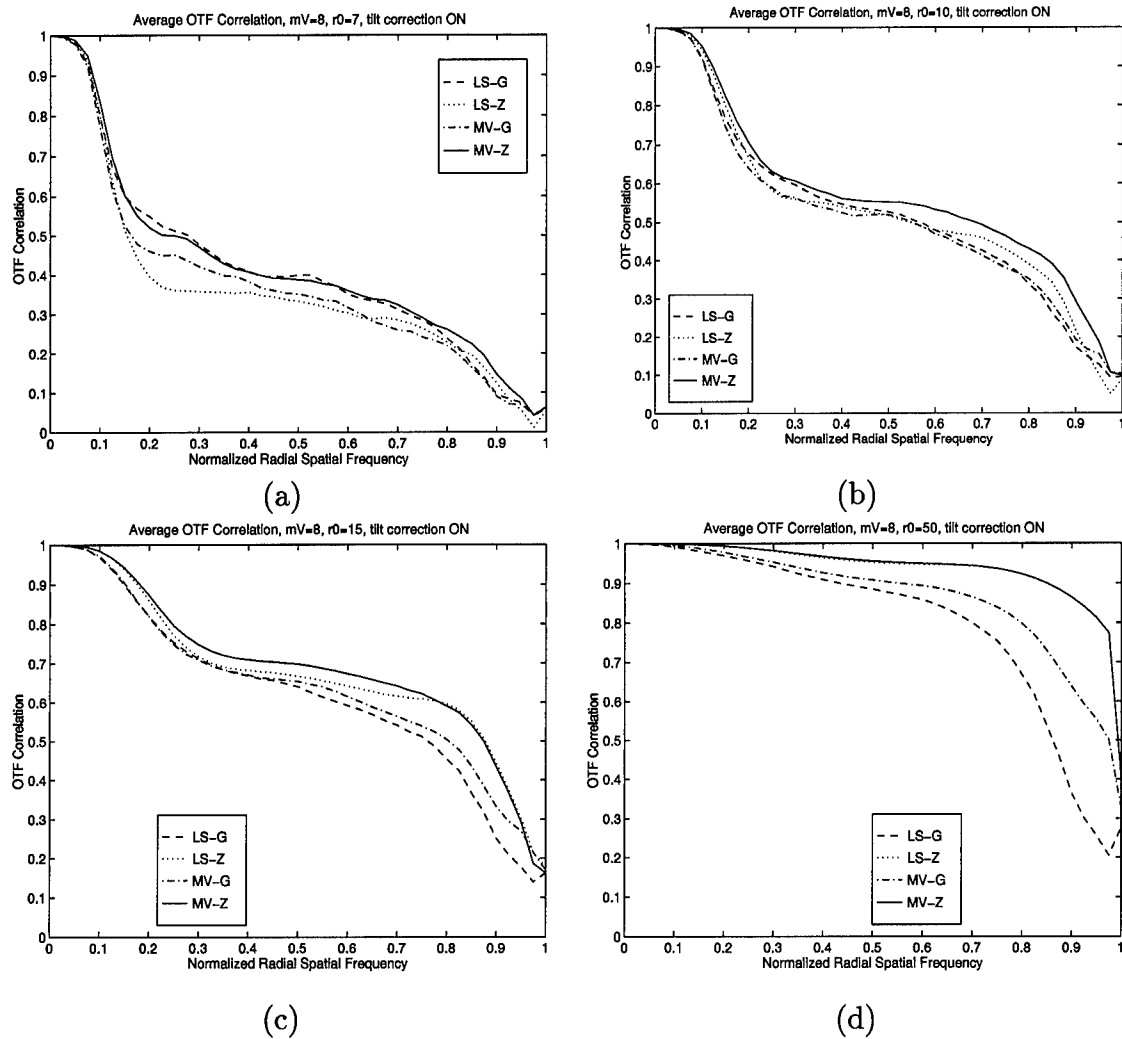


Figure 53. OTF Correlation for  $m_v = 8$  (tilt corrected): (a)  $r_0 = 7$  cm, (b)  $r_0 = 10$  cm, (c)  $r_0 = 15$  cm, (d)  $r_0 = 50$  cm.

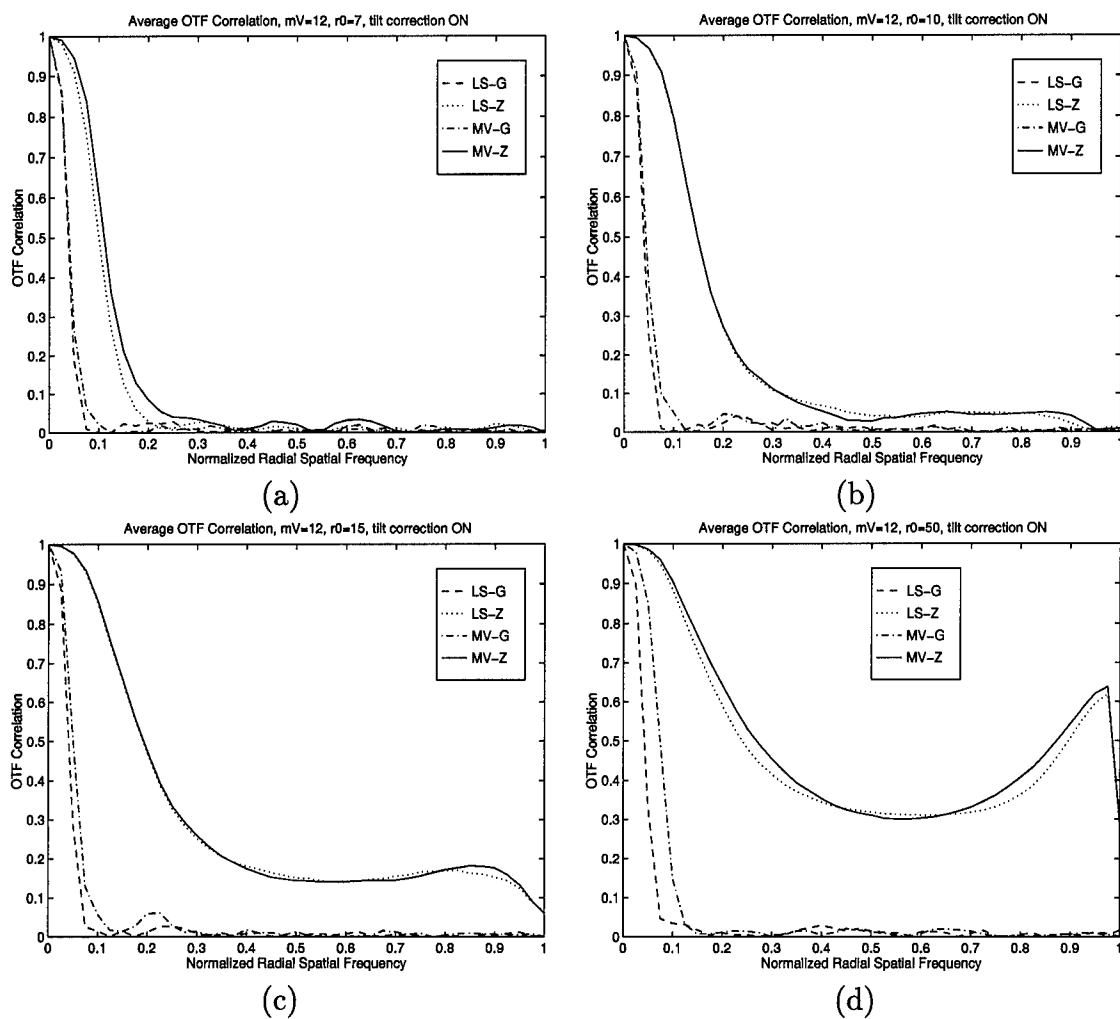


Figure 54. OTF Correlation for  $m_v = 12$  (tilt corrected): (a)  $r_0 = 7$  cm, (b)  $r_0 = 10$  cm, (c)  $r_0 = 15$  cm, (d)  $r_0 = 50$  cm.

## Bibliography

1. Albetski, John, "Air Force Maui Optical Station Historical Data," October 1996. Provided by Mr John Albetski, (808) 874-1641.
2. Arfken, George. *Mathematical Methods for Pyhsicists* (Third Edition). San Diego: Academic Press, Inc., 1985.
3. Bate, Roger R., et al. *Fundamentals of Astrodynamics*. New York: Dover Publications, 1971.
4. Boyce, Linda. "Ground-Based Electro-Optical Deep Space Surveillance." *AF-SPC Space Control Workshop Proceedings*. 1994.
5. "Interagency Report on Orbital Debris." Office of Science and Technology Policy, November 1995. National Science and Technology Council, (202) 456-6100.
6. Duncan, Terry. <http://wwwsor.plk.af.mil/default.html>, March 1996. Phillips Laboratory Starfire Optical Range.
7. Fried, David L. "Post-Detection Wavefront Distortion Compensation." *SPIE Digital Image Recovery and Synthesis, Vol. 828*. 127-133. 1987.
8. Gaskill, Jack D. *Linear Systems, Fourier Transforms, and Optics*. New York: John Wiley & Sons, 1978.
9. Gibson, D.M., et al. "Orbital Debris Characterization: ETS Staring Survey." *SPIE Space Debris Detection and Mitigation, Vol. 1951*. 11-20. 1993.
10. Goodman, Joeseph W. *Statistical Optics*. New York: John Wiley & Sons, 1985.
11. Goodman, Joeseph W. *Introduction to Fourier Optics* (Second Edition). New York: McGraw-Hill, 1996.
12. Hall, Ernest, et al, "Space Operations Orientation Course Student Handbook." 21st Crew Training Squadron, May 1994. Air Force Space Command, Peterson AFB, CO 80909-6822.
13. Henize, Karl G. et al. "Detection of Orbital Debris with GEODSS Telescopes." *SPIE Space Debris Detection and Mitigation, Vol. 1951*. 76-84. 1993.
14. Heroux, L.J. and H.E. Hinteregger. "Handbook of Geophysics and the Space Environment." *Solar Ultraviolet Irradiance Volume 2*, edited by Adolph S. Jursa, Springfield, VA: National Technical Information Service, 1985.
15. Hyde, Cynthia A. *Fourier Phase Spectrum Error Comparisons Using Speckle Imaging with Bispectrum Reconstruction and Deconvolution from Wavefront Sensing*. MS thesis, University of Dayton, 1996.
16. Johnson, Nicholas L. "U.S. Space Surveillance," *Advances in Space Research*, 13(8): 5-19 (1993).

17. Larson, Wiley J. and James R. Wertz. *Space Mission Analysis and Design* (Second Edition). California: Microcosm, Inc., 1992.
18. Lee, David J. *Dissertation Prospectus: Using Wavefront Sensor Information and Image Post-processing to Improve the Resolution of Telescopes with Small Aberrations*. PhD dissertation, Air Force Institute of Technology, 5 March, 1996.
19. Miller, Renee. "Space Surveillance Technologies." *AFSPC Space Control Workshop Proceedings*. 1994.
20. Muolo, Michael J. *Space Handbook; A Warfighter's Guide to Space*. Maxwell AFBV, Alabama: Air University Press, 1993.
21. Nicholls, Tom. <http://op.ph.ic.ac.uk/ao/glossary.html>, May 1996. Applied Optics Group at the Imperial College of Science, Technology, and Medicine.
22. Noll, Robert, J. "Zernike Polynomials and Atmospheric Turbulence," *Journal of the Optical Society of America*, 66(3): 207-211 (March 1976).
23. Pratt, William K. *Digital Image Processing*. New York: John Wiley & Sons, 1978.
24. Primot, J., et al. "Deconvolution from Wave-front Sensing: A New Technique for Compensating Turbulence-degraded Images," *Journal of the Optical Society of America - A*, 7(9): 1598-1608 (September 1990).
25. Rees, W. G. *Physical Principles of Remote Sensing*. New York: Cambridge University Press, 1990.
26. Roggemann, Michael C. "Optical Performance of Fully and Partially Compensated Adaptive Optics Systems Using Least-Squares and Minimum Variance Phase Reconstructors," *Computers in Electrical Engineering*, 18(6): 451-466 (1992).
27. Roggemann, Michael C. Class Notes, PHY 621, Electro-optical Space Systems Technology, January 1996. School of Engineering, Air Force Institute of Technology, Wright Patterson AFB OH.
28. Roggemann, Michael C., et al. "Comparison of Fourier Phase Spectrum Estimation Using Deconvolution from Wavefront Sensing and Bispectrum Reconstruction," *Optics Communications* (1996). accepted for publication.
29. Roggemann, Michael C. and Byron Welsh. *Imaging Through Turbulence*. New York: CRC Press, 1996.
30. Roggemann, Michael C. and Byron M. Welsh. "Signal-to-noise Ratio for Astronomical Imaging by Deconvolution from Wavefront Sensing," *Applied Optics*, 33(23): 5400-5414 (10 August 1994).

31. Roggemann, Michael C., et al. "Biased Estimators and Object-Spectrum Estimation in the Method of Deconvolution from Wave-Front Sensing," *Applied Optics*, 33(24): 5754-5763 (20 August 1994).
32. Seyrafi, Khalil. *Introduction to Electro-optical Imaging and Tracking Systems*. Norwood, MA: Artech House, Inc., 1993.
33. Thompson, Clay. M. *Image Processing Toolbox*. Natick, MA: The Mathworks, Inc., 1993.
34. Wallner, Edward P. "Optimal Wave-front Correction Using Slope Measurements," *Journal of the Optical Society of America*, 73(12): 1771-1776 (December 1983).
35. Welsh, Byron M., et al. "Fundamental Performance Comparison of a Hartmann and a Shearing Interferometer Wave-front Sensor," *Applied Optics*, 34(21): 4186-4195 (20 July 1995).
36. Welsh, Byron M. and Chester S. Gardner. "Performance Analysis of Adaptive-Optics Systems Using Laser Guide Stars and Slope Sensors," *Journal of the Optical Society of America*, 6(12): 1913-1923 (December 1989).
37. Welsh, Byron M. and Michael C. Roggemann. "Signal-to-Noise Comparison of Deconvolution from Wave-front Sensing with Traditional Linear and Speckle Image Reconstruction," *Applied Optics*, 34(12): 2111-2119 (20 April 1995).
38. Welsh, Byron M. and Rudolf N. VonNiederhausern. "Performance Analysis of the Self-Referenced Speckle-Holography Image-Reconstruction Technique," *Applied Optics*, 32(26): 5071-5078 (10 September 1993).
39. Wood, Gregory E. *Estimation of Satellite Orientation from Space Surveillance Imagery Measured with an Adaptive Optics Telescope*. MS thesis, Air Force Institute of Technology, 1996.

## *Vita*

Captain Scott Maethner [REDACTED]. He graduated from St. Cloud Technical High School in 1986 and then attended Concordia College in Moorhead, Minnesota. In May 1990 he received a B.A., Summa Cum Laude, with majors in Physics and Mathematics and minors in Philosophy and Aerospace Studies. He was a distinguished Graduate of the North Dakota State University Reserve Officer Training Corps Program where he was commissioned as a Second Lieutenant in the United States Air Force. In January 1991, Maethner was assigned to the Air Force Phillips Laboratory, Kirtland Air Force Base, New Mexico where he was a project officer for a number of space system survivability projects. In 1993 he transitioned to the space debris research program where he was the technical manager for the debris measurement and modeling programs. In June 1994 he became the space debris program manager. In May 1995, Maethner was assigned to the Air Force Institute of Technology, Wright-Patterson Air Force Base, Ohio to pursue a Master of Science degree in Space Operations. Upon completion of that assignment, Captain Maethner will attend Squadron Officers School en route to an assignment at Air Force Space Command, 50th Space Wing, Fourth Space Operations Squadron, Falcon Air Force Base, Colorado.

[REDACTED]  
[REDACTED]

| REPORT DOCUMENTATION PAGE   |   |  | Form Approved<br>OMB No. 0704-0188                                 |   |
|---|---|--|--|---|
| Public reporting burden for this collection of information is estimated to average 1 hour per response, including the time for reviewing instructions, searching existing data sources, gathering and maintaining the data needed, and completing and reviewing the collection of information. Send comments regarding this burden estimate or any other aspect of this collection of information, including suggestions for reducing this burden, to Washington Headquarters Services, Directorate for Information Operations and Reports, 1215 Jefferson Davis Highway, Suite 1204, Arlington, VA 22202-4302, and to the Office of Management and Budget, Paperwork Reduction Project (0704-0188), Washington, DC 20503.  |   |  |  |   |
| 1. AGENCY USE ONLY (Leave blank)  |   | 2. REPORT DATE<br>December 1996                            |  | 3. REPORT TYPE AND DATES COVERED<br>Master's Thesis |
| 4. TITLE AND SUBTITLE<br>Deconvolution from Wavefront Sensing<br>Using Optimal Wavefront Estimators   |   |  | 5. FUNDING NUMBERS   |   |
| 6. AUTHOR(S)<br>Scott R. Maethner, Capt, USAF   |   |  |  |   |
| 7. PERFORMING ORGANIZATION NAME(S) AND ADDRESS(ES)<br>Air Force Institute of Technology, WPAFB OH 45433-6583  |   |  | 8. PERFORMING ORGANIZATION<br>REPORT NUMBER<br>AFIT/GSO/ENP/96D-01 |   |
| 9. SPONSORING/MONITORING AGENCY NAME(S) AND ADDRESS(ES)<br>Capt Bruce Stribling<br>PL/OL-YY, Kihei, Maui HI 96753   |   |  | 10. SPONSORING/MONITORING<br>AGENCY REPORT NUMBER                  |   |
| 11. SUPPLEMENTARY NOTES   |   |  |  |   |
| 12a. DISTRIBUTION/AVAILABILITY STATEMENT<br>Approved for public release; distribution unlimited   |   |  | 12b. DISTRIBUTION CODE   |   |
| 13. ABSTRACT (Maximum 200 words)<br>A cost effective method to improve the space surveillance mission performance of United States Air Force (USAF) ground-based telescopes is investigated and improved. A minimum variance wavefront estimation technique is used to improve Deconvolution from Wavefront Sensing (DWFS), a method to mitigate the effects of atmospheric turbulence on imaging systems that does not require expensive adaptive optics. Both least-squares and minimum variance wavefront phase estimation techniques are investigated, using both Gaussian and Zernike polynomial elementary functions. Imaging simulations and established performance metrics are used to evaluate these wavefront estimation techniques for a one-meter optical telescope. Performance metrics include the average pupil-averaged mean square phase error of the residual wavefront, the average system transfer function, the signal-to-noise ratio (SNR) of the system transfer function, and the optical transfer function correlation. Results show that the minimum variance estimation technique that employs Zernike polynomial elementary functions offers improvements over all other estimation techniques in each of the performance metrics. Extended object simulations are also conducted which demonstrate the improvements in image quality and resolution that result from the modifications to the DWFS method. Implementation of the DWFS method into USAF space surveillance telescopes is investigated. |   |  |  |   |
| 14. SUBJECT TERMS<br>Atmospheric Turbulence, DWFS, Wavefront, Estimation, Reconstruction, Remote Sensing, Space, Surveillance, Telescope, Minimum Variance, Least Squares, Zernike  |   |  | 15. NUMBER OF PAGES<br>133   |   |
|   |   |  | 16. PRICE CODE   |   |
| 17. SECURITY CLASSIFICATION<br>OF REPORT<br>UNCLASSIFIED  | 18. SECURITY CLASSIFICATION<br>OF THIS PAGE<br>UNCLASSIFIED | 19. SECURITY CLASSIFICATION<br>OF ABSTRACT<br>UNCLASSIFIED | 20. LIMITATION OF ABSTRACT<br>UL                                   |   |

## GENERAL INSTRUCTIONS FOR COMPLETING SF 298

The Report Documentation Page (RDP) is used in announcing and cataloging reports. It is important that this information be consistent with the rest of the report, particularly the cover and title page. Instructions for filling in each block of the form follow. It is important to *stay within the lines* to meet *optical scanning requirements*.

**Block 1. Agency Use Only (Leave blank).**

**Block 2. Report Date.** Full publication date including day, month, and year, if available (e.g. 1 Jan 88). Must cite at least the year.

**Block 3. Type of Report and Dates Covered.** State whether report is interim, final, etc. If applicable, enter inclusive report dates (e.g. 10 Jun 87 - 30 Jun 88).

**Block 4. Title and Subtitle.** A title is taken from the part of the report that provides the most meaningful and complete information. When a report is prepared in more than one volume, repeat the primary title, add volume number, and include subtitle for the specific volume. On classified documents enter the title classification in parentheses.

**Block 5. Funding Numbers.** To include contract and grant numbers; may include program element number(s), project number(s), task number(s), and work unit number(s). Use the following labels:

|                      |                              |
|----------------------|------------------------------|
| C - Contract         | PR - Project                 |
| G - Grant            | TA - Task                    |
| PE - Program Element | WU - Work Unit Accession No. |

**Block 6. Author(s).** Name(s) of person(s) responsible for writing the report, performing the research, or credited with the content of the report. If editor or compiler, this should follow the name(s).

**Block 7. Performing Organization Name(s) and Address(es).** Self-explanatory.

**Block 8. Performing Organization Report Number.** Enter the unique alphanumeric report number(s) assigned by the organization performing the report.

**Block 9. Sponsoring/Monitoring Agency Name(s) and Address(es).** Self-explanatory.

**Block 10. Sponsoring/Monitoring Agency Report Number.** (If known)

**Block 11. Supplementary Notes.** Enter information not included elsewhere such as: Prepared in cooperation with...; Trans. of...; To be published in.... When a report is revised, include a statement whether the new report supersedes or supplements the older report.

**Block 12a. Distribution/Availability Statement.**

Denotes public availability or limitations. Cite any availability to the public. Enter additional limitations or special markings in all capitals (e.g. NOFORN, REL, ITAR).

**DOD** - See DoDD 5230.24, "Distribution Statements on Technical Documents."

**DOE** - See authorities.

**NASA** - See Handbook NHB 2200.2.

**NTIS** - Leave blank.

**Block 12b. Distribution Code.**

**DOD** - Leave blank.

**DOE** - Enter DOE distribution categories from the Standard Distribution for Unclassified Scientific and Technical Reports.

**NASA** - Leave blank.

**NTIS** - Leave blank.

**Block 13. Abstract.** Include a brief (*Maximum 200 words*) factual summary of the most significant information contained in the report.

**Block 14. Subject Terms.** Keywords or phrases identifying major subjects in the report.

**Block 15. Number of Pages.** Enter the total number of pages.

**Block 16. Price Code.** Enter appropriate price code (*NTIS only*).

**Blocks 17. - 19. Security Classifications.** Self-explanatory. Enter U.S. Security Classification in accordance with U.S. Security Regulations (i.e., UNCLASSIFIED). If form contains classified information, stamp classification on the top and bottom of the page.

**Block 20. Limitation of Abstract.** This block must be completed to assign a limitation to the abstract. Enter either UL (unlimited) or SAR (same as report). An entry in this block is necessary if the abstract is to be limited. If blank, the abstract is assumed to be unlimited.